STUDIES OF POLYSACCHARIDE ADSORPTION ONTO MODEL CELLULOSE SURFACES AND SELF-ASSEMBLED MONOLAYERS BY SURFACE PLASMON RESONANCE SPECTROSCOPY

Abdulaziz Kaya

Dissertation submitted to the faculty of the
Virginia Polytechnic Institute and State University
In partial fulfillment of the requirements for the degree of

Doctor of Philosophy
in
Chemistry

Alan R. Esker, Chair

Wolfgang G. Glasser

Louis A. Madsen

Hervé Marand

Thomas C. Ward

August 21, 2009

Blacksburg, Virginia

Keywords: Polysaccharide Adsorption, Hemicelluloses, Xylans, Model Cellulose Surfaces, Self-Assembled Monolayer, Surface Plasmon Resonance Spectroscopy

STUDIES OF POLYSACCHARIDE ADSORPTION ONTO MODEL CELLULOSE SURFACES AND SELF-ASSEMBLED MONOLAYERS BY SURFACE PLASMON RESONANCE SPECTROSCOPY

Abdulaziz Kaya

(Abstract)

Throughout the study of polymer adsorption at the air/water and solid/water interfaces, surface tension measurements and surface plasmon resonance (SPR) spectroscopy have been identified as key methods for the acquisition of structural and thermodynamic information. These techniques were used to determine air/water and cellulose/water interfacial properties of pullulan (P) and pullulan cinnamates (PCs), 2-hydroxypropyltrimethylammonium xylans (HPMAXs), and hydroxypropyl xylans (HPXs).

Hydrophobic modification of pullulan with cinnamate groups promoted adsorption onto model surfaces of regenerated cellulose. In order to understand the relative contributions of hydrophilic and hydrophobic interactions towards PC adsorption, PC adsorption onto self-assembled monolayers (SAMs) with different functional groups was also studied. As the degree of cinnamate substitution increased, greater adsorption onto cellulose, methyl-terminated SAMs (SAM-CH_3), and hydroxyl-terminated SAMs (SAM-OH) was observed. This study showed that hydrogen bonding alone could not provide a complete explanation for PC adsorption onto cellulose.

The adsorption of cationic 2-hydroxypropyltrimethylammonium (HPMA) xylans with different degrees of substitution (DS) onto SAMs and regenerated cellulose was studied by SPR. Surface concentration (Γ) exhibited a maximum (Γ_{max}) for HPMAX adsorption onto carboxylic acid-terminated SAMs (SAM-COOH) at an intermediate HPMA DS of 0.10. This observation was indicative of a relatively flat conformation for adsorbed HPMAXs with higher HPMA DS because of higher linear charge densities along the polymer backbone. Γ observed for HPMAX adsorption onto regenerated cellulose and SAM-OH surfaces was relatively low compared to HPMAX adsorption onto SAM-COOH surfaces.

Surface tension measurements for aqueous solutions of HPX by the Wilhelmy plate technique showed that surface tension changes ($\Delta\gamma = \gamma_{water} - \gamma_{HPX(aq)}$) increased and critical aggregation concentrations generally decreased with increasing hydroxypropyl (HP) DS. Hence, even though HP substitution was necessary to induce aqueous solubility, excessive hydroxypropylation promoted aggregation in water. SPR studies indicated that HPXs did not adsorb significantly onto regenerated cellulose or SAM-OH surfaces (submonolayer coverage). In contrast, HPX did adsorb (~monolayer coverage) onto SAM-CH_3 surfaces.

Collectively, these studies showed natural polymers could be chemically modified to produce surface modifying agents with sufficient chemical control, whereby the surface properties of the resulting systems could be explained in terms of chemical structure and intermolecular interactions.

ACKNOWLEDGMENTS

I would like to thank my advisor, Prof. Alan Esker for his guidance during my Ph. D. study at Virginia Tech. As an advisor, Alan is strict, patient and always encouraging. He always pushed me to the limits which made me to think as a scientist.

I would like to thank my committee members: Prof. Wolfgang G. Glasser, Prof. Lou Madsen, Prof. Herve Marand, and Prof. Thomas C. Ward for encouragement, helpful suggestions and constructive criticism. In particular, I am thankful to Prof. Glasser for taking time out of his busy schedule to provide valuable suggestions as well as help with my career decisions. I also would like to thank Prof. Paul Deck for his help in my plan of study changes.

I would also like to acknowledge the financial support of the Department of Chemistry at Virginia Tech in the form of teaching assistantship and in the form of tuition funds, and the United States Department of Agriculture (USDA) and the National Science Foundation (NSF) in the form of research funds.

I am also grateful to all my former and present group members: Dr. Hyong Jun Kim, Sheila Gradwell, Jianjun Deng, Suolong Ni, Rituparna Paul, Bingbing Li, Woojin Lee, Ufuk Karabiyik, Wen Yin, Jae-Hyun Sim, Qiongdan Xie, Joshua Kittle, Zelin Lin, Yang Liu, Xiaosong Du, and Chuanzi OuYang. In particular, I want to thank Zelin Liu for his great help and friendship during the past four years.

I wish to express my sincere appreciation and gratitude to my professors at Koç University; Professor İskender Yılgör and Mrs. Emel Yılgör who were always there for me like my parents and who encouraged me to come to Virginia Tech. As always, I would like to thank my family for their unconditional love and support over the years. Without their love and trust, I would not have finished my graduate study. Last but not the least, I would like to thank all my

friends for all the great times and for cheering me up when things looked bleak. Although I did not list you individually here, you know who you are.

TABLE OF CONTENTS

List of Figures

Chapter 2

Chapter 3

Chapter 4

Chapter 5

Chapter 6

Chapter 7

List of Tables

CHAPTER 1

Overview

Engineering interfaces is important in order to develop high strength composites. Wood based biocomposites suffer from incompatibility between hydrophilic cellulosic fibers and hydrophobic thermoplastics which yields poor mechanical properties. Our aim in this study was to understand the fundamentals behind polysaccharide adsorption from aqueous solution onto surfaces in order to engineer better interfaces in the future. Another aim of this study was to utilize biomass to develop surface modifying agents for cellulosic systems. We have investigated xylan derivatives, a hemicellulose, for this purpose because hemicelluloses play an important role in compatibilizing cellulose and lignin in plant cell walls.

This dissertation consists of seven chapters. In Chapter 2 (Introduction and Literature Review), the three main components of wood (cellulose, hemicellulose, and lignin), and their mutual interactions are discussed at the start of the chapter. Subsequent discussion focuses on theoretical concepts for polymer adsorption and experimental methods for investigating polymer adsorption. After an overview on the three main components of wood, physical investigations of these three components are discussed in the context of previous self-assembly and adsorption studies. This discussion is followed by coverage of thermodynamic treatments of an interface and the Gibbs adsorption isotherm. Theoretical predictions and explanations for polymer adsorption based upon self-consistent field and scaling theories are then addressed. The thesis then moves on to polyelectrolyte adsorption, and relevant features of polyelectrolyte solutions and interfacial properties. Next, surface tension measurements at the air/water interface, as a technique for providing surface excesses, are covered. These topics are then followed by a discussion of model cellulose surfaces and recent studies involving these surfaces. Moreover,

self-assembled monolayers (SAMs) and structural properties of SAMs will be illustrated as relevant model systems for exploring interactions between adsorbates and specific surface functional groups. Finally, surface plasmon resonance (SPR) spectroscopy, the main optical technique used in this dissertation, will be introduced for studying polymer adsorption.

Materials and experimental techniques for this thesis are provided in Chapter 3. The description of materials and experimental methods will not be repeated in subsequent chapters.

Chapter 4 describes the self-assembly of pullulan and pullulan cinnamates onto regenerated cellulose surfaces and self-assembled monolayers. Surface tension and pyrene dye fluorescence experiments used to probe aqueous solution properties of pullulan and pullulan cinnamates will also be covered. Next, pullulan and pullulan cinnamate adsorption onto model cellulose surfaces and self-assembled monolayers will be discussed along with in-situ atomic force microscopy (AFM) studies of pullulan and pullulan cinnamate layers adsorbed onto regenerated cellulose surfaces and various SAMs. Fitting of experimental adsorption isotherms to Langmuir and Freundlich adsorption isotherms will be demonstrated with subsequent speculation about possible conformations of adsorbed pullulan and pullulan cinnamate layers on the aforementioned surfaces.

Chapter 5 decribes the adsorption of 2-hydroxypropyltrimethylammonium xylan (HPMAX) onto SAMs and regenerated cellulose surfaces. The dominant role of electrostatic interactions on the adsorption process is the primary emphasis of this chapter. Initially, studies of HPMAX adsorption onto carboxyl terminated SAMs is discussed with respect to how linear charge density along the HPMAX backbone affects adsorption. Ultimately, comparisons to HPMAX adsorption onto other hydrophilic and hydrophobic surfaces are also made to probe the roles, hydrogen bonding and van der Waals interactions play on adsorption. These results are discussed in terms of predictions from scaling theory.

In Chapter 6, the adsorption of hydroxypropylxylan (HPX) at the air/water interface and onto regenerated cellulose surfaces and SAMs will be discussed. NMR characterization of acetylated derivatives of HPX will be discussed for the determination of the degrees of substitution. Surface tension measurements of aqueous HPX enabled us to estimate surface excesses at the air/water interface by using the Gibbs adsorption isotherm. Chapter 6 will conclude by discussing HPX adsorption onto SAMs and regenerated cellulose surfaces by SPR.

Finally, Chapter 7 summarizes the overall conclusions of this thesis and provides suggestions for future work. In particular other possible directions that can be explored through polysaccharide adsorption onto model cellulose surfaces and self-assembled monolayers will be discussed.

CHAPTER 2

Introduction and Literature Review

2.1 Introduction to Wood

Wood is a complex plant tissue composed of different types of cells. It can be easily recognized as the tissue located inside tree bark and it forms the interior part of major stems, branches, and roots.[1] Within living trees, wood (xylem) has the function of support, nutrient and mineral conduction, and storage. The support function helps the tree to remain erect despite the heights to which a tree grows. Transport of ground water to upper parts of a tree occurs through tube like structures in wood. Finally, food (energy) is stored in certain parts of the wood. The wood cells which support the tree and conduct water make up 60 to 90 percent of wood by volume. Within the living tree, these cells are dead which means that the cytoplasm is absent leaving hollow cells with rigid walls. The only living portion of the wood is the food storing cells.[2] Almost, all of the wood cells are derived from the layer that lies immediately outside the wood in a tree, which is called the vascular cambium. There are two kinds of cells in the vascular cambium: spindle-shaped, axialy elongated cells, termed as fusiform initials, and ray initials, which are as broad as they are high.[3] While these structures are present in all trees, several types of wood with different structure and properties can be obtained through the hierarchical assembly noted above.

The secondary xylem produced by cell division in the vascular cambium of gymnosperms is termed softwood, while that of angiosperms is hardwood. Both softwoods and hardwoods are widely distributed on earth. The characterization of the xylem species from arctic regions to moderate temperature regions can be carried out by considering the distinct growth rings. For softwood, which consists mainly of tracheids, the latewood (summer wood) has smaller radial

dimensions and thicker cell walls than earlywood (spring wood). These anatomical differences yield higher densities for latewood compared to earlywood. Hardwoods, like softwoods, are also present in tropical and arctic regions. In colder regions, hardwoods are deciduous, but in tropical regions they are evergreen and growth regions are not easily recognized. While tracheids are the main cells in softwoods, hardwoods can have a variety of cells. The macroscopic characteristics of hardwoods are governed by the distribution and number of different types of cells such as vessels, parenchyma, and fibers.[4] Hardwoods are characterized by the presence of vessels (pores). These vessels or pores are cells which occupy a large cross-sectional area and can usually be detected by the unaided eye.[2, 5] Fibers make up 25% of the wood by volume, but in some hardwoods they can make up 50-70 % of the wood by volume.[4]

2.1.1 Formation and Structure of the Cell Wall

Living cells associated with the growth and development of the woody stem of trees are produced in the vascular cambium which is located between the xylem and the phloem. These cambium cells form a sheath of living cells around the stem, root, and branches of the tree. The development of xylem cells from the cambium happens in four phases, cell division, the growth of the daughter cells into mature cells, development of the secondary cell wall (wall thickening), and lignification. Two kinds of cell division can occur: (a) tangential/longitudinal (periclinal) which involves an increase in the diameter of the stem, and (b) pseudo-transverse (anticlinal) which increases the circumference of the stem (Figure 2.1). The periclinal division of each cambium initial gives rise to daughter cells. The circumferences of the initials are increased by anticlinal division, i.e., new rows of cambium initials are introduced. All the daughter cells expand radially and longitudinally until final cell dimensions are reached. During rapid extension

of the daughter cells, there is an active growth in the cell wall which corresponds to the formation of the cellulose microfibrils.[5]

During the enlargement of daughter cells to form mature cells, the cells consist of a primary wall that can grow both longitudinally and radially. After the cells reach their full dimensions, a secondary wall starts to deposit onto the internal side of the primary wall that increases the rigidity and thickness of the cell wall. Figure 2.2 presents cell walls of two mature cells from a softwood species. Three distinct layers can be seen. Primary walls for the two cells are present adjacent to both sides of the middle lamella (the midline between the two cells in Figure 2.2). However, this primary wall is too thin and it is very hard to observe. Therefore, the term compound middle lamella is usually used for the region that includes both the middle lamella and two primary cell walls (c in Figure 2.2). Adjacent to the compound middle lamella, the first layer of the secondary cell wall, the S_1 layer, is present. The central layer, the S_2 layer, is the thickest of the three layers of the secondary cell wall. Finally, the innermost layer adjacent to the lumen is called the S_3 layer.[2]

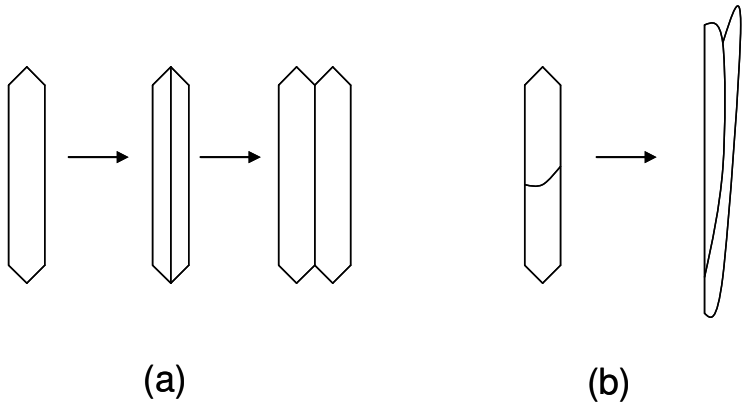

Figure 2.1: A schematic representation of the (a) periclinal and (b) anticlinal division of the cambium initial.

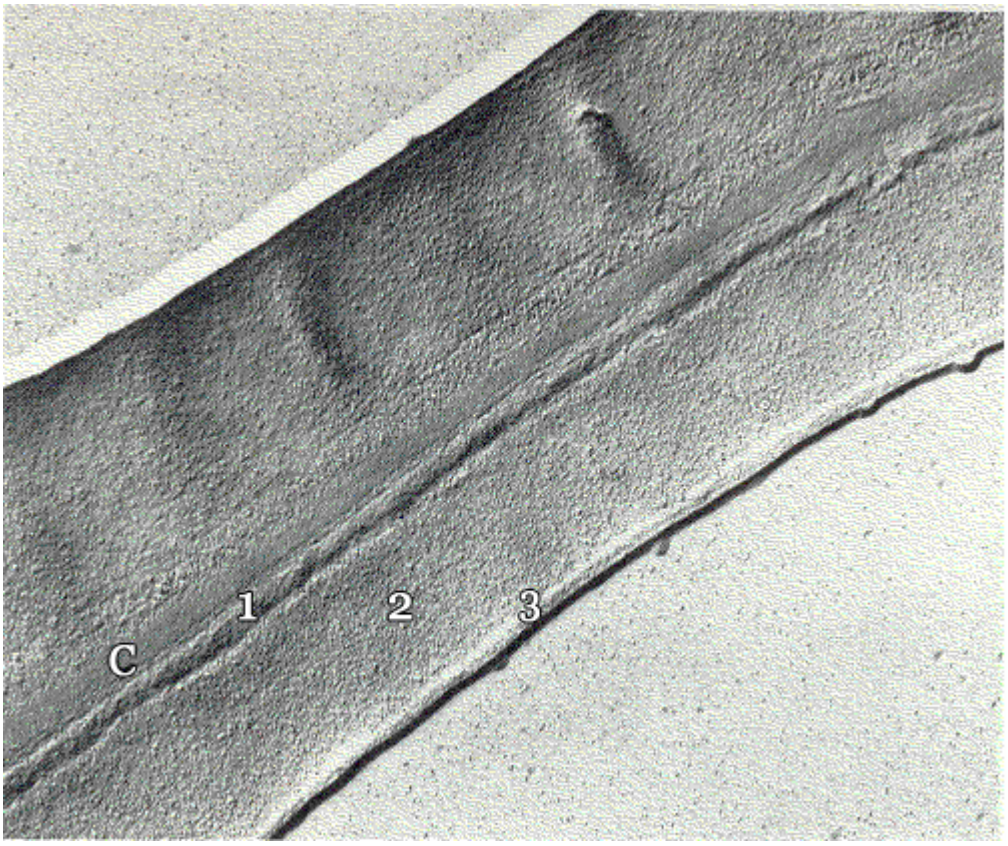

Figure 2.2: Cell walls in a cross-sectional view from springwood tracheids depicting cell wall layering. C: compound middle lamella, 1: S_1 layer, 2: S_2 layer, and 3: S_3 layer (16000× magnification). Reprinted with permission from *ACS Symposium Series* **1977**, *43*, 1-23. Copyright [1977] American Chemical Society.

2.1.2 Chemical Composition of the Cell Wall

The major constituents of the cell wall are cellulose, hemicellulose, and lignin. These polysaccharides and complex crosslinked "phenylpropane" polymers form a composite structure that is the cell wall.[6] Other polymeric constituents such as starch, pectin, and ash for extractive-free wood are present in varying quantities to a lesser extent. The cellulose content is more or less the same (43 ± 2%) by weight for both softwoods and hardwoods. The lignin content of hardwoods varies between 18 and 25% by weight, whereas softwood varies between 25% and 35% by weight. The hemicelluloses found in both groups are different in structure and in quality.

The hemicellulose content of the cell wall varies between 20 and 35% by weight in hardwoods, versus as much as 30% by weight in softwoods.[7]

2.1.2.1 Cellulose

Cellulose is the most abundant component of the cell wall and is also the main component of a variety of natural fibers such as cotton, bast fibers, and leaf fibers. In nature, cellulose is found in close association with hemicelluloses, pectin, water, wax, proteins, lignin, and mineral substances. This biopolymer is a linear chain composed of anhydro-D-glucopyranose units linked by β-(1→4)-glucosidic bonds (Figure 2.3).[8] These pyranose rings are found to be in the chair conformation, $^4C_1$, in which hydroxyl groups are in equatorial positions.[9] Therefore, cellulose is an extensive, linear polymer chain containing a large number of hydroxyl groups (3 per anhydroglucose unit) in the thermodynamically preferred conformation of $^4C_1$. To preserve the bond angles for acetal-oxygen bridges, every other anhydroglucose unit (AGU) is rotated 180° in the plane of the molecule.[10] The dimer cellobiose is actually the repeating unit of cellulose, but AGUs are used for determining the degree of polymerization (DP or n).[11] DPs for cellulose molecules depend on the origin and treatment of the raw material. For wood pulp, DP varies from ~ 300 to 1700. Cotton and other plant fibers have DP values in the range of ~ 800 to 10000 depending on the treatment.[10]

In the cell wall, cellulose exists in the form of threadlike structures which are called microfibrils.[4] These microfibrils are about 10 to 29 nm in diameter, and are much longer than their diameter. Each microfibril consists of about 2000 or so cellulose molecules arranged in a parallel orientation, to form a crystalline array.[12] The crystallinity has been demonstrated by X-ray diffraction and polarized optical microscopy.[4] X-ray diffraction measurements show that crystalline regions are interrupted with non-crystalline (amorphous regions) about every 600Å.[2, 5]

However, physical and chemical investigations reveal that cellulose molecules are long and can be at least 50,000 Å in length. Therefore, it is assumed that each cellulose molecule passes through a number of crystalline regions, and that cellulose chains only align in these crystalline regions.[5] The orientation of the fibers varies greatly between the three layers of the secondary cell wall. In the S_1 layer, the cellulose fibers are arranged in helical structures where about half of the molecules are left-handed and the other half are right-handed. In the S_2 layer, the cellulose fibers are composed entirely of right-handed helices, but the angle between the fiber direction and the long axis of the cell varies between 10° and 40° in different woods. In the S_3 layer, the angles between the long axis of the cell and the fiber are greater than that of the S_2 layer, between 10° and 60°. Initially, the cellulose microfibrils are laid down in a porous matrix of hemicellulose. Later, these pores are occupied by lignin.[12]

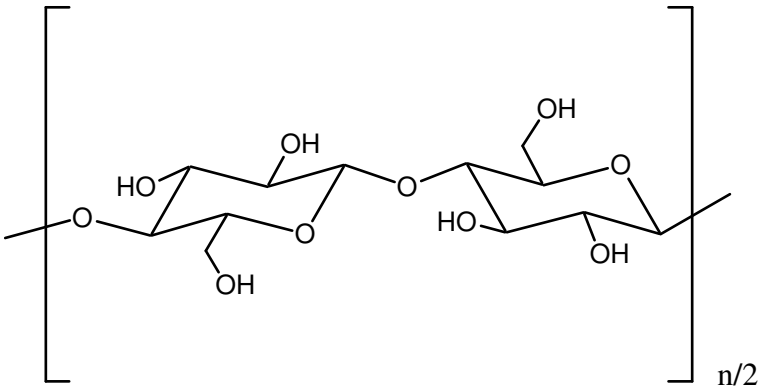

Figure 2.3: Repeating unit of cellulose.

Cellulose chains can form several alternate structures when these chains associate with each other through hydrogen bonds and van der Waals forces.[13] There are four different polymorphs of cellulose (I, II, III, and IV). Cellulose I is the form found in nature and it occurs in two different allomorphs (I_α and I_β).[11] Cellulose II, the second most studied cellulose polymorph, can be obtained from cellulose I by one of two processes: (a) solubilization of

cellulose in a solvent and reprecipitation by dilution with water; or (b) mercerization, which is the process of swelling native fibers with sodium hydroxide and then removing the swelling agent.[9] Cellulose III and cellulose IV are obtained from liquid ammonia and heat treatment of the other polymorphs, respectively.[14]

Thermodynamically, the most stable polymorph is cellulose II, which has an additional hydrogen bond for each glucan unit.[15] In both cellulose I and cellulose II, the dominant intramolecular hydrogen bonding is O3-H····O5.[16-18] However, intermolecular hydrogen bonding is different for the two polymorphs. In cellulose I, O6-H····O3 intermolecular hydrogen bonding dominates, whereas in cellulose II, O6-H····O2 is present.[11] It is also important to emphasize the fact that all the hydrogen atoms are more or less hydrogen bonded and there are no "free" or "non-hydrogen bonded hydroxyl groups" present in cellulose.[19] The large number of hydrogen bonds makes the linear cellulose molecules strongly associate with each other laterally. The crystallinity of cellulose arises from this excellent association and nearly perfect alignment of the cellulose molecules.[2]

2.1.2.2 Lignin

Lignin is the most abundant aromatic (phenolic) polymer in nature[20] and is distributed with hemicelluloses in the spaces between cellulose microfibrils in primary and secondary walls, and in middle lamellae.[21] Its main function is to cement cellulose microfibrils together.[22] It is a widely accepted concept that lignin is formed by the enzymatic dehydrogenative polymerization of three phenylpropane units (monolignol). The biosynthesis of lignin employs various oxidative coupling reactions of resonance-stabilized phenoxy radicals obtained from these phenylpropane units leading to randomly cross-linked macromolecules.[23] These phenylpropane units are: p-coumaryl, coniferyl, and sinapyl alcohols (Figure 2.4).[22, 24-26] Lignins can be divided into three

broad groups; softwood lignin, hardwood lignin, and grass lignin. Softwood lignin, also called guaiacyl lignin, originates from the precursor, coniferyl alcohol. Hardwood lignin is made up of coniferyl and sinapyl alcohol units. Grass lignin is derived from coniferyl, sinapyl, and p-coumaryl alcohol units.[22]

Lignin is the most complex high molecular weight natural polymer in the cell wall, and investigators still struggle with structure determination. The presence of many complex C-C linkages makes it harder to decompose the structure into lower molecular weight species without inducing structural changes. It is also optically inactive which is unusual for a biopolymer.[27] This behavior may be expected from a random three-dimensional network.[28] Furthermore, it is an amorphous polymer[23] and there are no reports of even semi-crystalline lignin.[28] Because it is not possible to isolate lignin quantitatively from plant materials without chemical or mechanical degradation, the true molar mass (MW) of lignin cannot be determined. In the isolation process, lignin usually degrades into fragments of varying size. Reported MWs of these isolated lignins range from 10^2 to 10^6 g•mol^{-1} depending on the source of the lignin and the isolation process.[29] Although native lignin is insoluble in virtually all simple solvents,[23, 28] isolated lignins exhibit partial solubility in solvents like dioxane, acetone, methyl cellosolve (ethylene glycol monomethyl ether), THF, DMF, and DMSO.[23]

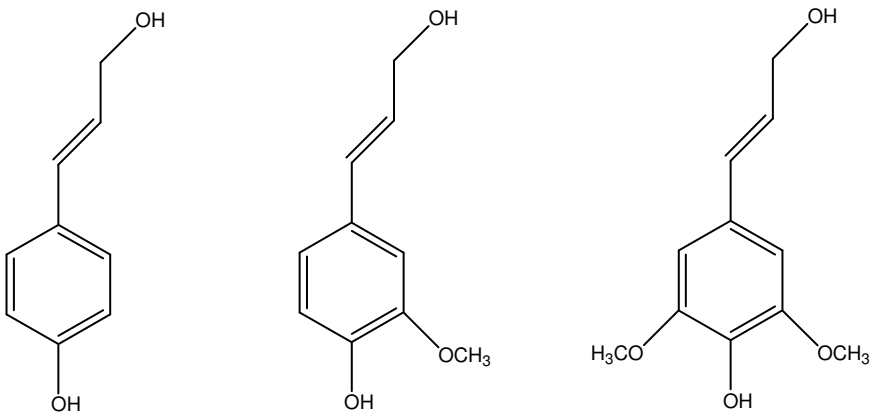

(a) (b) (c)

Figure 2.4: Lignin precursors (a) p-coumaryl alcohol, (b) coniferyl alcohol, and (c) sinapyl alcohol.

2.1.2.3 Hemicelluloses

Hemicelluloses are the most complex molecules in the cell walls of woods, straws, and grasses and comprise roughly one-fourth to one-third of the material present in most plants. In contrast to cellulose, these compounds are non-crystalline heteropolysaccharides and are classically defined as the alkaline soluble material that remains after pectic substances are removed.[30] Pectins are polysaccharides extracted from cell walls by hot water, ammonium oxalate, weak acid, or chelating reagents. Extraction of hemicelluloses from the cell wall requires strong alkali rather than the weak acids used for the extraction of pectins.[31] In plant cell walls, hemicelluloses are situated between the lignin and the collection of cellulose fibers that form the microfibrils.[32] They form hydrogen bonds with cellulose, covalent bonds with lignin, and ester linkages with acetyl units and hydroxycinnamic acids. Figure 2.5 provides one example of a hemicellulose-lignin linkage where ferulic acid, ether-linked lignin, forms a cross-link to hemicelluloses through an ester linkage. The general formulae of hemicelluloses are $(C_5H_8O_4)_n$ and $(C_6H_{10}O_5)_n$, and these units are termed as pentoses and hexoses, respectively. The principle

sugars present in hemicelluloses (Figure 2.6) are D-glucose, D-galactose, D-xylose, D-mannose, L-arabinose, D-glucuronic acid, 4-O-methyl-D-glucuronic acid, and D-galacturonic acid, and to a lesser extent, L-rhamnose, L-fucose and various 4-O-methylated neutral sugars. These sugar units are arranged in different proportions with different substituents depending on the source of the hemicellulose.[30]

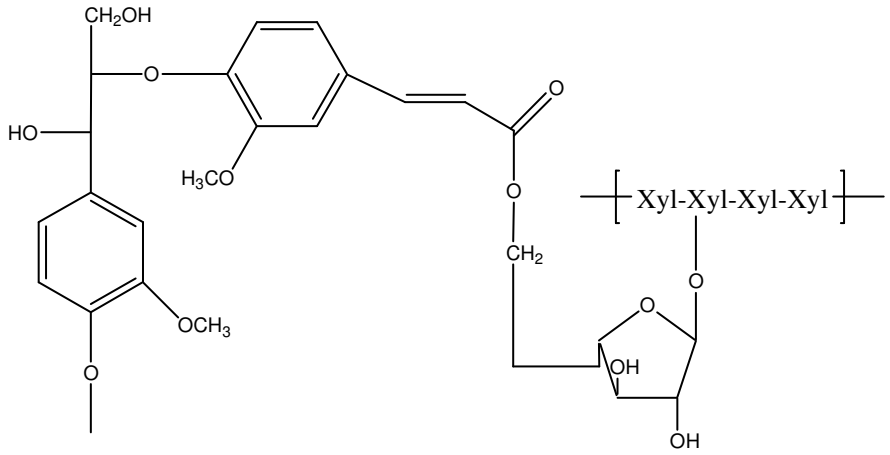

Figure 2.5: An example of a hemicellulose-ester-ferulic acid-ether-lignin bridge.

The chemical and thermal stability of hemicelluloses are lower than cellulose because they are non-crystalline and generally have low degrees of polymerization, n ~ 100 to 200. In addition, hemicelluloses differ from cellulose in terms of their alkali solubility. This characteristic is exploited to fractionate polysaccharides using different alkali conditions for lignin-free samples.[23] Hemicelluloses can be divided into four groups of structurally different polysaccharides: (a) xylans, (b) mannans, (c) β-glucans with mixed linkages, and (d) xyloglucans.[33] Subgroups exist within a given group.

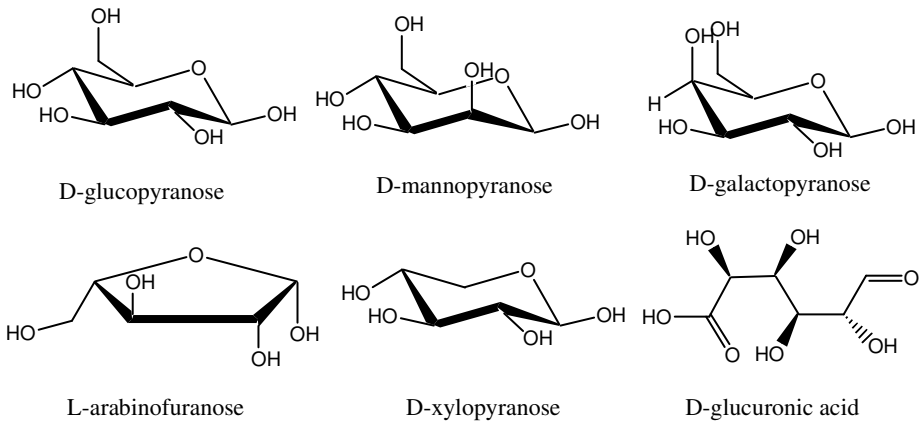

Figure 2.6: Main sugars used in hemicellulose biosynthesis.

2.1.2.4 Xylans

Xylans are the major component in the primary cell walls of monocotyl plants (grasses and cereals), whereas they exist in secondary cell walls of dicotyl plants (hardwoods and herbaceous plants).[33, 34] Monocots and dicots are two divisive groups of flowering plants. In dicots, there are two cotyledons (seed leaves) and, but in monocots, there is only one cotyledon.[35] Xylans from terrestrial plants have a backbone of β-(1→4)-D-xylopyranosyl groups that are branched with short hydrocarbon groups. Based on the known primary structure of xylans, xylans can be subdivided into homoxylans and heteroxylans, the latter include glucuronoxylans, (arabino)glucuronoxylans, (glucurono)arabinoxylans, arabinoxylans, and complex heteroxylans.[33] Homoxylans in which D-xylopyranosyl (Xylp) residues are linked by β-(1→3), β-(1→4), and/or mixed β-(1→3), β-(1→4) linkages are common in seaweeds (e.g. red and green algaes). In the highest evolutionary dicots (e.g. hardwoods), the main hemicellulose component of the secondary cell walls is glucuronoxylan (GX) (Figure 2.7) where α-D-glucuronic acid (GA) and/or 4-*O*-methyl α-D-glucuronic acid (MeGA) can be attached to the O-2 position of Xylp repeating units.[36] In (arabino)glucuronoxylans (AGX), α-L-arabinofuranosyl (Araf) units are usually attached at position 3 of the Xylp repeating units in addition to attachment of GA and/or

MeGA at position 2. AGX exists in softwoods and lignified tissues of grasses and annual plants.[37] The main difference between (arabino)glucuronoxylans and (glucurono)arabinoxylans (GAX) is the disubstituted Araf units for each Xylp repeating unit.[36] Neutral arabinoxylans (AX), in which Araf residues are usually substituted at position 3 or both position 2 and 3 of Xylp repeating units, represent the main xylan component of cereal grains.[37] The last xylan group, complex heteroxylans (CHX), have their Xylp backbone substituted with various mono- and oligoglycosyl side chains in addition to Araf, GA and MeGA units.[33] The degree of side chain substitution and substitution pattern determines the solubility of xylan in common solvents, interactions with other cell wall components, degradability by enzymes, and solution and functional properties.[37]

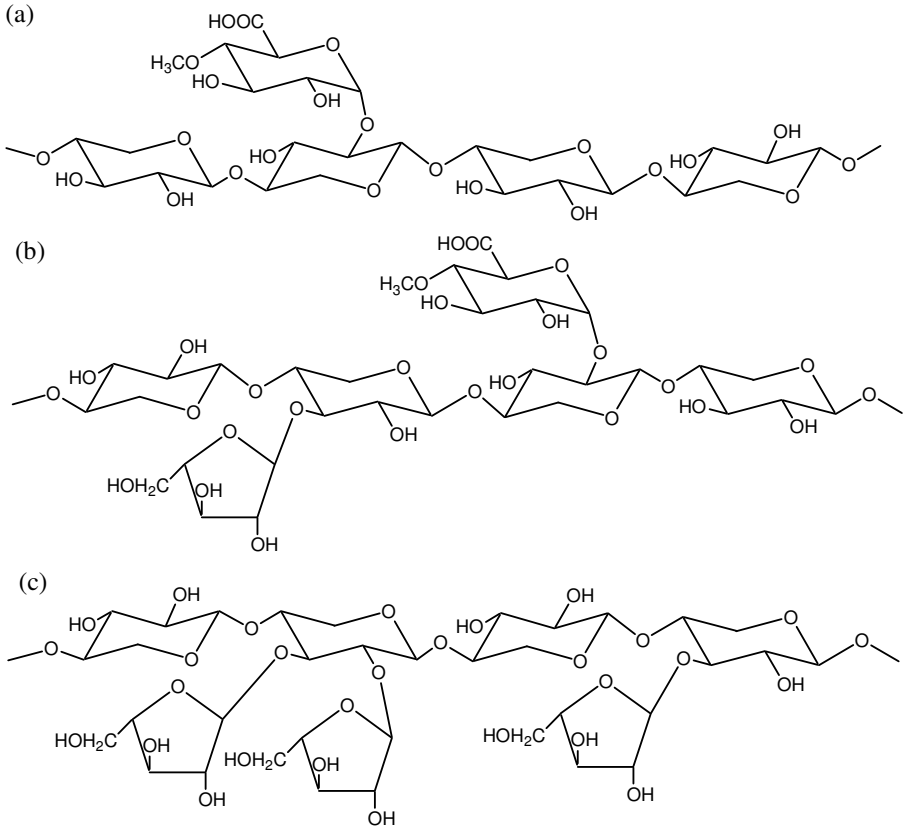

Figure 2.7: Structural features of (a) glucuronoxylan (GX), (b) (arabino)glucuronoxylans (AGX), and (c) arabinoxylan (AX).

2.1.3 Physical Investigations of Interactions Between Cellulose, Hemicellulose, and Lignin

Figure 2.8 illustares the structure of the cell wall of a softwood fiber proposed by Salmen et al.[38] They suggested that different types of lignin could be associated with different kinds of hemicelluloses in the S_2 layer. An earlier deposition of condensed lignin and unsubstituted xylan led to a closer proximity of these polymers towards the cellulose microfibril aggregates. By chemical analysis of lignin carbohydrate complexes isolated from spruce wood, Lawoko et al.[39] found a more condensed type of lignin associated to glucomannan, while the less condensed type lignin was associated to xylan. In accordance with these experimental observations, they also proposed that in hardwoods, a low substituted xylan was associated with cellulose and with a condensed type of lignin. On the other hand, a highly substituted xylan was more closely associated with a less-condensed type of lignin. In softwood, the glucomannan replaced the low substituted xylan as depicted in Figure 2.8.[38]

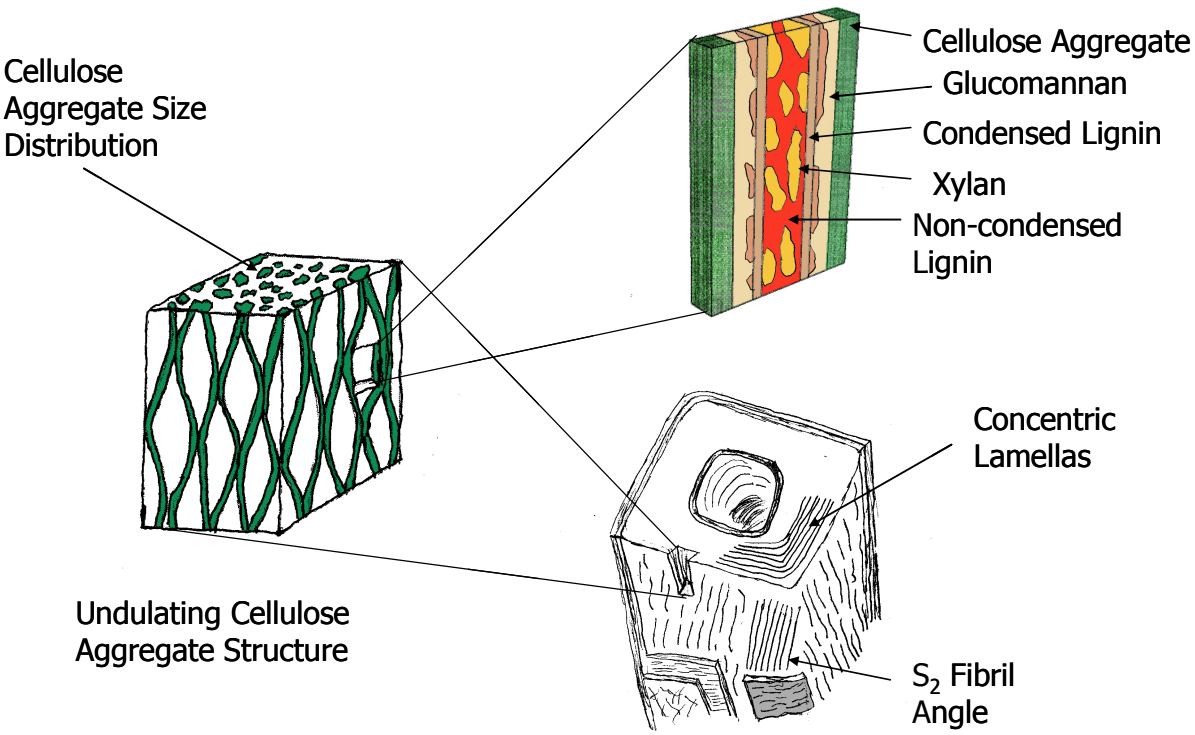

Figure 2.8: Schematic picture of the cell wall of a softwood fiber (tracheid). The figure indicates the cellulose microfibril angle of the secondary wall (S_2), the concentric lamellar arrangement of cellulose aggregates interspaced by matrix lamella, the lenticular undulating cellulose aggregate structure and the variability of cellulose aggregate sizes, as well as the arrangement of matrix components from glucomannan (non-substituted xylan in hardwoods) closest to the cellulose microfibrils that outwards associates to a condensed type of lignin followed by the xylan (more highly substituted xylan in hardwoods) associated to a more non-condensed type of lignin. Adapted from Salmen et al.[38]

2.1.3.1 Miscibility of the Chief Components of Wood

The miscibility of two materials can be studied by thermal analysis. If the blend shows a single glass transition temperature (T_g) between the glass transition temperatures of the two

constituents of the blend, the two materials are miscible with each other. However, immiscible blends exhibit two separate glass transition temperatures each corresponding to the T_g of the individual homopolymer. Partial miscibility is indicated by migration of the T_g values toward a common glass transition temperature which is a function of the fraction of each component present.[40]

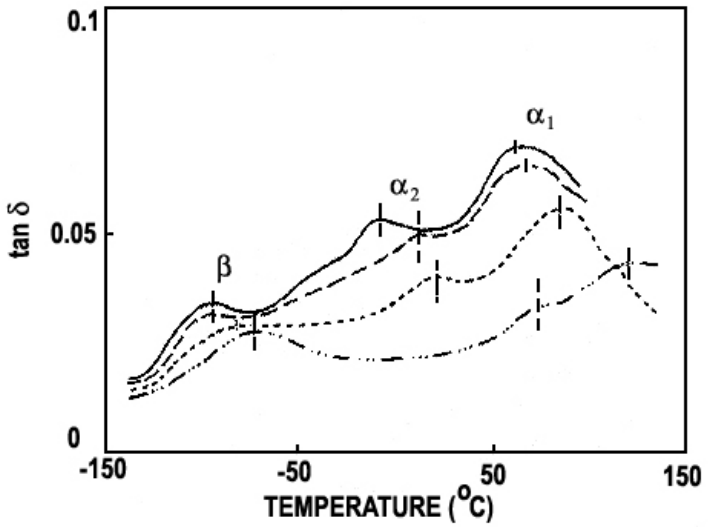

Figure 2.9: Dynamic mechanical and thermal analysis of solid spruce wood. Moisture contents are (--·--) 5 %, (----) 10 %, (– – –) 20 %, and (——) 30 %. Reprinted with permission from *Journal of Materials Science* **1987**, *22*, 617-624. Copyright [1987] Springer.

Dynamic mechanical and thermal analysis (DMTA) of the amorphous region of solid spruce wood is shown in Figure 2.9. The tan δ (phase angle of strain used in DMTA) is plotted against temperature for five different wood samples with varying moisture content, 5% (bottom) to 30% (top). The β transition is a secondary relaxation involving small-scale molecular motions which are attributed to the local site exchange of the moisture content of the wood. The α_1 and α_2 transitions which are due to large scale motions of the backbone chain imply two distinct glass

transition temperatures. These two transitions are caused by two different amorphous materials residing in wood, each having different phases at the molecular level. It has been concluded that the α_1 transition corresponds to lignin and the α_2 transition corresponds to the hemicellulose.[41, 42] These components are covalently linked to each other in a block copolymer fashion, a conclusion that is consistent with two different transitions in dynamic mechanical analysis of bulk wood and, the ability of these amphiphilic substances to form micelles or aggregates in solution.[42-46]

2.1.3.2 Previous Self-Assembly Studies of Biological Materials

Self-assembly behavior has been studied in order to understand the hierarchical structure of wood composites. The micelle forming properties of many amphiphilic block copolymers containing poly(ethylene oxide) such as polystyrene-b-poly(ethylene oxide) and poly(propylene oxide)-b-poly(ethylene oxide) have been performed.[47] Self-assembled structures have also been found for natural polymers including oligosaccharide-protein block copolymers,[48] hydroxyethyl cellulose,[49, 50] fluorine-containing cellulose diblock structures, and xylan-rich hetereopolysaccharides and their derivatives.[51] Lignin-carbohydrate structures also form micellar structures in aqueous solution.[45] Lignin-carbohydrate complexes consist of sugar chains with lignin moieties as pendant side groups. It is believed that lignin is attached to sugar units with aromatic ether linkages. The exact nature of the interaction between lignin and carbonhydrate is still unclear, but it is known that a covalent bond exists between the lignin and the carbohydrate. The lignin-carbohydrate complexes form micelles in the aqueous solution due to the hydrophobic nature of the lignin. The study of the self-assembly behavior of wood constituents is extremely relevant, because it is believed that self-assembly behavior is responsible for the composite structure of wood.[44]

2.1.3.3 Self-Assembly Behavior of Xylans

The aim of this thesis is to study the self-assembly and adsorption of xylan and its derivatives onto a cellulose surface. There have been numerous investigations[52-54] about the self-assembly of xylan onto cellulose surfaces. Mora et al.[52] investigated the redeposition of xylan molecules onto cellulose microfibrils during the pulping process. Electron micrographs of the cellulose microfibrils taken after treating the xylan deposited cellulose microfibrils with hydrogen bond-disrupting reagents produced the same images as those of pure cellulose microfibrils. This hydrogen bond-disrupting reagent, 4 M aqueous urea solution breaks up the hydrogen bonding between xylan and cellulose microfibrils, and thus regenerates smooth microfibril surfaces. These results demonstrated the role of strong hydrogen bonding in the sorption and retention of xylan aggregates on microfibril surfaces. In a later study, Henrikkson et al.[53] investigated the optimum conditions for the assembly of birch xylan onto cellulose microfibrils. By varying the temperature, pH, and time of the autoclaving experiments, he concluded that temperature and time were the most important parameters, whereas pH was not important in the investigated region. Linder et al.[54] extended the investigation of birch xylan self-assembly by changing the cellulose surfaces from cellulose microfibrils to bacterial cellulose (BC) gels produced by *Acetobacter xylinum*. The BC surfaces retained significantly greater amounts of xylan than the cellulose microfibrils under the same conditions. The morphology of the BC/xylan surfaces revealed globular xylan particles of nanometer scale even after short treatment times by atomic force microscopy. This observation suggested that the mechanism was one in which preformed xylan aggregates adsorbed onto the cellulose surfaces rather than the build-up of multilayers through the sequential adsorption of single xylan molecules.

2.2 Adsorption Phenomena

An increase of the solute concentration in the interfacial region is called adsorption. When adsorption occurs through a chemical bond, the process is called chemisorption, whereas the process of adsorption through physical interactions is termed physisorption. The opposite case, a reduction of concentration in the interfacial region is called negative adsorption or depletion for the case of polymers.[55] Depending on the type of systems in contact, we can consider different types of interfacial regions: liquid/gas, liquid/liquid, solid/liquid, and solid/gas. The material that adsorbs is defined as the 'adsorbate' whereas the material which is in the bulk gas or liquid phase prior to adsorption is defined as the 'adsorptive'. The penetration of adsorbate molecules into a bulk solid phase (also known as the adsorbent) is termed 'absorption'. The terms 'sorption', 'sorbate', 'sorptive' and 'sorbent' are often times used if adsorption and absorption are not clearly distinguishable for a process.[56]

For the adsorption of most vapors onto solid surfaces, the adsorption is spontaneous. Therefore, the Gibbs free energy change due to adsorption (ΔG_{ads}) must be negative. The adsorbed molecules lose a degree of freedom on the surface, as they are restricted to two instead of three directions of motion. Thus, their entropy decreases and the entropy change due to adsorption (ΔS_{ads}) is negative. From the thermodynamic relationship:

$$\Delta G_{ads} = \Delta H_{ads} - T\Delta S_{ads} \tag{2.1}$$

we can conclude that the enthalpy change due to adsorption (ΔH_{ads}) must be negative if the adsorption process is to be spontaneous or that the adsorption process must be exothermic. The situation may be different for adsorption from solution due to the effects of solvency, etc. The exothermic nature of adsorption of gases onto solid surfaces explains why the amount of

adsorbed gas decreases when the temperature increases.[57] In the next section, we will analyze the thermodynamic treatment of interfaces.

2.2.1 Thermodynamic Treatment of Interfaces - The Gibbs Adsorption Isotherm

The presence of a surface affects all the thermodynamic parameters. Consider a liquid in equilibrium with its vapor. The change across the boundary between the two bulk phases, α and β, is not sharp and the local pressure and density vary along the interface. Figure 2.10 illustrates the change in some general property (P) between two bulk phases α to β, where z is the distance measured along a line normal to the interface. Gibbs developed a thermodynamic model for analyzing a two phase system by assigning a dividing surface, σ. This dividing surface is a mathematical plane with no thickness in the third (z) direction. In a real system, the interface between two bulk phases, α and β, is not a plane in the mathematical sense, but a zone of thickness where properties of the system continuously change from characteristic values of P for the α phase to characteristic values of P for the β phase. Therefore, the total volume of the system becomes

$$V = V^{\alpha} + V^{\beta} + V^{\sigma} \tag{2.2}$$

where V^{α}, V^{β}, and V^{σ} are the volumes of the α and β phases and the interfacial region. For the case of the Gibbs dividing surface the interface is perfectly sharp. Under this condition, $V^{\sigma} = 0$ and the α and β phases are defined relative to the dividing surface, σ, which is just a plane.

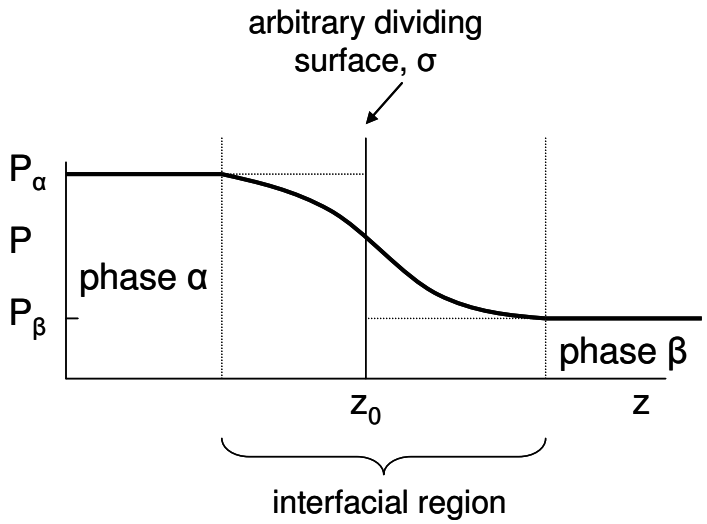

Figure 2.10: Variation of a general property (P) in the vicinity of an interface between bulk phases α and β with respect to position (z) measured along a line normal to the interface.

It is possible to obtain values for extensive properties of the two bulk phases (Gibbs free energy, internal energy, entropy, etc.) because these extensive properties have constant molar values outside the interfacial region. The difference between the values for the bulk regions and the total value of a thermodynamic variable for the entire system allows one to assign a value to the interfacial region. For the case of the surface internal energy,

$$U^{\sigma} = U - u^{\alpha}V^{\alpha} - u^{\beta}V^{\beta} \tag{2.3}$$

where U represents the total internal energy of the system, u^{α} and u^{β} are the internal energy per unit volume of the bulk phases α and β, respectively. Similar surface quantities can be defined for other extensive thermodynamic properties.

Because the molecular composition changes across the interface, the number of moles of component i per unit volume in each phase, n_i^{α} and n_i^{β}, in a two-phase multicomponent system can be defined as

$$n_i^{\alpha} = c_i^{\alpha} V^{\alpha} \text{ and } n_i^{\beta} = c_i^{\beta} V^{\beta} \tag{2.4}$$

where c_i^{α} and c_i^{β} represent the concentration of the solute in bulk phases of α and β with volumes of V^{α} and V^{β}, respectively. The amount of component i in the interfacial region is

$$n_i^{\sigma} = n_i - n_i^{\alpha} - n_i^{\beta} \tag{2.5}$$

where n_i is the total number of moles of species i in the entire system. Here, we can define surface concentration or surface excess for component i:

$$\Gamma_i = \frac{n_i^{\sigma}}{A^{\sigma}} \tag{2.6}$$

where A^{σ} is the cross-sectional area of the dividing surface. It should be kept in mind that Gibbs approach is a model that explains the mathematical handling of data, and does not imply that the surface excess of i is actually physically located on the dividing surface, σ. The reason is that molecules of i are three dimensional and cannot occupy a two dimensional mathematical plane. Eqn. 2.5 makes it clear that n_i^{σ} and thus Γ_i can be either positive or negative. By varying the location of the dividing surface, z_0, the magnitude and sign of the Γ_i can change dramatically.

The total differential of the surface internal energy is

$$dU^{\sigma} = TdS^{\sigma} + \gamma dA^{\sigma} + \sum \mu_i(T) dn_i^{\sigma} \tag{2.7}$$

where γ is the interfacial tension. In Eqn. 2.7, γdA^{σ} replaces the bulk work term PdV, where P is the pressure of the system, because the interface has no volume but does have an area. At equilibrium, the bulk and surface have the same temperature, T and components at the surface have the same chemical potential, μ_i they have in bulk. If we integrate Eqn. 2.7 over a finite area of constant T, γ, and μ_i (T), we obtain

$$U^{\sigma} = TS^{\sigma} + \gamma A^{\sigma} + \sum_i \mu_i(T) n_i^{\sigma} \tag{2.8}$$

Taking the total differential of Eqn. 2.8 and subtracting Eqn. 2.7 yields

$$S^{\sigma} dT + A^{\sigma} d\gamma + \sum_i n_i^{\sigma} d\mu_i \tag{2.9}$$

At constant temperature, Eqn. 2.9 gives the Gibbs adsorption isotherm:

$$-d\gamma = \sum_i \frac{n_i^{\sigma}}{A^{\sigma}} d\mu_i = \sum_i \Gamma_i d\mu_i \tag{2.10}$$

which relates the surface tension change ($d\gamma$) to the chemical potential changes ($d\mu_i$) through the surface excesses (Γ_i). For a two component system of solvent (1) and solute (2), Eqn. 2.10 becomes

$$-d\gamma = \Gamma_1 d\mu_1 + \Gamma_2 d\mu_2 \tag{2.11}$$

Figure 2.11 illustrates how concentrations of solute and solvent might vary across a liquid/vapor interface. The dividing plane is drawn so that the two areas shaded in full strokes are equal, and the surface excess of solvent is thus zero, $\Gamma_1 = 0$. The area shaded with dashed strokes, which lies to the right of the dividing plane minus the smaller area which lies to the left of the dividing plane gives positive surface excess values for the solute.

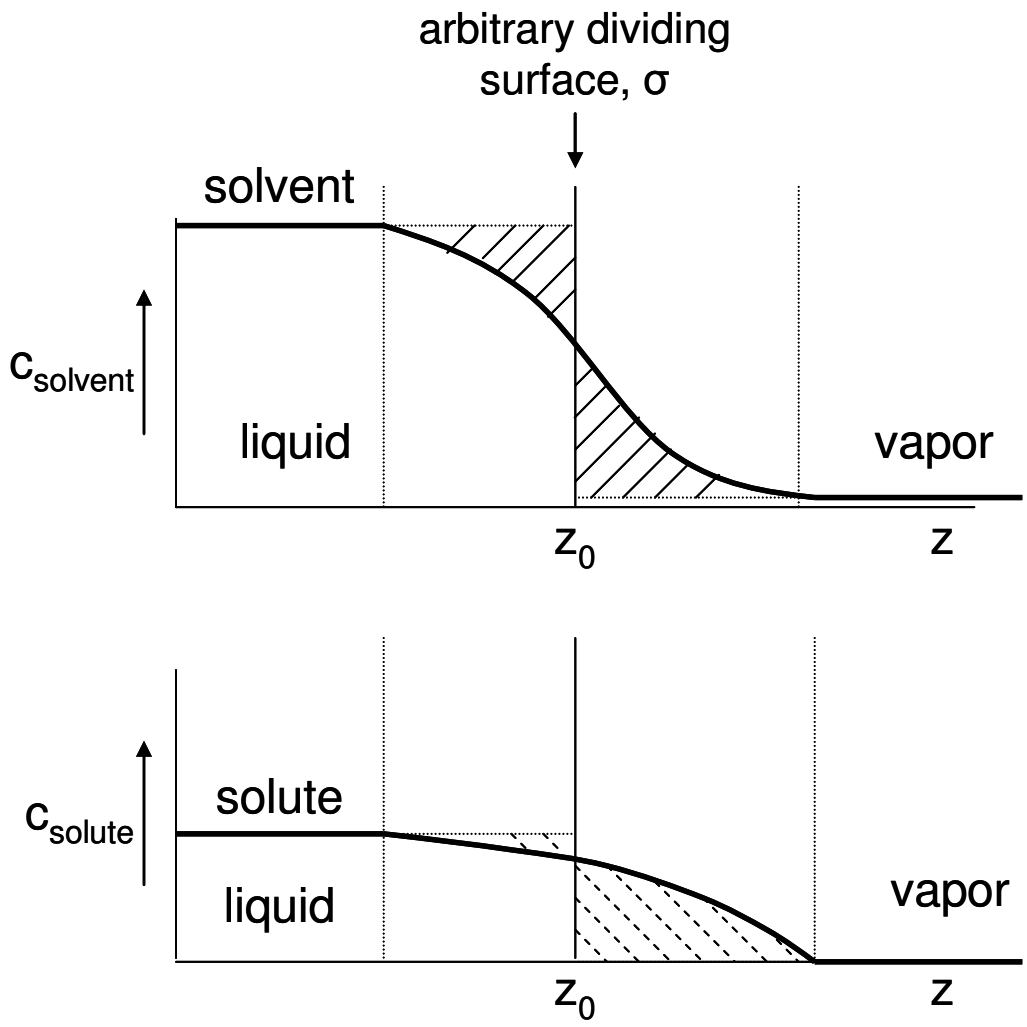

Figure 2.11: Schematic illustration of surface excess. c is the concentration of the solvent (top) or solute (bottom) at a liquid interface, and z_0 is the position along the surface normal.

Therefore, choosing the position of the dividing plane, z_0, in a place that $\Gamma_1 = 0$, converts Eqn. 2.11 into

$$\Gamma_2 = -\frac{d\gamma}{d\mu_2} \tag{2.12}$$

where Γ_2 corresponds to the surface excess or surface concentration of the solute. We can substitute the activity for chemical potential of the solute through

$$d\mu_2 = RTd\ln a_2 = RTd\ln x_2\gamma_2 \tag{2.13}$$

where a_2 is the activity of the solute in the solvent, x_2 is the mole fraction of the solute in the solvent, and γ_2 is the activity coefficient of the solute in the solvent. This substitution yields

$$\Gamma_2 = -\frac{1}{RT}\frac{d\gamma}{d\ln a_2} = -\frac{1}{RT}\frac{d\gamma}{d\ln x_2\gamma_2} \tag{2.14}$$

Finally, for ideal (dilute) solutions, the activity coefficient (γ_2) approaches unity, such that the mole fraction of the solute (x_2) can be replaced by the molar concentration of the solute (c_2) to obtain

$$\Gamma_2 = -\frac{1}{RT}\frac{d\gamma}{d\ln c_2} \tag{2.15}$$

Eqn. 2.15 is the relationship between the experimentally measurable quantities (e.g γ, c_2 and T) to the surface concentration or surface excess of the solute (Γ_2).[57-60] Later, in Chapter 6, we will use Eqn. 2.15 to estimate the surface excess of hydroxypropyl xylans at the air/water interface.

2.2.2 Adsorption onto Solid Surfaces

In the previous section, the Gibbs adsorption isotherm permited the calculation of the adsorbed amount at liquid/vapor interfaces from surface tension measurements. For adsorption onto solid surfaces, this experimental advantage is missing, however, a thermodynamic explanation for the driving force for adsorption also exists. The surface excesses or adsorbed amounts for solid surfaces must be obtained from other measurements.[58] The fundamental concept in adsorption science is the adsorption isotherm. It is the equilibrium relationship between the amount of adsorbate and the pressure or concentration of the bulk fluid phase at constant temperature.[56]

A simple model describing the adsorption of gas molecules onto planar surfaces was introduced by Langmuir in 1918.[61] The key assumptions of the Langmuir adsorption isotherm

are non-interacting, equivalent adsorption sites, a homogeneous surface that lacked dislocations or any other structural nonidealities that might induce preferential adsorption, and the maximal adsorption of a single monolayer, whereby an equilibrium constant (K_L) was the ratio of the adsorption rate constant (k_{ads}) to the desorption rate constant (k_{des}).[60] These assumptions were most often valid for gas adsorption onto solid surfaces. The mathematical expression of the Langmuir isotherm for adsorption from dilute solutions is

$$\Gamma = \frac{\Gamma_m \bullet K_L \bullet C}{1 + K_L \bullet C} \tag{2.16}$$

where K_L is the Langmuir constant, C was the bulk concentration of the adsorbate in solution, and Γ_m is the limiting surface concentration at infinite bulk concentration.[62] The linearized form of the Langmuir adsorption isotherm is

$$\frac{1}{\Gamma} = \frac{1}{\Gamma_m} + \frac{1}{\Gamma_m \bullet K_L \bullet C} \tag{2.17}$$

Therefore, plots of $1/\Gamma$ versus 1/C should be linear and values of the Langmuir constant (K_L) and limiting surface concentration at infinite bulk concentration (Γ_m) can be deduced from the slope and intercept. If the plot is not linear, the model is inappropriate for describing the adsorption process.[57]

Even though it is not explicitly stated, the Langmuir adsorption isotherm assumes a homogeneous surface, otherwise K_L values in Eqn. (2.16) would be different for various places of the surface. Attempts to explain surface heterogeneity through theoretical adsorption isotherms have been more successful for the adsorption of gas molecules onto solid surfaces than the adsorption of solutes onto solids from dilute solutions. One probable reason for this difference is that fewer interactions must be considered for a gas than a solution.[58] The Freundlich adsorption isotherm represents an empirical attempt to describe adsorption for

heterogeneous systems.[63] It is possible to derive the Freundlich isotherm by using a model which assumes exponentially increasing heats of adsorption as surface coverage increases.[57] The Freundlich isotherm is given as

$$\Gamma = K_F \bullet C^{1/n_F} \tag{2.18}$$

where K_F is the adsorbent capacity, C is the bulk concentration, and $1/n_F$ is the adsorption affinity constant.[64] A Freundlich adsorption isotherm can describe adsorption behavior in excess of monolayer coverage. A linear form of the Freundlich adsorption isotherm can be obtained from Eqn. 2.18:

$$\ln\Gamma = \ln K_F + \frac{1}{n_F} \bullet \ln C \tag{2.19}$$

where adsorbent capacity, K_F, and the adsorption affinity constant, $1/n_F$, can be obtained from the intercept and slope, respectively. In reality, the Freundlich isotherm does not explain surface heterogeneity, and it is commonly observed that the Langmuir adsorption isotherm can adequately fit experimental data for surfaces where surface heterogeneity is known to be present. In fact, the two isotherms are the same in the limit where $K_LC \rightarrow 0$ and $n_F \rightarrow 1$. The reason for the failings of the Freundlich isotherm are that its derivation assumes highly specific adsorption site energies which may not properly account for surface heterogeneity.[58] Nonetheless, the Freundlich isotherm is still commonly used to fit experimental isotherms that deviate from Langmuir behavior.

2.3 Polymer Adsorption onto Solid Surfaces

Polymer conformations are usually treated as a random walk in a continuous space or lattice. The conformation of a polymer chain for θ solvent conditions can be represented as an unrestricted random walk. Near an impenetrable surface, half of the region which corresponds to these polymer conformations is restricted. This restriction leads to lower conformational entropy

near the surface. If the polymer does not have an affinity for the surface, a depletion layer occurs in the surface region. However, polymers usually accumulate in the surface region despite entropic restrictions.[55] Adsorption takes place only if there are sufficient interactions between polymer segments and the surface to compensate for the loss of conformational entropy. The critical Gibbs free energy for adsorption to occur spontaneously is typically on the order of a few tenths of a kT unit per adsorbed segment. Even if the critical Gibbs free energy for adsorption is slightly exceeded, polymer adsorption occurs tenaciously, and irreversibly. The reason for this behavior is the combined contribution of each segment to the total Gibbs free energy of adsorption for the entire polymer chain.[65] Silberberg[66] et al. introduced the concept of an adsorption energy parameter which is the negative of internal energy change associated with replacing a solvent molecule adsorbed at the surface by a polymer segment. The dimensionless adsorption energy parameter (χ_s) is

$$\chi_s = \frac{(u_1^a - u_2^a)}{kT} \tag{2.20}$$

where u_1^a is adsorption energy of a solvent molecule, and u_2^a is adsorption of a polymer segment. Normally, u_1^a and u_2^a are negative. Negative values of χ_s mean solvent molecules preferentially remain at the surface.[67]

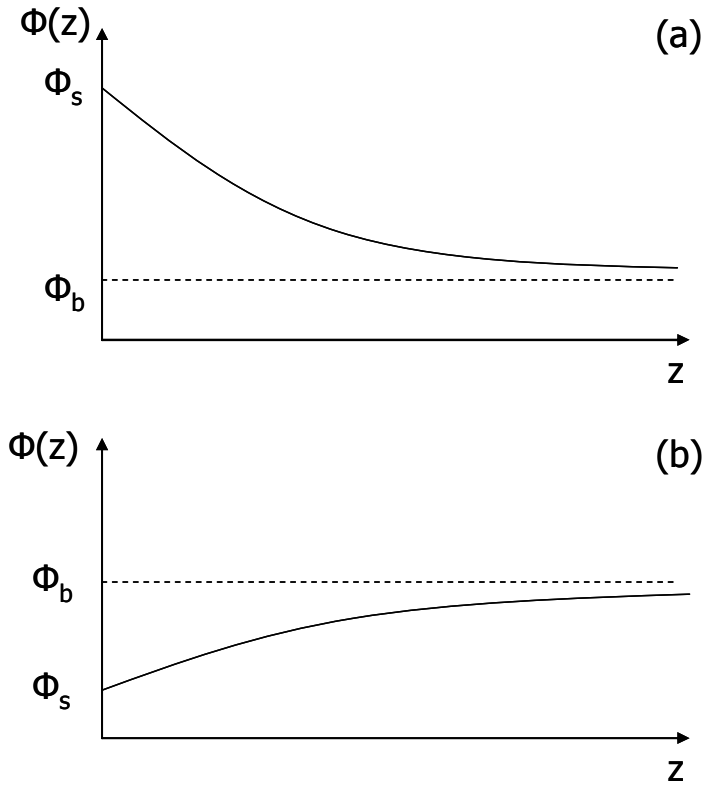

Figure 2.12: Schematic depictions of volume fractions of a solute as a function of distance from a flat substrate for (a) adsorption and (b) depletion. "Reprinted from Physics Reports, 380, Roland R. Netz and David Andelman, Neutral and charged polymers at interfaces, 1-95, Copyright (2003), with permission from Elsevier."

Figure 2.12 demonstrates the volume fraction profile $\Phi(z)$ of monomers as a function distance from the surface. In the bulk, far away from the surface, the volume fraction of the monomer is Φ_b, whereas near the surface it is Φ_s. Theoretical models try to address questions about the conformations of polymer chains near the surface, the local concentration of polymer chains, and the total amount of adsorbed chains. Figure 2.12 also illustrates the opposite case, depletion, when surface-segment interactions are less favorable than solvent-surface interactions. The concentration in the surface layer is smaller than the bulk concentration ($\Phi_b > \Phi_s$).[68] For

example, polystyrene forms a depletion layer at silanized glass (covered with short aliphatic tails, terminally attached by an Si-O bond to glass) from organic solvents even though it adsorbs to glass.[69]

Figure 2.13 illustrates a widely accepted depiction of polymer chain conformations adsorbed at a surface. Only a small portion of polymer chain segments actually contact the surface, while a substantial fraction of the segments extend into the bulk solution. The different segments of a polymer chain adsorbed at a surface are referred to as trains, loops, and tails. Trains correspond to the consecutive attachment of segments to the surface, loops correspond to the polymer segments which have no contact to the surface, but connect two trains, and tails correspond to the non-adsorbed chain ends and thus extend into the bulk solution. The way in which polymer segments distribute through trains, loops, and tails determine the physical properties of the system.[70]

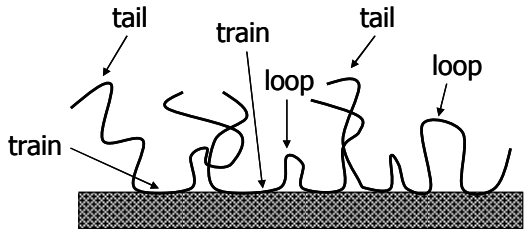

Figure 2.13: Schematic representation of an adsorbed polymer layer where loops, trains, and tails are indicated.

2.3.1 Theoretical Predictions for Polymer Adsorption

Early theoretical treatments of polymer adsorption involved statistical mechanical analyses of random walks of isolated chains near a surface.[71-75] In these treatments, interactions between polymer segments were neglected, an important failing as segment concentration near the surface could be very high, even for adsorption from dilute solutions.[76] Later, de Gennes[77, 78] investigated the adsorption of a flexible polymer onto a planar surface using scaling theory.

Scheutjens and Fleer[70, 76] first attempted to calculate how the distribution of loops, tails, and trains affected adsorbed layer properties through a quasi-crystalline lattice model. Monte Carlo simulations[79, 80] were also applied to polymer adsorption for comparison to both statistical mechanical theories and experimental observations.

2.3.1.1 Mean (Self-consistent) Field Approaches

The most versatile model used for the theoretical study of polymer adsorption was the Scheutjens-Fleer self-consistent field lattice model.[81] The Scheutjens and Fleer (SF) theory was based on a lattice model and space was divided into layers of lattice sites parallel to the planar surface. Each lattice site was occupied by a polymer segment or solvent molecule which were assumed to have equal sizes. Attractions between polymer segments and solvent molecules (characterized by a Flory-Huggins interaction parameter, χ) mediated site exclusion (repulsion). The use of a random mixing approximation within each layer represented a mean-field attempt to account for interactions of segments separated by great distances along the contour of the chain, that still lied in close spatial proximity. Segments in the first layer contacted with the surface received an additional energy increment of $\chi_s \bullet kT$ which characterized the adsorption strength of segments relative to solvent molecules.[82] In most cases, the grand canonical partition function was calculated for large numbers of conformations of each adsorbed polymer chain. By maximization of the partition function, the free segment weighting factor for a segment in a given layer could be derived through its potential energy. This potential energy arose from the entropy of mixing, the tendency of segments to accumulate in layers of high segment concentration, and the preferential adsorption of one segment over a solvent molecule. Therefore, the segment density profile in the adsorbed polymer was calculated from the volume fraction in a given layer, which resulted from the contributions of the chain segments.[83]

On the other hand, SF theory bore some limitations. The model equations were cast in a finite difference form that facilitated a numerical solution but failed to explain some of the underlying physics. The division of space into discrete lattice layers, which necessitated the selection of a particular lattice geometry, was an artificial approximation that may not have accurately reflected the reality of continuous space. The consequences may have been the most severe near the surface, where segment-surface interactions happened on a length scale comparable to the spacing between lattice layers.[82] In order to overcome these limitations, Russel and co-workers[82, 84] introduced an analytical formulation based on a self-consistent field (SCF) approach originally developed by Edwards[85] for polymer solutions. In the SCF approach, polymer walks in a potential field that depended on local concentrations were considered. It was called self-consistent because the potential field depended on the local concentration and these local concentrations depended on the potential field. Self-consistent equations could be solved if a suitable relationship between the field and local concentration was formulated.[55] Next, some of the predicted results for homopolymer adsorption obtained from theoretical calculations based on Scheutjens and Fleer (SF) theory will be discussed.

The volume fraction profile predicted by SF theory was demonstrated in Figure 2.14. The parameters for the calculations were provided in the figure legend. The loops were located in the inner region, while segments of tails dominated the outer region. The hydrodynamic layer thickness, the ellipsometric layer thickness, the average length of tails and loops as well as the total adsorbed amount of polymer expressed by volume fraction (Φ_{ads}) were calculated from the corresponding volume fraction profile ($\Phi(z)$) where z was the distance from the surface along the surface normal. Comparison of adsorbed amount and ellipsometric thickness yielded good qualitative agreement between theoretical calculations and experimental measurements.[83]

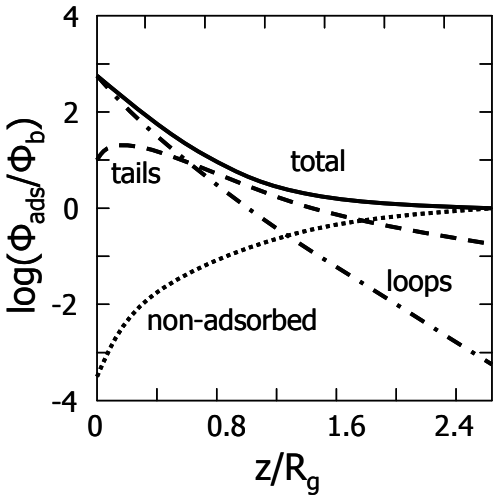

Figure 2.14: Segment density profiles predicted by SF theory for $r = 10^4$, $\chi_s = 1$, $\chi = 0.5$, and $\Phi_b = 10^{-4}$. The logarithmic y-axis was scaled with respect to Φ_b, whereas the x-axis was scaled with respect to the radius of gyration of an ideal chain, R_g. "Reprinted from Advances in Colloid and Interface, 37, Masami Kawaguchi and Akira Takahashi, Polymer adsorption at solid-liquid interfaces, 219-317, Copyright (1992), with permission from Elsevier."

Adsorbed amount (Γ) is one of the basic parameters for characterizing polymer adsorption. However, its measurement is often ambiguous and its determination over a wide concentration range is scare. Figure 2.15a demonstrates the dependence of Γ, expressed in equivalent monolayers, on bulk volume fraction, Φ_b, theoretically predicted by SF theory. Theoretical curves show typical high-affinity isotherms with nearly flat plateaus over a wide concentration range. In θ solvents, Γ at this pseudo-plateau depends on chain length (r). In good solvents, the dependence of Γ on r is weaker than in poor solvents. Stronger adsorption from poor solvents arises from polymer segments that can accumulate in the surface region more easily because of effectively weaker repulsions between segments.[55] Figure 2.15b demonstrates the experimental observations for the dependence of Γ on equilibrium concentration (c_b) for

dextran adsorption onto silver iodide at different molecular weights. The plateau values increases with the molecular weight of the dextran which is in qualitative agreement with theoretical predictions.[86]

The dependence of Γ on chain length for the pseudo-plateau region is presented in Figure 2.16. The solid curves represent the theoretical predictions of SF theory for three adsorption energies (χ_s=0.6, 1, and 3) in a θ-solvent (χ = 0.5) and two curves for better solvents (χ=0.4 and 0). In good solvents (χ = 0), Γ is small and independent of chain length at longer chain lengths. In a poorer solvent (χ = 0.4), Γ is larger because of weaker repulsions between segments and increases with chain length. In a θ-solvent, Γ linearly depends on chain length (r > 100) for all χ_s. Increasing adsorption energies cause Γ to increase and shift the linear sections of Figure 2.16 to smaller chain lengths. This increase in Γ is more pronounced in the unsaturated regime.[55]

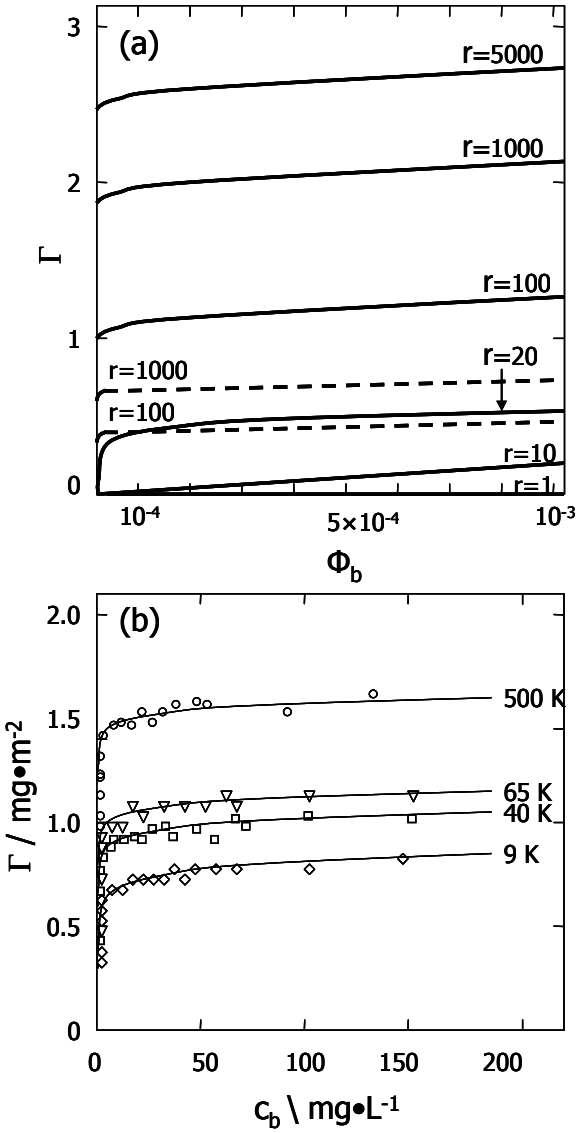

Figure 2.15: Theoretical and experimental adsorption isotherms for polymers of different molecular weight. Graph (a) shows Γ, expressed in equivalent monolayers, predicted by SF theory at various r values versus bulk volume fraction. Solid lines correspond to theta solvent conditions (χ = 0.5) and dashed lines correspond to good solvent conditions (χ = 0). For both calculations, χ_s = 1. Graph (b) corresponds to experimental data for dextran adsorption onto silver iodide.[86] Adapted from Fleer et al.[55]

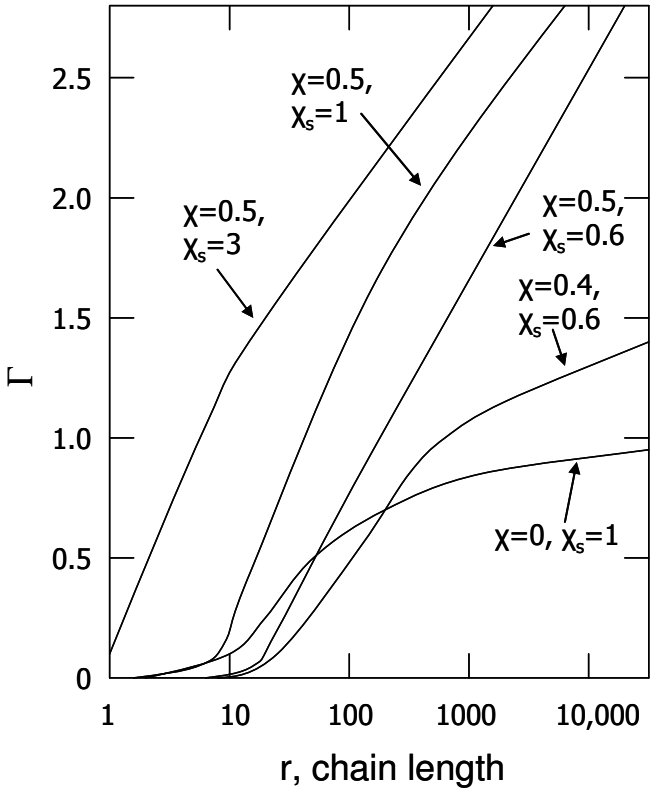

Figure 2.16: Adsorbed amount, Γ, expressed in equivalent monolayers, versus chain length, r, on a semilogarithmic scale. Solid curves are predicted by SF theory for $\Phi_b = 10^{-3}$ at various χ and χ_s values. Adapted from Fleer et al.[55]

2.3.1.2 Scaling Theory Approaches

By using scaling theory, de Gennes[87] predicted that long, linear, flexible chains strongly adsorbed onto a solid wall in a good solvent in the semi-dilute concentration regime to form a self-similar diffuse adsorbed layer. The concentration profile in the adsorbed layer could be divided into three distinct regions. In the proximal region, the short-range forces between the segments and the wall were important and the segment density profile ($\Phi(z)$) did not vary significantly with concentration. Eisenriegler et al.[79, 88] showed that in the proximal region, $\Phi(z)$ decayed as a power law $\Phi(z) \sim z^{-m}$, where the critical exponent was $m \approx 1/3$, a value that reflected the competition between the adsorption energy parameter, chain entropy, and excluded-volume

interactions. In the central region, Φ(z) was universal and did not depend on the bulk polymer concentration (Φ_b). In this region, Φ(z) decayed as a power law $\Phi(z) \sim z^{-m}$ where the critical exponent was $m \approx 4/3$. This relationship arose from the fact that the correlation length (ζ (z)), the local mesh size of the semi-dilute polymer solution, scaled with distance from the surface (z), with only one relevant length scale, $\zeta(z) \sim z$.[68, 89] Experimentally this relationship was confirmed by neutron scattering experiments for the adsorption of monodisperse poly(dimethylsiloxane) (PDMS) onto mesoporous silica[90] and at the liquid/air interface.[91, 92] In the distal region, the excess polymer concentration decayed exponentially to the bulk value:

$$\phi(z) - \phi_b \approx 4\phi(z)\exp(-2z/\xi^b) \tag{2.21}$$

where ζ^b was the bulk correlation length.

2.4 Polyelectrolyte Adsorption

Polyelectrolytes can be defined as linear macromolecular chains bearing a large number of ionic or ionizable groups upon dissolution in a suitable polar solvent, generally water.[93, 94] Well known examples of such systems include proteins, nucleic acids, and synthetic sytems such as polyacrylic acid and sulfonated polystyrene.[93] Polyelectrolytes exhibit solution properties that differ from uncharged macromolecules and low molar mass electrolytes. The origin of this behavior comes from the interplay of high molecular weight chains and electrostatic interactions.[94] Both long-range (Coulombic) interactions and short-ranged (excluded volume) interactions are present in polyelectrolyte solutions. The presence of these long-range interactions makes it difficult to apply theoretical models such as scaling concepts and renormalization group theories to polyelectrolytes in contrast to neutral polymers.[93] Here, a brief discussion of the solution behavior of polyelectrolytes will be discussed as it is important for understanding polyelectrolyte adsorption.

2.4.1 Dilute Solution Behavior of Polyelectrolytes

Extensive knowledge has been accumulated for the dilute solution behavior of polyelectrolytes in aqueous solutions.[95] Forster et al. looked at the dependence of electrostatic persistence length (l_{pc}) on the ionic strength of aqueous solutions of poly (2-vinylpyridinium benzylbromide) (PVP) by using static and dynamic light scattering. It was observed that electrostatic persistence length, which is a measure of chain stiffness, increased with decreasing salt concentration.[96] Extended chain conformations at low salt concentrations were also observed for DNA and sodium poly(styrenesulfonate).[97] Previously mentioned long-range electrostatic interactions have led to the clustering of polyelectrolytes as determined by small angle x-ray scattering for sodium polyacrylates[98] which has made it difficult to visualize single chain behavior for polyelectrolytes. Authors claimed that these clusters formed through electrostatic attractions between polyelectrolytes mediated by counterions (gegenions) that sat between the polyelectrolyte chains.[98]

If an inert salt like NaCl was added to a polyelectrolyte solution, strong electrostatic interactions were screened and highly expanded polyelectrolyte chains started to shrink.[95] Electrostatic interactions were exponentially screened on length scales larger than the Debye screening length (κ^{-1}):

$$\kappa^2 = \frac{4\pi \bullet e^2}{\varepsilon \bullet k_B \bullet T} \sum c_s \bullet q_s^2 \qquad (2.22)$$

where ε was the dielectric constant of the medium, k_B was the Boltzman constant, T was the absolute temperature, e was the elementary charge on an electron, c_S was the concentration of the small ions of type s, and q_s was their valence. In a dilute, salt-free solution, the concentration of counterions was very low, and the Debye screening length was larger than the size of the chain. Therefore, ionic groups on a polyelectrolyte chain could interact with each other through an

unscreened Coulombic potential.[99] The unperturbed dimensions were reached if a large enough concentration of inert salt was added to the polyelectrolyte solution.[100, 101] Therefore, variation of the salt concentration provided a mechanism for the achievement of good and θ-solvent conditions for polyelectrolyte chains. Recently, Scweins et al.[102] investigated the coil size as a function of molar mass for dilute aqueous solutions of sodium poly (acrylate) at two salt concentrations (0.1 M NaCl and 1.5 M NaCl) by static and dynamic light scattering. In 0.1 M NaCl, the polyelectrolyte was in a good solvent ($R_g \sim M_w^{0.60}$), while 1.5 M NaCl was close to a θ-solvent for the polyelectrolyte ($R_g \sim M_w^{0.52}$). A further increase in the salt concentration led to phase separation.[103, 104] The latter phase separation was called salting-out and was also called H-type precipitation, because the amount of salt required for polyelectrolyte precipitation was high and independent of polymer concentration.[105]

2.4.2 General Features of Polyelectrolyte Adsorption

When charges are present on a macromolecule near a surface, adsorption is strongly affected by electrostatic interactions. When the polymer is charged, electrostatic repulsion between polymer segments at the surface oppose the accumulation of segments near the surface. On the other hand, if the surface is charged, electrostatic contributions to the adsorption energy parameter increase or decrease the adsorption depending on the sign and magnitude. Because salt groups screen electrostatic forces, the salt concentration of a polyelectrolyte solution becomes an important parameter for controlling adsorption. pH is also an important parameter if the ionized groups of the polyelectrolyte and surface are weak electrolytes.[55] In summary, the main factors that govern polyelectrolyte adsorption are salt concentration (c_s), surface charge density (σ_0), linear charge density of the polyelectrolyte (τ), and nonelectrostatic interactions between the surface and the polyelectrolyte.[106]

2.4.3 Theoretical Predictions and Experimental Observations for Polyelectrolyte Adsorption

Most early polyelectrolyte adsorption theories have used nonionic polymer adsorption theories as a foundation for the partition function and then added electrostatic interactions. Hesselink et al.[107] developed a polyelectrolyte adsorption theory through the extension of the theory of Hoeve[108, 109] for the adsorption of uncharged polymers. The predicted adsorption isotherm had a high-affinity character where the adsorbed amount rose very steeply and saturated at very low polyelectrolyte concentrations. Hesselink's theory predicted that increasing salt concentration generally increased the adsorption, however, increased salt concentration actually decreased the adsorption if electrostatic interactions were the main driving force for adsorption. Lyklema and Van der Schee[110] extended the polymer adsorption theories of Roe[67] and Scheutjens and Fleer[70, 76] to polyelectrolyte adsorption. This approach predicted that fully charged polyelectrolytes formed thin adsorbate layers on oppositely charged surfaces at low ionic strengths and that the dependence of the adsorbed amount on the chain length was minimal. In a subsequent study, Papenhuijzen et al.[111] predicted that at high salt concentrations, the adsorbed amount increased more strongly with ionic strength and molecular weight than it did at low salt concentrations. Furthermore, their work predicted the nonelectrostatic segment-solvent interaction parameter (χ) became more important for adsorption at high salt concentrations, and the nonelectrostatic adsorption energy parameter (χ_s) was important over the entire salt concentration regime.[111]

The theory of Lyklema and Van der Schee[110] has been applied to the case of weak polyelectrolytes.[112-114] Evers et al.[112] calculated the adsorbed amount as a function of solution pH for the adsorption of a weak polyacid onto a surface that had different amounts of constant

surface charge. If the polyelectrolyte and the surface were oppositely charged, a maximum in the adsorbed amount occurred around the pK_a where the degree of dissociation (α) of the acidic protons varied strongly. This maximum was situated slightly below the pK_a of the polyacid and occurred only if χ_s was not too large.[112] At the maximum, the surface charge density was about the same as the charge density of the polyelectrolyte. The overall charge of the polyelectrolyte and the lateral repulsion between segments was small.[113] The existence of this maximum in adsorbed amount was later tested experimentally by Blaakmeer et al.[115] for poly(acryclic acid) (PAA) adsorption onto a positively charged cationic polystyrene latex. The polystyrene latex contained quarternary amine groups which made the surface charge density (σ_0) constant over the studied pH range. At high pH, where PAA was fully charged, the adsorbed amount was low. With decreasing pH, the adsorbed amount increased and passed through a maximum at about one pH unit below the pK_a of the carboxylic acid groups of PAA. The ionic strength effects on the adsorbed amount for weak polyelectrolytes was small compared to strong polyelectrolytes.[115]

Van de Steeg et al.[116] defined two regimes for the dependence of polyelectrolyte adsorption on salt concentration: screening-enhanced adsorption and screening-reduced adsorption. In order to grasp this distinction, Γ_0 was the adsorbed amount at very low salt concentration where electrostatic screening was negligible, and Γ_∞ was the adsorbed amount at very high salt concentrations where electrostatic interactions were virtually eliminated. For the screening-reduced adsorption regime ($\Gamma_0 > \Gamma_\infty$), electrostatic attractions between the segment and surface were dominant. Γ decreased with increasing salt concentration because the salt screened the electrostatic attraction and reduced the adsorption. In the screening-enhanced adsorption regime ($\Gamma_0 < \Gamma_\infty$), nonelectrostatic interactions between the segment and the surface were dominant. Γ increased with increasing salt concentration because the salt screened the repulsion

between segments and enhanced adsorption. SF theoretical predictions for polyelectrolyte adsorption onto oppositely charged surfaces, where nonelectrostatic interactions between the surface and the polymer segment were omitted ($\chi_s = 0$) were provided in Figure 2.17. Figure 2.17a illustrated that for all linear charge densities, (τ), screening-reduced adsorption was observed. Figure 2.17b and 2.17c showed adsorbed amount (Γ) increased from $\tau = 0$ to $\tau = 0.015$ and then decreased if τ increased further for different salt concentrations. The sharpest peak occurred at low salt concentrations.[116]

Experimentally, screening-reduced adsorption was observed for the adsorption of cationic derivatives of polyacrylamide onto cellulose fibers,[117, 118] cationic copolymers of acrylamide onto silica,[119, 120] and poly-L-lysine onto mica powder.[121] Screening-enhanced adsorption was observed for the adsorption of poly(4-vinyl-*N*-*n*-propylpyridinium bromide) (PVPP) with complete quaternization adsorption onto silica at pH = 4. Durand et al.[122] observed both screening-reduced adsorption and screening-enhanced adsorption for the adsorption of copolymers of acrylamide and an acrylate with a quarternary ammonium group onto montmorillonite (clay). With a cationic monomer content of just 1%, the adsorbed amount decreased with increasing salt concentration. At intermediate cationic monomer contents (5%), the adsorbed amount did not vary with salt concentration. However, at even higher cationic monomer content (13% and 30%) the adsorbed amount actually increased with increasing salt concentration.[122]

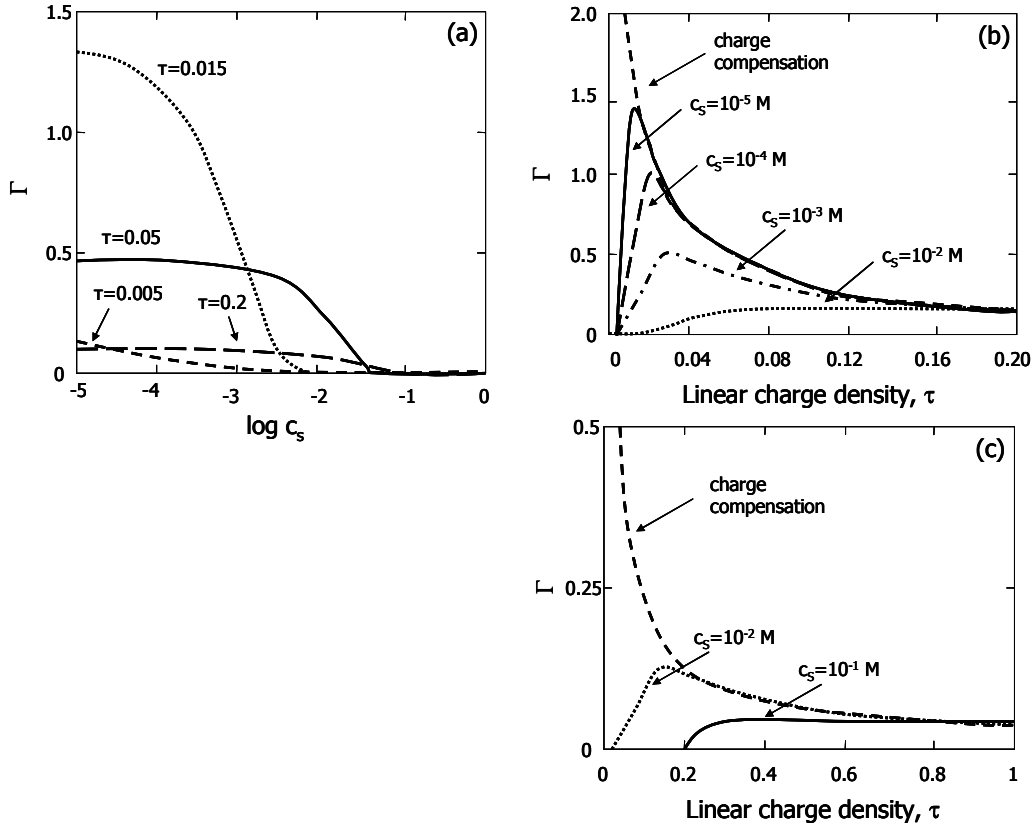

Figure 2.17: SF theoretical predictions for the adsorption of a polyelectrolyte of 100 segments onto an oppositely charged surface (σ_0=-0.01 C•m^{-2}). Adsorbed amount (Γ) is represented in equivalent monolayers. (a) The dependence of Γ on electrolyte concentration for different linear charge densities of the polyelectrolyte. (b) and (c) The dependence of Γ on linear charge densities of the polyelectrolyte at different salt concentrations. The only difference between (b) and (c) is the scale. Dashed curves in (b) and (c) represent the adsorbed amount needed for charge compensation. Reprinted with permission from *Langmuir* **1992**, *8*, 2538-2546. Copyright [1992] American Chemical Society.[116]

Recent theoretical interest in polyelectrolyte adsorption stems from the importance of understanding and controlling the formation of polyelectrolyte multilayers through successive deposition of positively and negatively charged particles.[99] Shklovskii[123, 124] argued that mean

field Poisson-Boltzman theory provided inadequate explanation for the self-assembly of many rod-like polyelectrolytes into bundles of parallel densely packed rods. The reason for this problem was that Poisson-Boltzman theory predicted that polyelectrolytes should repel each other. Therefore, the Wigner crystal (WCR) model was proposed where polyelectrolyte rods could be considered as a uniform, negatively charged background onto which condensed ions formed the WCR. The cohesive energy of the crystal was the main reason why polyelecrolyte rods attracted each other.[123] Newer theoretical predictions of polyelectrolyte adsorption divided the adsorbed layer into Wigner-Seitz cells (Figure 2.18) surrounded by each polyelectrolyte chain.[125-129] Dobrynin et al.[126] developed a scaling theory for polyelectrolyte adsorption onto oppositely charged surfaces. He predicted two dimensional (2D) adsorbed layers at low surface charge densities and three dimensional (3D) adsorbed layers at high surface charge densities. 2D adsorbed layers were caused by the balance between the energy gained through electrostatic attractions between charged monomers and the surface and a loss of confinement entropy that arose from chain localization at low surface charge densities. In contrast, 3D adsorbed layers were caused by a balance of electrostatic attractions between charged monomers and the surface and short-range monomer-monomer repulsion at high surface charge densities. The crossover between 2D adsorbed layers and 3D adsorbed layers occurred at $\sigma_e \approx fa^{-2}$ where f was the fraction of charged monomers and a was the bond length.[126]

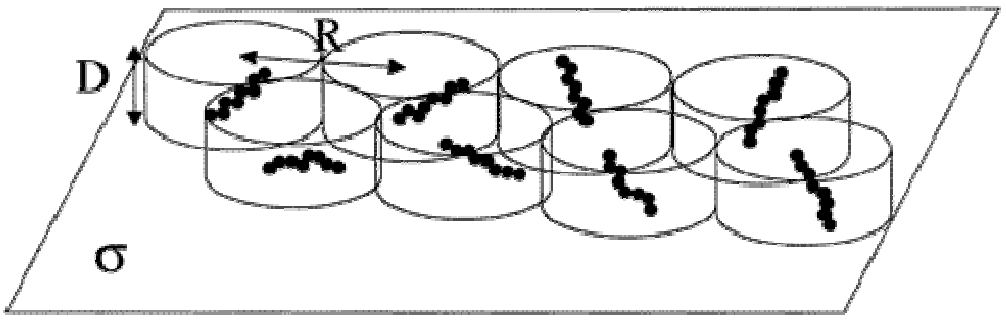

Figure 2.18: Schematic depiction of an adsorbed layer in the dilute 2D Wigner liquid regime (D < R). R is the Wigner-Seitz unit cell size and D is the thickness of the adsorbed layer. Reprinted with permission from *Macromolecules* **2001**, *34*, 3421-3436. Copyright [2001] American Chemical Society.

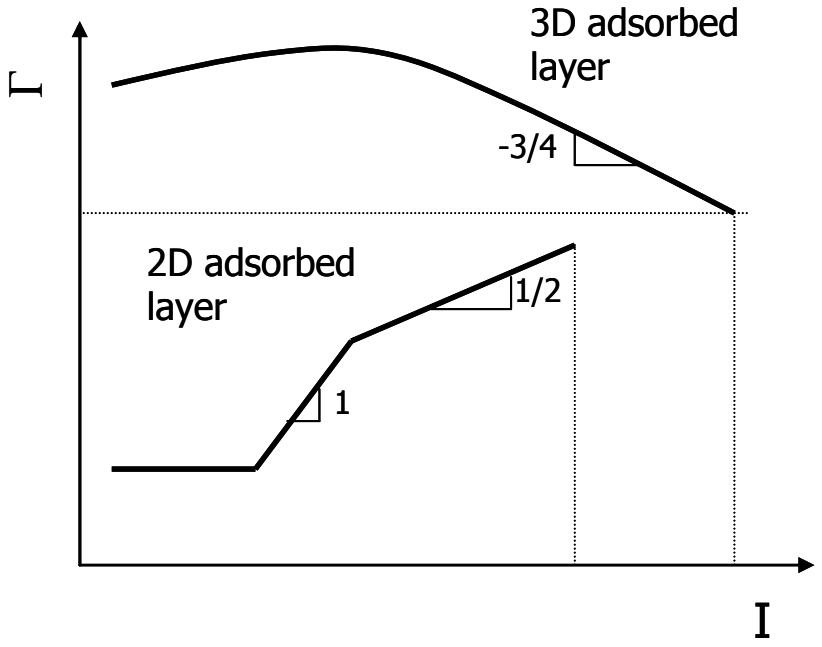

Figure 2.19: Dependence of Γ on ionic strength for a semilogarithmic scale. Predicted scaling exponents are illustrated for 2D and 3D adsorbed layers. "Reprinted from Progress in Polymer Science, 30, Andrey V. Dobrynin and Michael Rubinstein, Theory of polyelectrolytes in solutions and at surfaces, 1049-1118, Copyright (2005), with permission from Elsevier."

The previously mentioned screening reduced adsorption regime and screening enhanced adsorption regime could also be seen in Dobrynin's polyelecrolyte adsorption theory. For a 2D adsorbed layer, added salt screened the repulsion between segments and largely overcompensated the surface charge that led to screening enhanced adsorption. At higher salt concentrations, the adsorbed amount was independent of surface charge, depended on the linear charge density of polyelectrolyte chains (τ), and increased with the square root of the ionic strength (Figure 2.19). For a 3D adsorbed layer, polyelectrolyte adsorption increased at low salt concentrations (screening enhanced adsorption), decreased at higher salt concentrations (screening-reduced adsorption), and exhibited a maximum in the adsorbed amount at intermediate salt concentrations.[99] The previuosly discussed results of Durand et al.[122] for the adsorption of copolymers of acrylamide and an acrylate with a quarternary ammonium group onto montmorillonite could also be explained by Dobrynin's model for polyelectrolyte adsorption. With an increasing fraction of charged monomers (f), the crossover value $\sigma_e \approx fa^{-2}$ shifted to higher surface charge densities. Therefore, the adsorbed polyelectrolye formed a 3D adsorbed layer for $f < 0.05$, and a screening reduced adsorption regime was observed. At $f = 0.05$, the adsorbed amount was independent of salt concentration which indicated that $\sigma \approx \sigma_e$. For $f > 0.05$, adsorbed polyelectrolyte formed a 2D layer and a screening enhanced adsorption regime was observed.[126]

2.5 Surface Analysis Techniques

2.5.1 Surface Tension Measurements

Many kinds of molecules will orient themselves at the interface between a gas and a liquid in order to minimize their free energy. The resulting surface films are nominally a monolayer thick and are called monomolecular layers or monolayers.[130] Monolayers formed by a

substance that is insoluble in the liquid subphase are called Langmuir monolayers, whereas substances that are soluble in bulk liquids may preferentially adsorb to an interface to form Gibbs monolayers.[58] Most of the early studies dealing with Langmuir monolayers were carried out with long chain carboxylic acids such as steraic acid at varying pH.[131, 132] The molecules had to be amphiphilic in order to form Langmuir monolayers on the water surface. These amphiphilic molecules consisted of two dissimilar parts, one part was hydrophilic (usually polar) and is commonly referred to as the "head", and the rest of the molecule was generally hydrophobic, e.g. one or more saturated alkane chains ("tail"). Such asymmetric molecules naturally preferred to stay at the surface of water. If the hydrophobic groups were long enough, the material was insoluble and the molecules on the surface formed an isolated "two-dimensional system", where the hydrophilic head groups stuck into the water, and the hydrophobic tail groups oriented towards the air.[133] We have previously discussed Gibbs thermodynamic treatment of adsorbed layers at interfaces and its relationship to surface tension. Various techniques have been developed for the measurement of the the surface tension of liquids. These were the pendant drop method, maximum-bubble-pressure method, drop weight method, Du-Noüy ring tensiometer, and Wilhelmy plate technique, etc.[134] Here, the Wilhelmy plate method for surface tension measurements of liquids will be discussed.

For the Wilhemy plate technique, absolute forces acting on the plate, usually made of platinum or filter paper and partially immersed in the subphase, are measured (Figure 2.20). Downward forces working on the plate such as gravity and surface tension are balanced by upward forces, buoyancy which results from the displacement of the water by the plate and the pressure sensor itself. These forces are usually measured with a sensitive electrobalance.[135] The surface tension and surface pressure can be calculated from the following equations:

$$\gamma = \frac{F_{obs,0} - W}{2(L+t)\cos\theta} \tag{2.23}$$

$$\Pi = \gamma_0 - \gamma_{film} = \frac{F_{obs,0} - F_{obs,film}}{2(L+t)\cos\theta} \tag{2.24}$$

where $F_{obs,0}$ is the force measured by the wet Wilhelmy plate when there is no film on the surface, $F_{obs,film}$ is the force measured by the Wilhelmy plate when there is film on the surface, W is the gravitational force, L is the width of plate and t is thickness of the plate, which is so small compared to L that it can often be ignored. θ is the contact angle between the liquid subphase and the plate at the interface. The measured surface tension depends on the contact angle of the liquid with the plate, and it is assumed to remain constant at all γ for the calculation of Π. Normally, the plate is completely wetted by the subphase leading to a contact angle value of zero.[130] One important drawback of Wilhelmy plate method is under increasing surface pressure, monolayers may be deposited onto the plate, thereby changing the contact angle. The wetting problem may be avoided by using freshly cleaned filter paper for each monolayer experiment.[135]

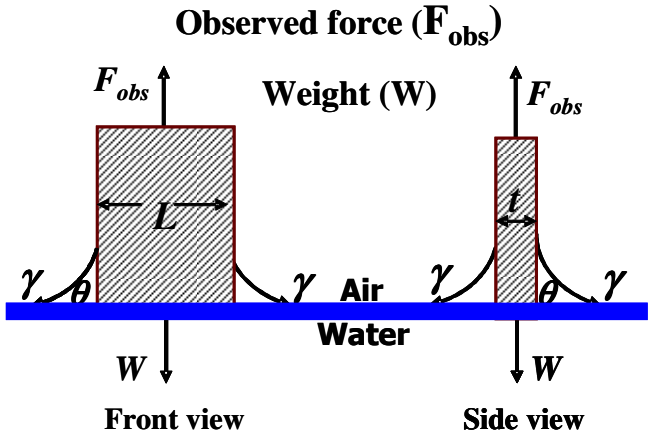

Figure 2.20: Wilhelmy plate technique for measuring surface tension (γ) and surface pressure (Π) at the air/water (A/W) interface.

2.5.2 Model Cellulose Surfaces

In order to study the adsorption of polysaccharides onto the cellulose surfaces, a well-defined cellulose film must be prepared. Schaub et al.[136] were the first group to transfer a cellulose derivative, trimethylsilylcellulose (TMSC), onto a hydrophobized silicon substrate by the Langmuir-Blodgett (LB) technique. TMSC was a cellulose compound with short, hydrophobic side chains. TMSC did not have an amphiphile structure that was comparable to conventional LB-materials, however, it formed homogeneous films and several hundred LB layers of TMSC could be transferred onto hydrophobic substrates. After LB transfer, the in situ conversion of TMSC thin films on silicon substrates to a film of regenerated cellulose film was carried out by short exposure (30 seconds) of the films to the atmosphere above a 10% aqueous HCl solution at room temperature (Figure 2.21).[136] The regeneration process could be followed by a variety of techniques including polarized transmission infrared spectroscopy and X-ray reflectometry (XRR),[136] X-ray photoelectron spectroscopy (XPS),[137, 138] ellipsometry,[139] and contact angle measurements.[139, 140] XRR results showed that the thickness of the film decreased by 60% after desilylation.[136]

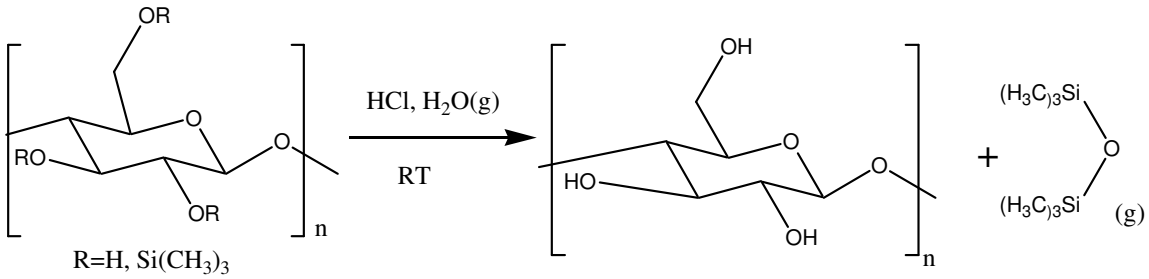

Figure 2.21: Desilylation reaction of TMSC.

Geffroy et al.[141] first applied spincoating technique to produce TMSC thin films on silicon wafers with subsequent hydrolysis to cellulose. Prior to spincoating, the silicon wafers

were treated with an anchoring polymer, polyvinylpyridine-polystyrene block copolymer, in order to promote the the physisorption of the coating to the substrate. Kontturi et al.[142, 143] systematically studied spincoating of TMSC onto different substrates as a function of spincoating parameters such as spinning speed, concentration of the coating solution and the nature of solvent. They found that it was not necessary to pretreat the substrates (silicon or gold substrate) with anchoring polymers to adhere TMSC onto the substrate. After the regeneration process, the chemical structure of the resulting cellulose thin film was close to theoretical values for cellulose as revealed by XPS and attenuated total reflectance infrared spectroscopy (ATR-IR). Atomic force microscopy (AFM) of these films revealed that smoother films could be obtained by spincoating from a nonvolatile solvent (e.g. toluene) compared to a more volatile one (e.g. chloroform). ATR-IR studies of spincoated films on gold also revealed that the resulting cellulose films were largely in an amorphous state[142] which was also previously reported for LB-films.[136]

2.5.3 Self-Assembled Monolayers (SAMs)

Self-assembled monolayers (SAMs) are ordered molecular assemblies that form spontaneously through the chemisorption of surfactants to a solid substrate with specific affinity of the head group to the substrate.[144, 145] Figure 2.22 shows a schematic, including the constituents of a SAM-molecule (head group, alkyl chain spacer or backbone, and tail group). Examples of SAM forming molecules include fatty acids adsorbed onto metal oxides,[146-149] organosilicons adsorbed onto hydroxylated surfaces,[150-155] and organosulfurs adsorbed onto metals.[156-160] The most studied and versatile of these systems are the organosulfur compounds adsorbed onto metals, specifically alkanethiols adsorbed onto gold. Adsorbates offer control over head and tail groups, as well as the overall thickness (i.e. length of the alkyl chain) of the SAM.

SAMs offer well-ordered and highly reproducible thin films that serve as model surfaces for studying organic surface properties.

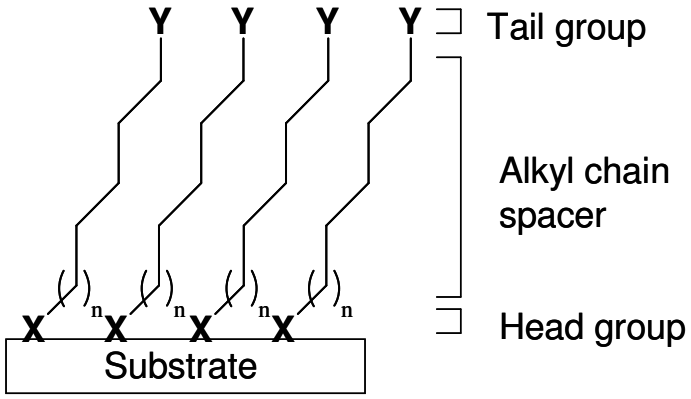

Figure 2.22: Schematic representation of the three components of a SAM. X corresponds to the chemisorbing head group and Y indicates the tail group which can be of widely varying chemical functionality.

Figure 2.23: Oxidative addition of an alkanethiol to gold with subsequent reductive elimination of H_2.

The strong binding of the head group of the SAM forming molecule to the substrate (e.g., S-Au) allows for the preparation of SAMs from the gas phase or from solution.[145] It is believed that the reaction occurs by oxidative addition of the S-H bond to the gold surface, followed by a reductive elimination of hydrogen (Figure 2.23). The protons released combine to form H_2 molecules.[144] This mechanism is consistent with the fact that monolayers can be formed from the gas phase in the absence of oxygen.[161, 162] The adsorbing species is the thiolate ($R\text{-}S^-$) group which has been observed by XPS,[163, 164] Fourier transform infrared (FTIR) spectroscopy,[165] Fourier transform mass spectrometry,[166] electrochemistry,[167] and Raman spectroscopy.[168] The

bonding of the thiolate group to the gold surface is very strong (homolytic bond strength of ~ 44 kcal·mol^{-1}).[169]

The ease of preparation and low cost of solution deposition make SAMs a common approach for surface modification. If the substrate is clean, the substrate should be dipped into the corresponding solution for a period of time, and the monolayer will self-assemble. Alkanethiols in ethanol solution are a good example for the preparation of SAMs from solution.[145] SAM formation on the substrate in a laboratory atmosphere is basically an exchange process between the desired adsorbate and adventitious materials that have adsorbed onto the substrate prior to immersion of the substrate in a thiol solution. Displacement with thiols requires desorption of contaminants and impurities on the surface, thus desorption processes affect the kinetics of SAM formation. SAMs have reproducible material properties if the substrates are put into thiol solution within ~ 1h after substrate preparation or cleaning the substrate with strong oxidizing chemicals (e.g. piranha solution: H_2SO_4:H_2O_2) or oxygen plasmas. Prolonged exposure of the substrates to ambient conditions prior to immersion in a thiol solution slows the desorption of adsorbates from the substrate and essentially prevents SAM formation in the normal time frame.[170] Self-assembled monolayers are relevant for this work, because they can make gold slides hydrophobic or hydrophilic, thereby allowing us to evaluate the relative importance of different functional groups to polysaccharide adsorption onto regenerated cellulose surfaces.

Nuzzo and Allara first demonstrated the adsorption of bifunctional organic disulfides (RS-SR) onto Au (111) surfaces and characterized the structure of the monolayers formed on the gold surface by reflection absorption infrared spectroscopy.[156] This development was crucial for surface studies, because gold did not have a stable oxide and therefore could be handled in ambient conditions. In contrast, silver and copper readily formed oxides that adsorb polar

contaminants. The monolayers formed on all three metals are stable against physical manipulation and washing with polar solvents. However, the monolayers on copper and silver exhibited limited stability in air. Therefore, gold was preferred over other transition metals for the preparation of SAMs from thiols and disulfides.[171]

Porter et al.[157] investigated the adsorption of n-alkyl thiols, $CH_3(CH_2)_nSH$, where n = 1 to 21 (odd integers) onto gold surfaces in ethanol and hexane solutions by ellipsometry, infrared spectroscopy, and electrochemistry. All three techniques showed that there were structural differences between the short-chain and long-chain sulfides. They found that long-chain thiols formed a densely packed crystalline structure and the long alkyl chains were tilted 20 to 30^o from the surface normal (Figure 2.24a). As the chain length of the thiol decreased, the structure became disordered with lower packing densities.[157] The most important step of the adsorption process was chemisorption, where alkanethiols bound to the gold surface. As a result of strong interactions between the head group and the substrate, the molecules tried to bind at every available binding site. After all binding sites were occupied, the alkyl chains assembled into a more energetically favorable conformation. The alkyl chains had a tilted structure in order to minimize the steric repulsions and maximize van der Waal's interactions between the neighboring chains.[172] In a later study, Nuzzo and coworkers studied a number of SAMs with different terminal (tail) groups ($-CH_3$, $-CH_2OH$, $-CO_2H$, $-CO_2CH_3$, and $-CONH_2$) on gold surfaces. Infrared data showed that these SAM molecules, regardless of terminal group, formed densely packed crystalline structures and the alkyl chains were tilted in the range of 28 to 40° from the surface normal.[159]

Electron diffraction[173, 174] and scanning tunneling microscopy (STM)[167, 175] studies of thiol SAMs on gold revealed that the monolayer had a $(\sqrt{3}\times\sqrt{3})R30°$ overlayer (R=Rotated) structure (Figure 2.24b) and surface order extended over areas of hundreds of square nanometers.

The spacing between adjacent sulfur atoms in this structure (4.99 Å) was nearly three times that of the van der Waals diameter of a sulfur atom (1.85 Å); thus sulfur-sulfur interactions were thought to be minimal. This distance was also greater than the distance of closest approach of the alky chains (4.24 Å) which resulted from the previously mentioned tilting of chains with respect to the surface normal that maximized van der Waal's interactions.[169]

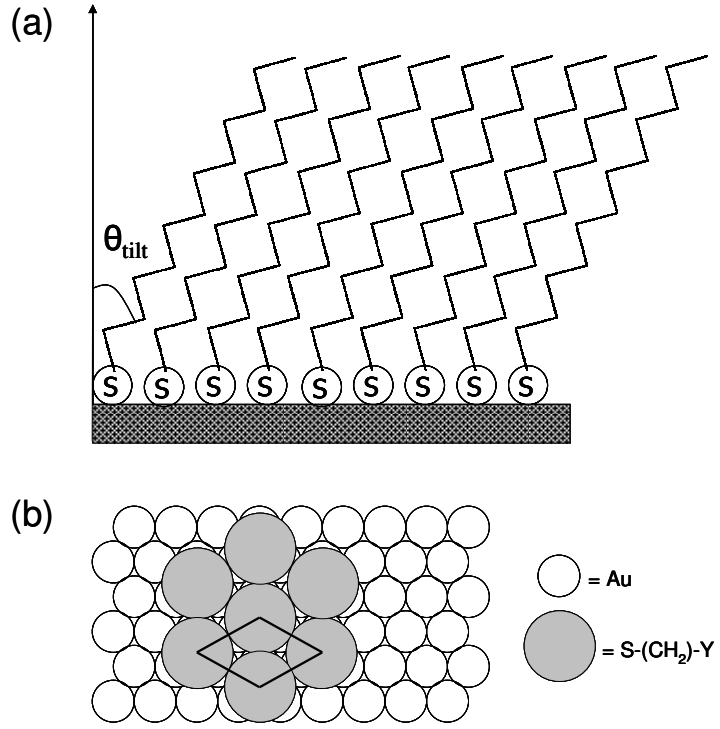

Figure 2.24: Schematic diagram of the structure of alkanethiols adsorbed on Au (111). (a) Depiction of the tilt angle of an adsorbed dodecanethiol monolayer on Au (111). Adapted from Porter et al.[157] (b) The overlayer structure formed by an alkanethiol monolayer on Au (111). The lattice has dimensions of ($\sqrt{3}\times\sqrt{3}$) and is rotated 30° relative to the substrate lattice. Adapted from Dubois et al.[169]

2.5.4 Surface Plasmon Resonance

Surface plasmon resonance (SPR) is a unique optical surface technique which is commonly used in the fields of chemistry and biochemistry to characterize surfaces and monitor

binding events.[176] SPR is an attractive technique in the biosensing field because it is capable of measuring real time interactions between the analyte and an immobilized, functionalized surface.[177] The success of SPR comes from three factors: (a) real time measurement of the biomolecular interactions, (b) adsorption of unlabeled analyte molecules can be monitored, and (c) SPR has a high degree of surface sensitivity which allows one to monitor weak binding sytems.[176] These interactions take place in a fluid medium which can be tailored to mimic interactions encountered in vivo,[178] such as DNA-DNA,[179-181] antibody-antigen,[182, 183] and DNA-protein[184, 185] interactions.

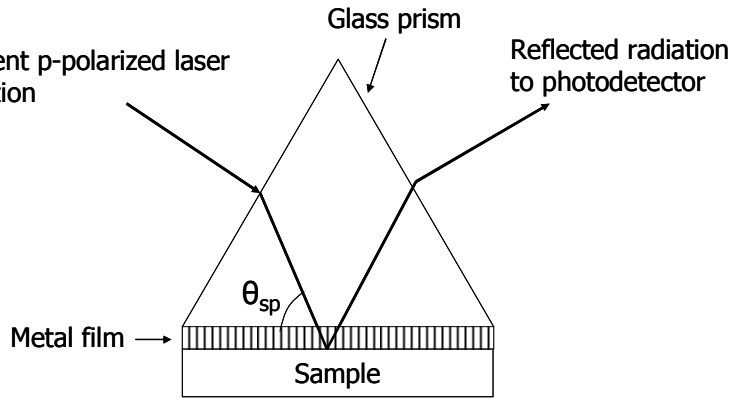

Figure 2.25: Kretschmann prism arrangement. Adapted from Earp et al.[186]

The most frequently used SPR apparatus is the Kretschmann prism arrangement (Figure 2.25), which operates on the principle of total internal reflection.[187] The Kretschmann prism arrangement is a structure where a light ray is coupled into a surface plasmon (SP) mode that can exist on the surface of a thin metal film. Thin gold or silver films are generally used as SP support materials because of the optical qualities and relative ease of deposition of these materials onto a substrate with accurately controlled thicknesses. The metal film is deposited onto a glass substrate that will be optically coupled to a waveguide. For the case of gold, a

chromium layer is deposited between the glass and gold layers to ensure adhesion of the gold to the glass. The main criterion for a material to support SP waves is that the real part of the dielectric permittivity of the material must be negative. Dielectric permittivity is a measurable physical parameter that is related to the optical properties of the material.[186]

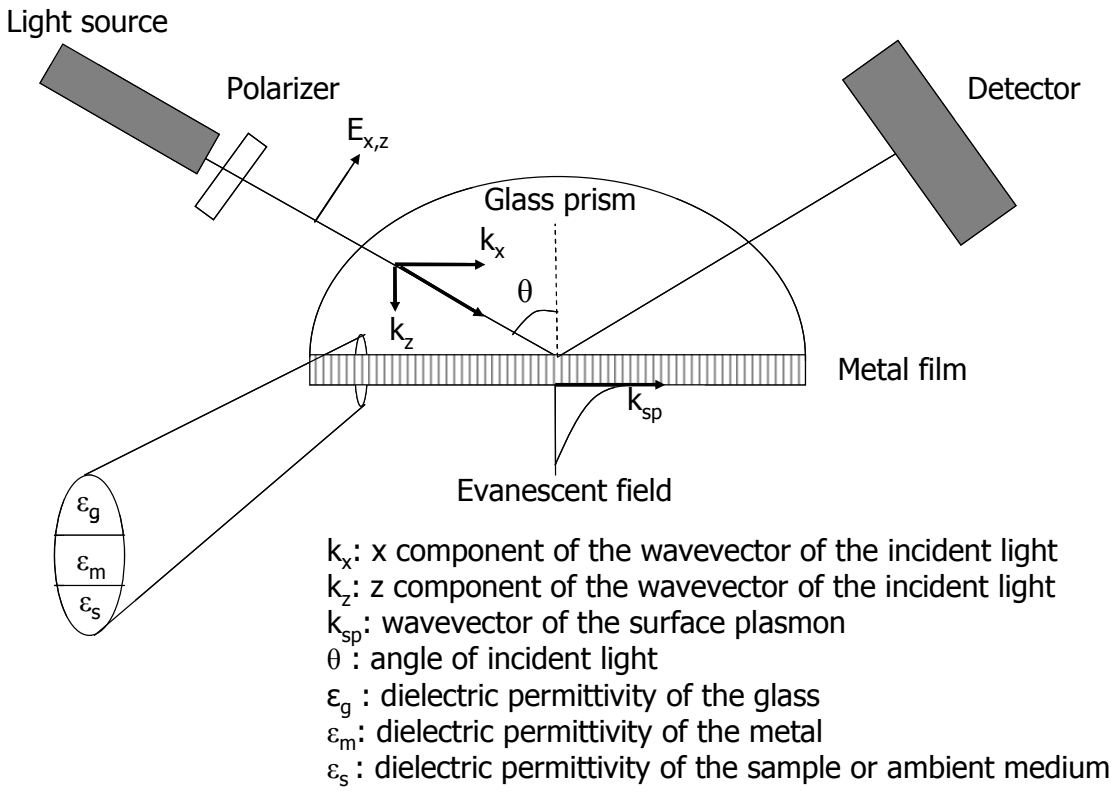

Figure 2.26: Schematic of the Kretschmann prism configuration. Adapted from Liedberg et al.[188]

Although silver exhibits better optical properties for coupling light into the SP mode, it is not always best for SPR sensing applications. Silver is more reactive than gold and care must be taken to ensure that none of the materials to be studied degrade or destroy the material surface. Silver also may not be optimal when functionalization of the SP support metal is planned. Many SAMs with different functionalities can be adsorbed onto gold and silver surfaces. Modification

of surface by such monolayers forms the basis for linking strategies for the immobilization of biomolecules. Gold can accept these modifications quite readily, whereas silver is also amenable to modification but suffers degradation in the process. Therefore, gold is typically used in SPR sensing applications.[189]

As shown in Figure 2.26, the light originates from the source, passes through the polarizer and travels through the glass medium which acts as a waveguide. A waveguide is a physical medium which guides the light in much the same way that a conductor can guide an electrical current. Figure 2.27 illustrates the waveguiding nature of optical waveguides by total internal reflection. When this phenomenon occurs, the light is confined inside the waveguide without significant leakage into the surroundings. For any waveguide, the refractive index of the waveguide medium must be greater than the surroundings. Total internal reflection can occur at a boundary between two media provided that the angle matches or exceeds the critical angle of reflection.[186] Snell's law describes the critical angle of reflection for light incident upon the interface between two media. According to Snell's law,[190]

$$n_1 \sin\theta_1 = n_2 \sin\theta_2 \tag{2.25}$$

where n_1 is the refractive index of medium 1 and n_2 is the refractive index of medium 2. Figure 2.28 illustrates the propagation of the light through the two media, and shows the angles defined in Eqn. 2.25. Total internal reflection occurs when the incident angle (θ_1) is greater than or equal to the critical angle (θ_c).[186] The critical angle is the incident angle where the refracted angle (θ_2) equals 90°. Therefore, the critical angle can be expressed as[190]

$$\theta_c = \sin^{-1}\left(\frac{n_2}{n_1}\right) \tag{2.26}$$

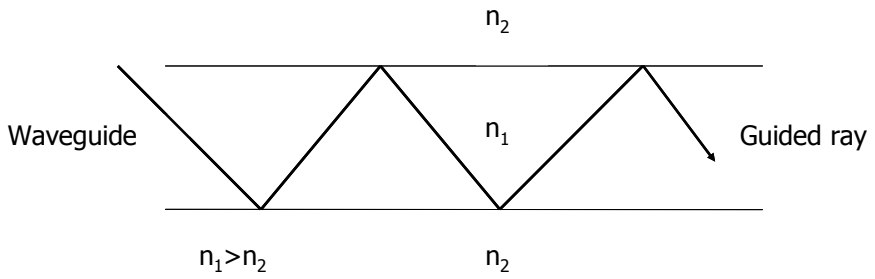

Figure 2.27: Total internal reflection.

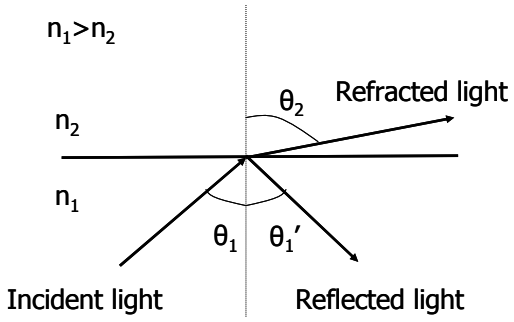

Figure 2.28: Schematic depiction of Snell's Law.

As mentioned before, the Kretschmann prism configuration relies on total internal reflection. Total internal reflection occurs when light traveling through an optically dense medium (e.g. glass) reaches an interface between this medium and a medium of lower optical density (e.g. air) and is reflected to the dense medium. Although the incident light is totally reflected, a component of this light, the evanescent wave or field, penetrates into the less dense medium to a distance on the order of one wavelength. In SPR, a monochromatic, p-polarized light source is used and the interface between two media coated with a thin metal film that has a thickness less than the wavelength of the light.[178] The wavevector of the evanescent field is given by

$$k = \frac{2\pi}{\lambda}\sqrt{\varepsilon_g} \tag{2.27}$$

where λ is the wavelength of the incident light and ε_g is the dielectric permittivity of the glass prism. The component of the wavevector parallel to the surface is defined by

$$k_x = k \bullet \sin\theta \tag{2.28}$$

where θ is the the angle of the incident light. Substitution of Eqn. 2.27 into Eqn. 2.28 yields[186]

$$k_x = \frac{2\pi}{\lambda}\sqrt{\varepsilon_g}\sin\theta \tag{2.29}$$

A surface plasmon is a longitudinal charge density wave that propagates along the interface of a metal and a dielectric.[178] The theoretical understanding of surface plasmons originates from Maxwell's theory, in which free electrons of a metal are treated as a high density electron liquid (plasma). Surface plasmons, then, are the density fluctuations occurring on the surface of such a liquid.[191] The wavevector of a surface plasmon is described by

$$k_{sp} = \frac{2\pi}{\lambda}\sqrt{\frac{\varepsilon_m \varepsilon_s}{\varepsilon_m + \varepsilon_s}} \tag{2.30}$$

where ε_m is the dielectric permittivity of the metal and ε_s is the dielectric permittivity of the sample, or the ambient medium.[186]

The evanescent wave of the incident light will couple with the free oscillating electrons (plasmons) in the metal film at a specific angle of incidence. At this specific angle of incidence, $k_x = k_{sp}$ is satisfied and the surface plasmon is resonantly excited. As a consequence, energy from the incident light is lost to the metal film and the intensity of the reflected light detected by a two-dimensional array of photodiodes or charged coupled detectors (CCD) is reduced.[178] Recalling that, $n=\sqrt{\varepsilon}$ for a non-polar insulator or any material for high frequency electromagnetic radiation such as light, allows Eqn. 2.30 to be expressed in terms of refractive

indices.[192] By varying the angle of the incident light, the condition of $k_x = k_{sp}$ is satisfied at a particular angle:[186]

$$\theta_{sp} = \sin^{-1}\left(\frac{1}{n_g}\sqrt{\frac{n_m^2 n_s^2}{n_m^2 + n_s^2}}\right) \tag{2.31}$$

where n_m and n_s are the refractive index of the metal and sample, respectively. Examination of Eqn. 2.31 shows that θ_{sp} is dependent on the refractive index of the medium above the metal surface up to a thickness of approximately 300 nm above the metal film. This range defines the detection zone for SPR. When the refractive index in this zone above the metal surface changes, either by a change in the refractive index of the solution or through the adsorption of a film on the surface of the sensor, the angle of incidence that excites the surface plasmon changes.[178] Figure 2.29 illustrates the change in the resonant angle, θ_{sp}, associated with the adsorption of an analyte onto the surface.

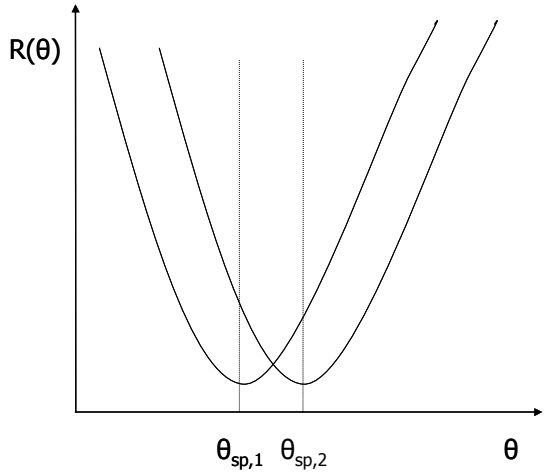

Figure 2.29: Change in the resonant angle due to adsorption. $\theta_{sp,1}$ corresponds to the resonant angle prior to analyte adsorption and $\theta_{sp,2}$ corresponds to the resonant angle after analyte adsorption.

It is possible to calculate the surface concentration (also known as the surface excess) of adsorbed molecule on the sensor surface from the change in refractive index due to adsorption through the relationship of de Feijter et al.:[193]

$$\Gamma = \frac{L \bullet \Delta n_a}{(dn/dc)} \tag{2.32}$$

where L is the thickness of the adsorbed layer, (dn/dc) is the refractive index increment of the adsorbed material with respect to the concentration of the analyte, and Δn_a is the refractive index difference between the adsorbed material and the solvent. The refractive index increment of the adsorbed material can be obtained from a differential refractometer measurements performed at the same wavelength used for SPR measurements. The thickness of the adsorbed material, L, can be calculated by first correcting the observed resonance angle ($\Delta\theta_{sp}$) for changes in the bulk refractive index of the solution:[194]

$$\Delta\theta_a = \Delta\theta_{sp} - c\left(\frac{d\theta_{sp}}{dc}\right) \tag{2.33}$$

where ($d\theta_{sp}/dc$) is the change in the resonant angle with changing bulk analyte concentration (c).[194] Next, the relationship between the change in the resonant angle and the thickness of the film ($dL/d\theta_a$) is obtained from Fresnel simulations.[195, 196] This quantity along with the result of Eqn. 2.33 can be used to deduce the thickness of the film:[194, 195, 197]

$$L = \Delta\theta_a\left(\frac{dL}{d\theta_a}\right) \tag{2.34}$$

By substituting Eqn. 2.34 into Eqn. 2.32, the surface excess becomes

$$\Gamma = \frac{\Delta\theta_a \bullet \Delta n_a}{(d\theta_a/dL) \bullet (dn/dc)} \tag{2.35}$$

CHAPTER 3

Materials and Experimental Techniques

3.1 Materials

Ultrapure water (Millipore, Milli-Q Gradient A-10, 18.2 MΩ·cm, < 5 ppb organic impurities) was used in all aqueous systems. Trimethylsilyl cellulose (DS = 2.71) was synthesized and kindly provided by Prof. Thomas Heinze's group at the Friedrich-Schiller-University in Jena, Germany. 11-mercapto-1-undecanol (SAM-OH), 1-dodecanethiol (SAM-CH_3), 11-mercapto-undecanoic acid (SAM-COOH), and methyl trans-cinnamate, 99% (Me-Cinn) were purchased from Aldrich. Dimethyl sulfoxide, spectrophotometric grade, 99.9+% (DMSO), pyridine, 99+% (Py), cinnamic acid, 98+% (CA) and N, N'-carbonyl diimidazole, 98% (CDI) were purchased from Alfa Aesar. Pullulan, from Aurebasidium pullulans and N, N-dimethylacetamide, 99% (DMAc) were purchased from Sigma. NaCl (>= 99%, ACS reagent) was purchased from Sigma-Aldrich. N, N-Dimethyl formamide, 99.9% (DMF) was purchased from Fischer Scientific and distilled under reduced pressure with anhydrous magnesium sulfate as a drying agent. Absolute ethanol was purchased from Decon Lab, Inc. Dry formamide was purchased from Riedel-de Haën. Acetic anhydride, ≥ 99% was purchased from Fluka. All other reagents, H_2O_2 (30% by volume), H_2SO_4 (conc.), and NH_4OH (28% by volume) were purchased from EM Science, VWR International, and Fisher Scientific, respectively.

3.1.1 Synthesis and Characterization of Pullulan Cinnamates (PC)

Pullulan cinnamates were synthesized by the reaction of pullulan with cinnamic acid in the presence of CDI as a coupling agent (Figure 3.1). The carbonyl group in cinnamic acid was activated by CDI. CDI and cinnamic acid were dissolved in 10 mL anhydrous DMF. The mixture was stirred for 24 hours at room temperature. 1.0 g of pullulan (6 mmol of glucose) was dissolved in 20 mL DMAc at 70 ˚C and magnetically stirred for ~1 h. The activated cinnamic

acid was added to the reaction flask. The mixture was stirred for 24 hours at 70 °C. The product was precipitated in absolute ethanol and dried under vacuum at 40 °C for 24 hours. The DS of pullulan cinnamate derivatives were determined by ^{1}H NMR and UV-Vis measurements. DS was defined as the number of cinnamate groups per AGU throughout this thesis. DS of PC samples and their weight average molar masses (M_w) and polydispersity indices (M_w/M_n) obtained by aqueous size exclusion chromatography (SEC, Waters size exclusion chromatograph) were summarized in Table 3.1. The mobile phase, 0.7 M $NaNO_3$, 0.1 M Tris, and 200 ppm NaN_3 at pH = 6, was equilibrated at 30 °C with a flow rate of 0.8 mL•min^{-1}. The SEC instrument was equipped with 2× Waters Ultrahydrogel linear columns and 1× Waters Ultrahydrogel 250 column (all columns measuring 7.8 × 300 mm), a Waters 1515 isocratic HPLC pump, Waters 717plus autosampler, a Wyatt miniDAWN multiangle laser light scattering (MALLS) detector with a He-Ne laser operated at 690 nm, a Viscotek 270 viscosity detector, and a Waters 2414 differential refractive index detector operated at 880 nm and 35 °C. Reported weight average molar masses (M_w) and polydispersity indices (M_w/M_n) were based upon absolute measurements from the MALLS detector.

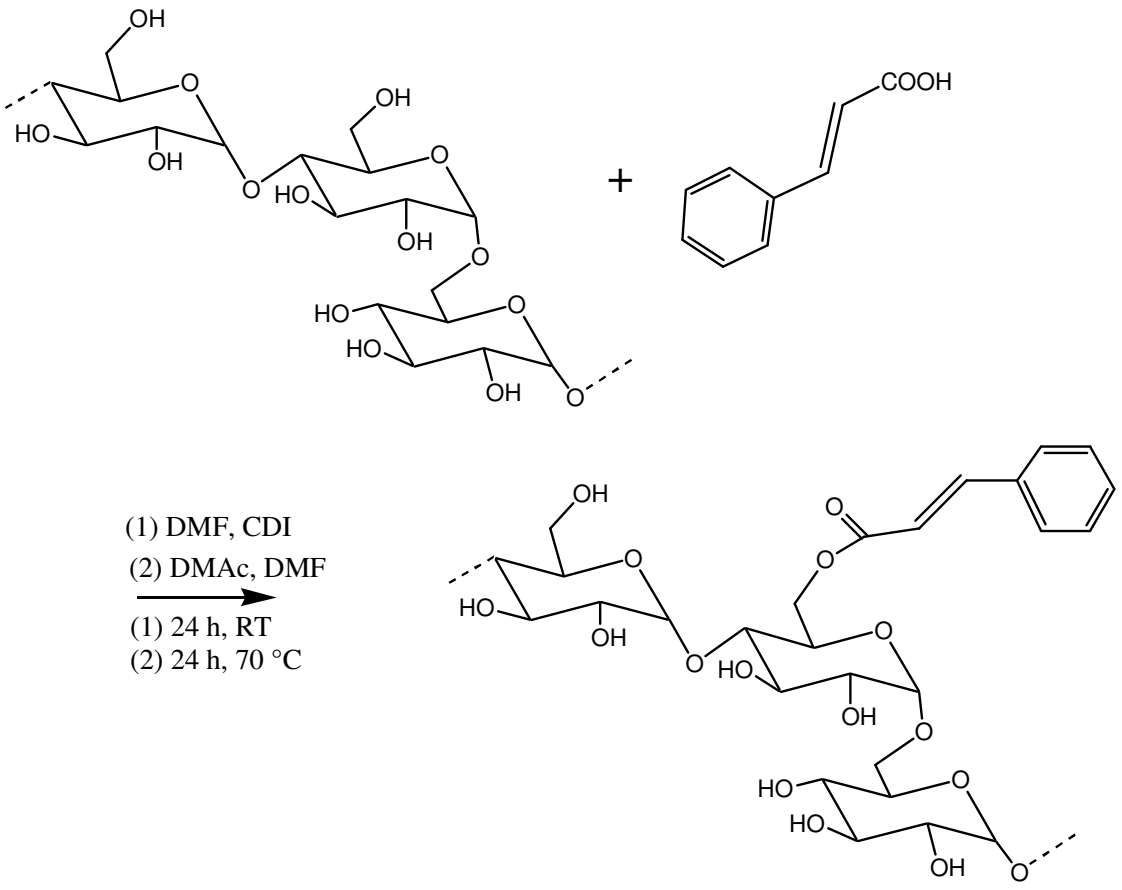

Figure 3.1: Reaction scheme for the synthesized pullulan cinnamates.

Table 3.1: Pullulan and pullulan cinnamate samples used for SPR experiments.

	DS[a]	DS[b]	M_w[c] (kg•mol^{-1})	M_w/M_n[c]	(dn/dc)[d] (mL•g^{-1})
P	0	0	112	1.38	0.146 ± 0.002
PC003	0.033	0.036	111	1.35	0.145 ± 0.001
PC006	0.057	0.058	118	1.30	0.147 ± 0.001
PC008	0.078	0.080	100	1.10	0.145 ± 0.001

a. Degree of substitution determined by ^{1}H NMR.
b. Degree of substitution determined by UV spectroscopy.
c. SEC in 0.7 M $NaNO_3$, 0.1 M Tris, and 200 ppm NaN_3, at pH = 6.
d. Measured with a differential refractometer in water at λ = 690 nm at 20 ºC.

3.1.1.1 ^{1}H NMR Characterization of Pullulan Cinnamates

^{1}H NMR spectra were obtained on a 500 MHz JEOL Eclipse spectrometer. Unmodified pullulan consisted of linear chains of anhydroglucose units that alternated regularly between one α-(1→6) linkage and two α-(1→4) linkages, or stated another way, maltotriosyl repeating units (MTU) connected by α-(1→6) linkages.[198] ^{1}H NMR spectra for pullulan cinnamates in D_2O were provided in Figure 3.2. Peaks between chemical shifts of δ = 3.3 and δ = 4.2 ppm corresponded to protons of the AGUs. The integrated area around δ = 4.98 ppm originated from anomeric protons of α-(1→6) linkages between MTUs, whereas the integrated area around δ = 5.38 and δ = 5.41 ppm originated from anomeric protons of α-(1→4) linkages of the MTUs. The ratio of α-(1→4) linkages to α-(1→6) linkages was 2 which was consistent with the previously reported value.[199] The integrated area between δ = 6.4 and δ = 8.0 ppm corresponded to the seven protons of the cinnamate groups. If each AGU unit was substituted with a single cinnamate group, DS would be equal to 1 and the integrated area between δ = 6.4 and δ = 8.0 ppm would be equal 21. Therefore, division of the integrated area between δ = 6.4 and δ = 8.0 ppm by 21 gave the DS of the pullulan cinnamate. Hence, the DS was defined as the number of cinnamate groups per anhydroglucose unit. DS values deduced from the ^{1}H NMR spectra in Figure 3.2 were summarized in Table 3.1.

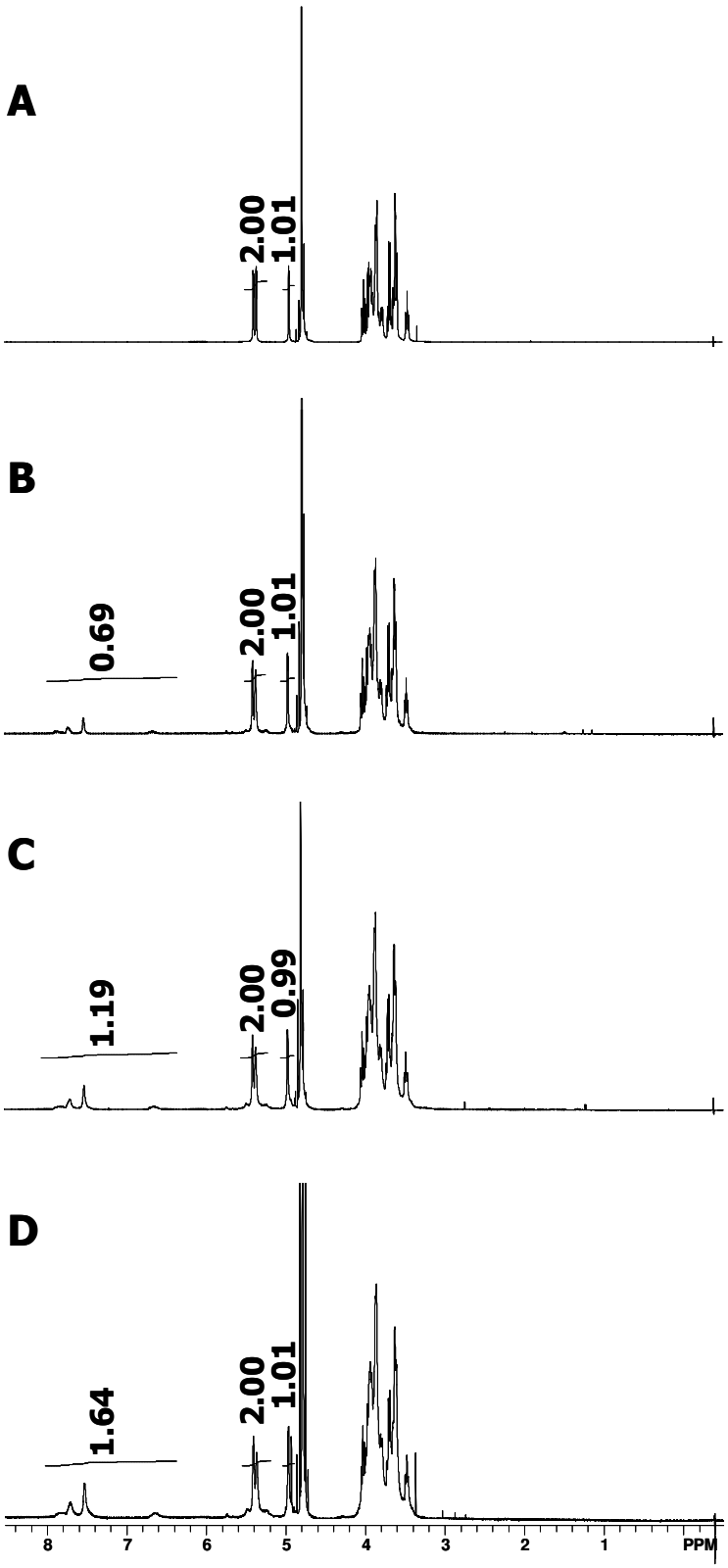

Figure 3.2: ^{1}H NMR spectra of (A) pullulan (P), (B) PC003, (C) PC006, and (D) PC008 in D_2O.

3.1.1.2 UV Spectroscopic Characterization of Pullulan Cinnamates

UV spectra for methyl trans-cinnamate at different concentrations and a spectrum for pullulan cinnamate at a single concentration in DMSO were provided in Figure 3.3. As seen in Figure 3.3, all spectra showed an absorbance maximum at a wavelength of λ_{max} = 281 nm. A methyl cinnamate calibration curve was used for the DS determination for pullulan cinnamates because all spectra had the same shape and λ_{max}.

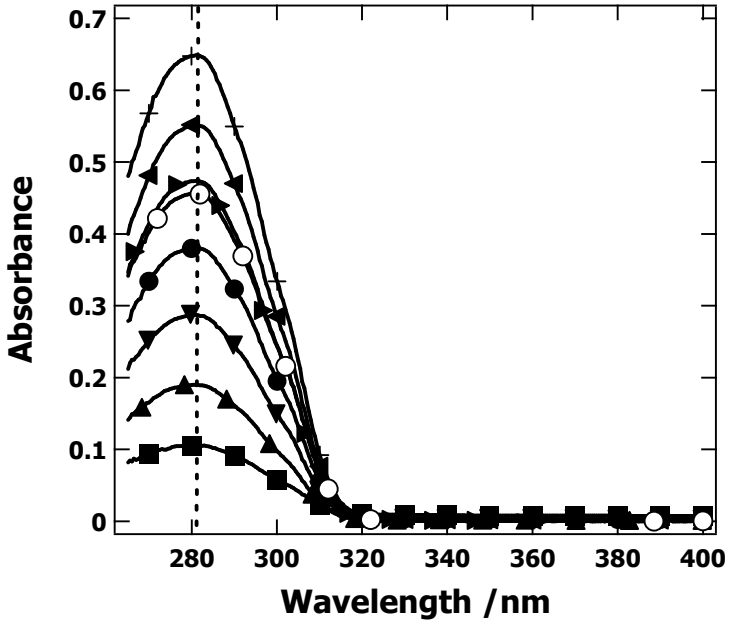

Figure 3.3: UV spectra of PC008 and methyl trans-cinnamate in DMSO. Symbols corresponded to (○) 50.7 mg·L^{-1} PC008 in DMSO, and (■) 4.76 μM, (▲) 9.52 μM, (▼) 14.3 μM, (●) 19.0 μM, (►) 23.8 μM, (◄) 28.6 μM, and (+) 33.3 μM methyl trans-cinnamate solutions in DMSO.

A calibration curve for methyl *trans*-cinnamate at λ_{max} = 281 nm in DMSO (Figure 3.4) had a slope of (19.02 ± 0.22) × 10^3 M^{-1}·cm^{-1} and a y-intercept of 0.015 ± 0.005. As such, the curve in Figure 3.4 was consistent with Beer's Law, A = ε·b·c where A was absorbance, ε was the molar extinction coefficient, b was the path length, and c was the molar concentration. Hence, a value

of $\varepsilon_{max,281\ nm}$ = (19.02 ± 0.22) × 10^3 $M^{-1}{\cdot}cm^{-1}$ was obtained. The observed values of $\varepsilon_{max,281\ nm}$ and λ_{max} for methyl *trans*-cinnamate differed somewhat from octyl-*p*-methoxy-*trans*-cinnamate in hexane (ε_{max} = 24×10^3 $M^{-1}{\cdot}cm^{-1}$ and λ_{max} =310 nm).[200] Compared to methyl *trans*-cinnamate, methoxy (-OCH_3) substitution of the benzene ring caused a bathochromic shift (the absorption maximum moved to higher wavelength) and increased absorbance.

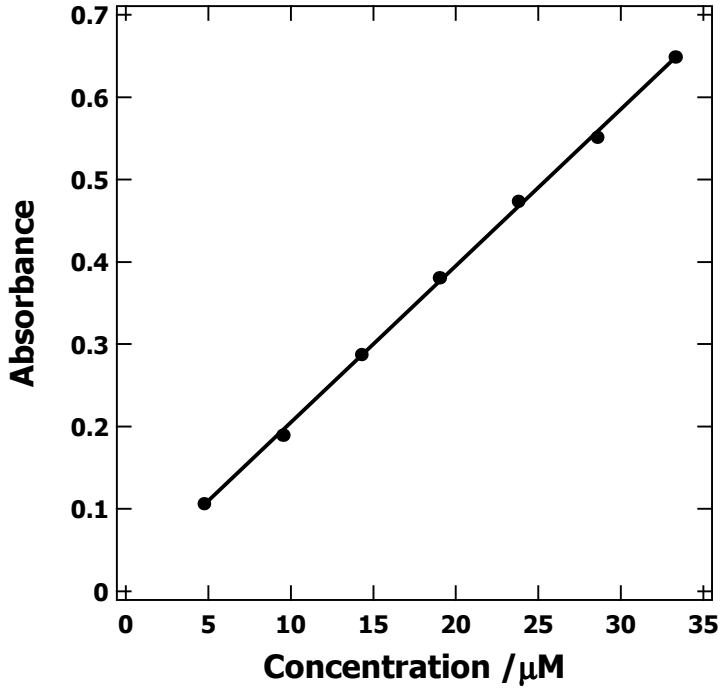

Figure 3.4: UV-Vis absorbance calibration curve for methyl trans-cinnamate in DMSO at λ_{max} = 281 nm. The molar extinction coefficient was $\varepsilon_{max,\ 281nm}$ = (19.02 ± 0.22) × 10^3 $M^{-1}{\cdot}cm^{-1}$ for methyl trans-cinnamate.

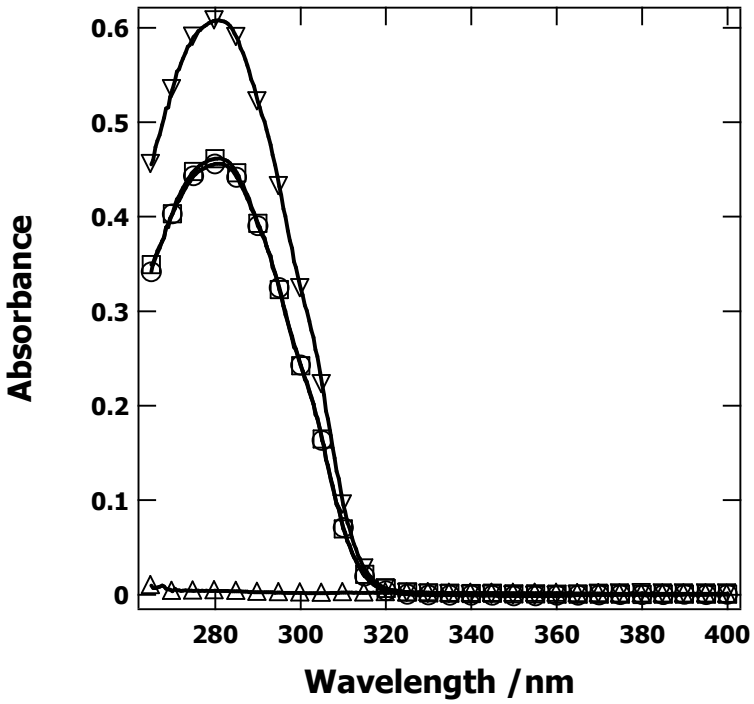

Figure 3.5: UV spectra of pullulan and pullulan cinnamates in DMSO. Symbols corresponded to (Δ) 100 mg·L^{-1} P, (□) 106.7 mg·L^{-1} PC003, (∇) 88 mg·L^{-1} PC006, and (○) 50.7 mg·L^{-1} PC008 in DMSO.

UV spectra for pullulan and pullulan cinnamates were shown in Figure 3.5. The absorbances of PC003 (106.7 mg·L^{-1}), PC006 (88.0 mg·L^{-1}), and PC008 (50.7 mg·L^{-1}) in DMSO at λ_{max} = 281 nm were 0.462, 0.608, and 0.456, respectively. The absence of strong absorbance for pullulan at a concentration of 100 mg·L^{-1} indicated the absence of strong chromophores in the molecule. However, weak UV absorbance was observed for pullulan at higher concentrations (Figure 3.6). Due to weak UV absorbance by pullulan at λ = 281 nm, an UV absorbance calibration curve was also established for pullulan in Figure 3.7. As seen in Figure 3.7, a calibration curve for pullulan at λ = 281 nm in DMSO yielded a slope of 23 ± 2 M^{-1}·cm^{-1} with a y-intercept of -0.0078 ± 0.0089. As such, the curve in Figure 3.7 was also consistent with Beer's Law. Hence, $\varepsilon_{281\ nm}$ was

equal to 23 ± 2 $M^{-1}\cdot cm^{-1}$. The weak UV absorbance along the pullulan chain was likely caused by the carbonyl groups (C=O) at the reducing end of the linear chain. Linear polysaccharides have generally been characterized by one reducing end (the residue containing the free anomeric carbon) and one non-reducing end, where reducing ends have been hemiacetals in equilibrium with their open-chain forms (characterized by a carbonyl group). The internal residues were all acetals that were not in equilibrium with their open-chain forms and thus did not contain carbonyl groups.[201] λ_{max} = 279.5 nm and $\varepsilon_{max,279.5\ nm}$ = 23 ± 2 $M^{-1}\cdot cm^{-1}$ values agreed with reported values for the UV absorbance of the carbonyl group (270 nm < λ_{max} < 285 nm and 18 $M^{-1}\cdot cm^{-1}$ < ε_{max} < 30 $M^{-1}\cdot cm^{-1}$).[202]

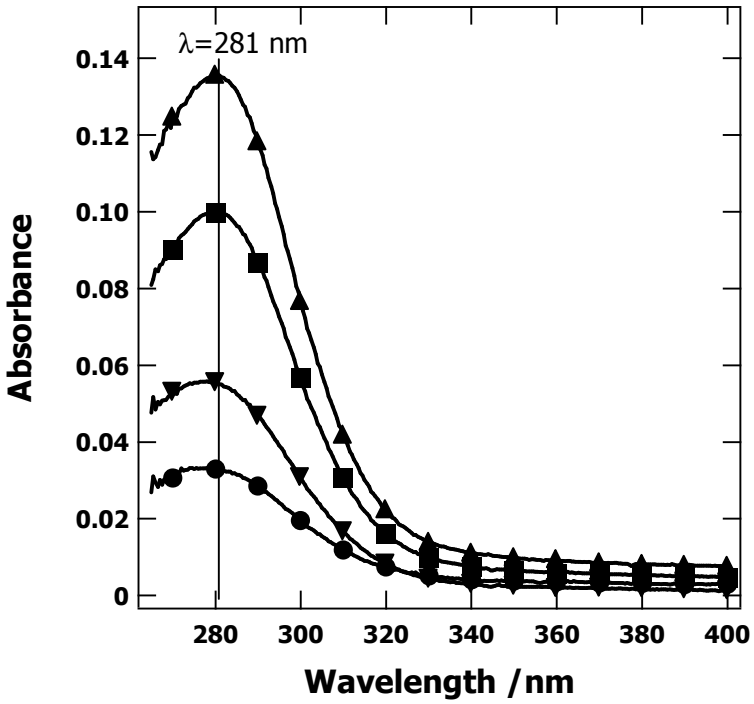

Figure 3.6: UV spectra of pullulan in DMSO. Symbols corresponded to pullulan with AGU concentrations of (●) 1.54 mM, (▼) 3.08 mM, (■) 4.57 mM, and (▲) 6.12 mM in DMSO.

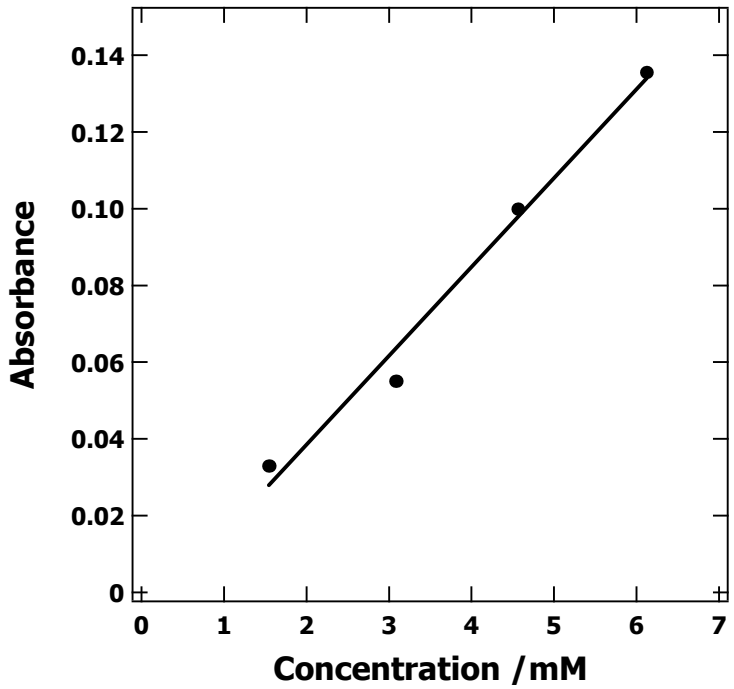

Figure 3.7: UV absorbance calibration curve for pullulan in DMSO at λ = 281 nm. The molar extinction coefficient for pullulan was $\varepsilon_{281nm} = 23 \pm 2\ M^{-1} \cdot cm^{-1}$.

DS for pullulan cinnamate was formulated as

$$DS = C_{Cinn} / C_{AGU} \tag{3.1}$$

where C_{Cinn} was the molar concentration of cinnamate groups and C_{AGU} was the molar concentration of anhydroglucose units (AGU). DS for pullulan cinnamate was calculated from Eqns. 3.2 and 3.3:

$$m = (C_{Cinn} \times V \times MW_{Cinn}) + (C_{AGU} \times V \times MW_{AGU}) \tag{3.2}$$

$$A = (\varepsilon_{Cinn} \times b \times C_{Cinn}) + (\varepsilon_{AGU} \times b \times C_{AGU}) \tag{3.3}$$

where m was the mass of the pullulan cinnamate, MW_{Cinn} was the molecular weight of a cinnamate group, MW_{AGU} was the molecular weight of an anhydroglucose unit, V was the volume of the polymer solution, and ε_{Cinn} and ε_{AGU} were the molar extinction coefficients for

cinnamate and AGU units, respectively. Simultaneous solution of Eqns. 3.2 and 3.3 yielded C_{Cinn} and C_{AGU}. Results for the pullulan cinnamates used in this thesis were summarized in Table 3.1.

3.1.2 Characterization of 2-Hydroxypropyltrimethylammonium Xylans (HPMAXs)

HPMAXs were provided by Prof. Thomas Heinze's group at the Friedrich-Schiller-University in Jena, Germany. HPMAXs were synthesized by the reaction of birch xylan (BX) with 2,3-epoxypropytrimethylammonium chloride (EPTA) (Figure 3.8). The BX contained 0.1 4-*O*-methylglucuronic acid (MeGA) groups per anhydroxylose unit (AXU). Details of the HPMAX synthesis were described elsewhere.[203] DS was defined as the number of 2-hydroxypropyltrimethylammonium (HPMA) groups per AXU. The DS of HPMAX samples and their refractive index increments in water at different salt concentrations (1 mM, 10 mM, and 100 mM NaCl in water) were summarized in Table 3.2.

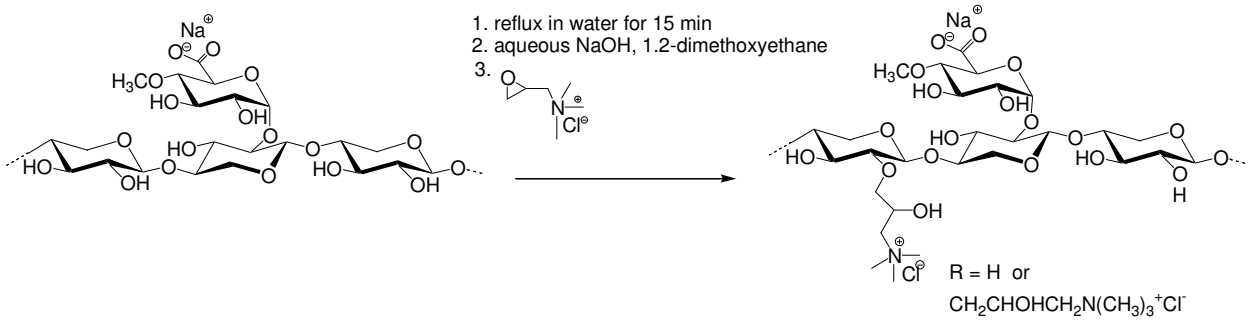

Figure 3.8: Reaction scheme for the cationization of GX with EPTA to yield HPMAX. MeGA DS was ~0.1/AXU.

Table 3.2: Refractive index increments of HPMAXs used in SPR experiments.

Acronym	Degree of Substitution (DS)[a]	(dn/dc)[b] (mL•g^{-1})			
		Water	1 mM NaCl	10 mM NaCl	100 mM NaCl
HPMAX006	0.06	0.105 ± 0.002	—	—	—
HPMAX010	0.10	0.130 ± 0.002	0.131 ± 0.002	0.135 ± 0.002	0.147 ± 0.003
HPMAX014	0.14	0.146 ± 0.002	—	—	—
HPMAX019	0.19	0.149 ± 0.002	—	—	—
HPMAX034	0.34	0.146 ± 0.002	0.145 ± 0.002	0.138 ± 0.002	0.137 ± 0.003

a. HPMA DS determined by elemental analysis, all samples have a MeGA DS = 0.1.
b. Measured with a differential refractometer in the corresponding medium at λ = 690 nm at 20 ºC.

3.1.3 Characterization of Hydroxypropyl Xylans (HPXs)

HPX samples were provided by Prof. Wolfgang Glasser's group at Virginia Tech. They were synthesized by the reaction of barley husk xylan with propylene oxide (PO) in aqueous alkali conditions (Figure 3.9a). Details of the HPX synthesis were provided elsewhere.[204] In this study, HPX derivatives were named according to the pH of the aqueous solution used for the hydroxypropylation of xylan. HPX120, HPX125, HPX127, and HPX130 corresponded to pH = 12.0, 12.5, 12.7, and 13.0, respectively. In general, the DS increased with pH.[204] For DS determinations, HPX was acetylated with acetic anhydride in accordance with the method of Carson and Maclay with minor modification (Figure 3.9b).[205] HPX (0.5 g) was dissolved in 10 mL of dry formamide at 45 to 50 ºC and was vigorously stirred for 30 minutes. Next, 5 mL of pyridine was added at 45 to 50 ºC and the mixture was stirred for 30 minutes. Afterwards, the reaction mixture was cooled to 30 ºC, and 5 mL of acetic anhydride was added. Following overnight stirring, the reaction mixture was precipitated in 200 mL of a cold aqueous 2 wt% HCl solution. Finally, the precipitated solids were filtered and rinsed with copious amounts of cold aqueous 0.5 wt% HCl solution and cold ultrapure water. The resulting product was dried overnight at 35 ºC under vacuum. For ^{1}H NMR analysis, 3 to 5 mg of acetylated HPXs were

dissolved in 5 mL of $CDCl_3$. ^1H NMR spectra were obtained on a 400 MHz Varian Inova spectrometer.

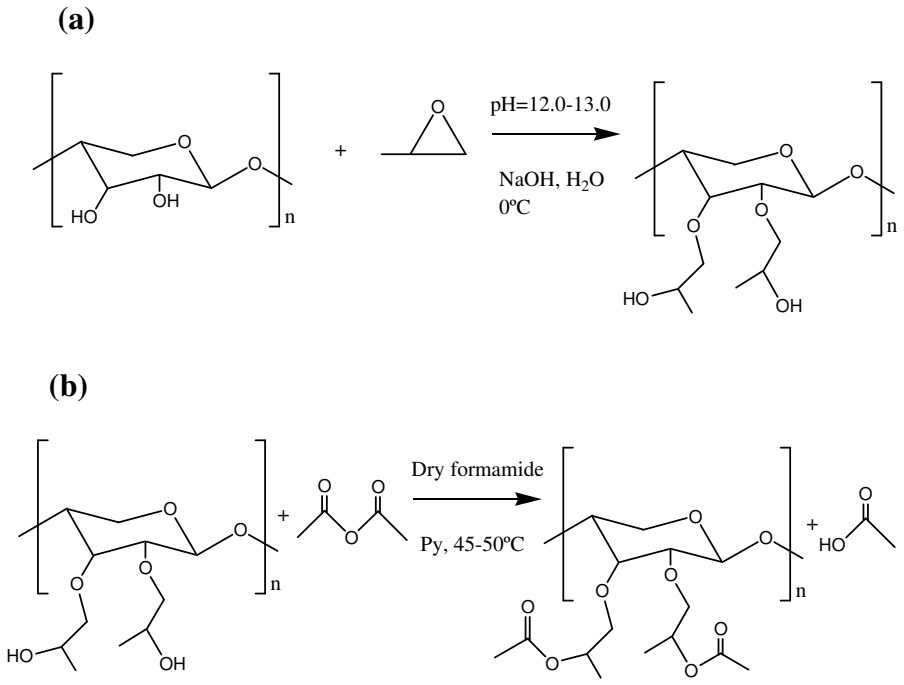

Figure 3.9: Reaction schemes for the synthesis of (a) hydroxypropyl xylan (HPX) and (b) acetoxypropyl xylan (APX).

3.2 Characterization Techniques and Film Preparation

3.2.1 Preparation of Model Cellulose Films

Smooth, uniform films of regenerated cellulose were prepared on 12.4 mm x 12.4 mm x 0.9 mm sensor slides from trimethylsilylcellulose (TMSC). Sensor slides consisted of a glass slide covered with 20 Å of chromium and 480 Å of gold. Sensor slides were obtained by initial deposition of the chromium layer and then the gold layer onto precleaned soda lime float glass (Specialty Glass Products, Inc.) at 3×10^{-6} Torr with an electron beam evaporator system (Thermionic Vacuum Products). Spincoating was used to prepare TMSC surfaces. Each sensor slide was cleaned by immersion in a 7:3 by volume solution of sulfuric acid:hydrogen peroxide (piranha solution) for 1 h and rinsed exhaustively with Millipore water prior to spincoating.

TMSC was spincoated onto cleaned sensor slides with a spinning speed of 4000 rpm from 10 $g \cdot L^{-1}$ TMSC solutions in toluene.[142] TMSC coated sensor slides were hydrophobic, and had a water contact angle of 91 ± 1°. Trimethylsilyl groups of TMSC were cleaved by exposure of the gold slide to the vapor of an aqueous 10 wt% HCl solution for 2 minutes. This process yielded a regenerated cellulose surface.[136] The regenerated cellulose surface was hydrophilic and had a water contact angle of 29 ± 2°. The extent of the desilylation reaction was followed by X-ray photoelectron spectroscopy (XPS).

3.2.2 Preparation of Self-Assembled Monolayers (SAMs)

The sensor slides underwent the same cleaning procedure described for the preparation of model cellulose films. Once dried, the sensor slides were placed in a 1 mM solution of the appropriate SAM forming molecule [(1-mercapto-1-undecanol (SAM-OH), or 1-dodecanethiol (SAM-CH_3), or 11-mercapto-undecanoic acid (SAM-COOH)] in absolute ethanol for at least 24 hours.[158] Once the SAM sensor was needed, the slide was removed from the 1 mM ethanolic solution, rinsed with absolute ethanol for the removal of excess SAM forming molecules, and dried with nitrogen. Finally, the SAM sensor slide was washed with ultrapure water and dried with nitrogen. The SAM sensor slides were either hydrophilic or hydrophobic, a function of the SAM forming molecule used. Surfaces prepared from SAM-OH had a water contact angle of 20 ± 2°, whereas surfaces prepared from 1-dodecanethiol had a water contact angle of 100 ± 1°.

3.2.3 X-ray Photoelectron Spectroscopy (XPS)

XPS (PHI 5400, Perkin-Elmer, Mg-Kα radiation) was performed with a magnesium anode operated at 250 W with a background pressure of 5×10^{-7} Torr. The spectra were recorded with an 89.45 eV pass energy, 0.1 eV step and 25 ms dwelling time. The angle between the X-

ray beam and surface normal was 15°. Each surface was examined with both a survey scan, that encompassed the region 0 to 1100 eV, and a multiplex of carbon, oxygen, silicon, and gold.

Relative elemental compositions for spincoated cellulose surfaces before and after desilylation were provided in Table 3.3. The absence of the Si 2p peaks after desilylation with wet HCl vapor confirmed that trimethylsilyl groups were removed. The experimental elemental composition for TMSC was in reasonable agreement with the theoretical elemental composition calculated on the basis of a DS = 2.71. Likewise, the experimental C:O ratio for the regenerated cellulose also exhibited reasonable agreement with the experimental value.

Table 3.3: Elemental compositions of spin-coated TMSC surfaces before and after desilylation.

		Au 4f[a]	C 1s[a]	O 1s[a]	Si 2p[a]
TMSC	Expt.[b]	0	65.4	22.6	12.0
Surface	Theo.[c]	0	62.8	25.7	11.5
After	Expt.[b]	0.1	59.7	40.2	0
Desilylation	Theo.[c]	0	54.6	45.4	0

a. Atomic percentages.
b. Experimental results from XPS measurements.
c. Theoretical percentages on the basis of the molecular structure.

3.2.4 Characterization of Regenerated Cellulose by Reflection Absorption Infrared Spectroscopy (RAIRS) and Electron Diffraction

3.2.4.1 Reflection Absorption Infrared Spectroscopy (RAIRS)

Regenerated cellulose films on gold substrates were prepared as described previously. RAIRS spectra were collected in a fashion similar to the approach used for for poly(L-lactic acid) films.[206] RAIRS was performed with a Bruker Vertex 80v FTIR spectrometer, equipped with a liquid nitrogen cooled mercury cadmium telluride (MCT) detector. The measurements were executed at an angle of incidence of ~86° with p-polarized light. 200 scans at a resolution of 2 cm^{-1} were averaged, and clean gold substrates were used as background references.

3.2.4.2 Electron Diffraction

Regenerated cellulose samples were prepared on carbon-coated TEM grids in a process analogous to the process used for TMSC films as described previously. TMSC was first deposited onto the TEM grid from an 1 $g \cdot L^{-1}$ TMSC solution in toluene. Cellulose was regenerated by exposure of the grid to the vapor of an aqueous 10 wt% HCl solution for 2 minutes. After the films were dried with nitrogen was complete, the sample was studied using a Philips EM 420 electron microscope operated at 120 kV.

Regenerated cellulose hydrolyzed from TMSC has been found largely in the amorphous state. Conversely, native cellulose is normally composed of both amorphous and crystalline cellulose I (parallel chains) regions.[207] Electron diffraction and reflection absorption infrared spectroscopy (RAIRS) experiments[206] confirmed that the regeneration process used in this study yielded amorphous bulk and film samples, respectively. In the RAIRS spectrum of a regenerated cellulose film, the absorption band at about 1430 cm^{-1}, assigned to the CH_2 scissoring motion, was very weak in regenerated cellulose samples and indicated that breakage of the intramolecular hydrogen bond associated with O6 in the glucose unit had occurred. In addition, the band at about 895 cm^{-1}, assigned as C–O–C stretching at the β-(1-4)-glycosidic linkage, was intense due to the amorphous character of the sample. The O-H stretching band of the hydroxyl groups on regenerated cellulose surfaces was shifted to 3421 cm^{-1} and was slightly broadened as a result of regeneration. This observation confirmed weaker intra- and intermolecular hydrogen bonding, i.e., lower crystallinity. Furthermore, the model regenerated cellulose surfaces exhibited no features characteristic of crystalline cellulose II (anti-parallel chains) structures. All of these observations were in line with a previous study.[142] Likewise, electron diffraction of regenerated cellulose yielded no crystalline reflections, while the circular halo of the diffraction pattern

indicated the regenerated cellulose samples were unoriented and amorphous. Hence, conclusions drawn in this study should be consistent with adsorption onto the amorphous regions of the native cellulose I structure.

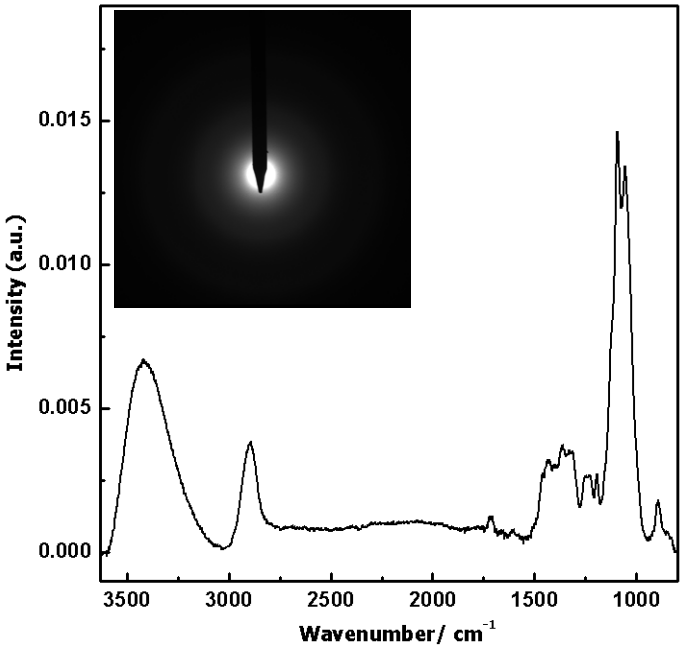

Figure 3.10: A RAIRS spectrum of a regenerated cellulose film. The inset shows an electron diffraction pattern for regenerated cellulose.

3.2.5 Surface Tension Measurements

The surface tension measurements of aqueous polymer solutions were determined by the Wilhemy plate method using a paper plate attached to a Cahn 2000 electrobalance. In general, polymer solutions were placed in a specially designed glass jar that consisted of an inner cup containing the solution and an outer jacket that contained 20.0 ºC flowed water from a thermostated circulating bath. The sample cell was inside a Plexiglass™ box for the minimization of water evaporation and the maintainence of a constant relative humidity (~ 75%). For surface tension measurements of aqueous P and PC solutions, a fixed volume of 10 mL of 1 $g \cdot L^{-1}$ polymer solution was placed in the specially designed jar. Surface tension values were

recorded for a period of 10 hours at fixed time intervals. For surface tension measurements of aqueous HPX solutions, a fixed volume of 20 mL of water was placed in the specially designed glass jar. Next, HPX stock solution (~ 150 $mg \cdot L^{-1}$) was added to the pure water incrementally with a digital variable volume pipettor that controlled the HPX solution concentration.

3.2.6 Pyrene Dye Fluorescence Measurements

The aggregation of pullulan derivatives was investigated by fluorescence spectroscopy (Perkin-Elmer LS 50 Spectrometer) with a fluorescent pyrene probe.[208] Aliquots of pyrene in methanol were initially transferred into empty vials until the methanol evaporated. Next, test solutions of known concentration were added to the vials. All of the mixtures were shaken mildly on an Orbit Shaker for at least 24 h. Next, test solutions of known concentration were added to the vials. All of the mixtures were shaken mildly on an Orbit Shaker for at least 24 hours. The resulting solutions contained 10^{-6} M pyrene. Emission fluorescence spectra of pyrene were recorded with an excitation wavelength of 334 nm, an excitation bandpass of 5 nm, and an emission bandpass of 2.5 nm. The ratios of the emission intensities of the first (I_1 = 373 nm) and third (I_3 = 384 nm) vibronic peaks in the emission spectra were sensitive to the polarity of the pyrene microenvironment.

3.2.7 Contact Angle Measurements

Static contact angle measurements were made with a FTA125 Contact Angle Analyzer (First Ten Angstroms). All data were collected at room temperature. The surfaces were kept inside an environmental chamber that minimized evaporation of the sessile drop with time and maintained a constant relative humidity (~ 75%). The static contact angles of drops of ultrapure water on a given surface were measured. A minimum of three different samples for each surface were recorded and averaged with one standard deviation error bars.

3.2.8 Refractive Index Increment Measurements

The refractive index increments (dn/dc) of polymer solutions were determined with a Wyatt Optilab rEX differential refractometer. The experiments were carried out at λ = 690 nm at 20 ºC. Samples were flowed at 0.25 $mL \cdot min^{-1}$ into the differential refractometer using a syringe pump and a syringe affixed with a 0.80 μm cellulose acetate (CA) syringe filter. The (dn/dc) values were determined using the Wyatt Astra V software package. For aqueous P and PC solutions, dn/dc values were evaluated over the concentration range of 0 to 2.5 $g \cdot L^{-1}$, whereas for aqueous HPMAX, and HPX solutions, dn/dc values were evaluated over the concentration range of 0 to 150 $mg \cdot L^{-1}$. For polymer solutions at higher salt concentration (100 mM NaCl), the refractive index increments were measured at a constant chemical potential for the counterions in the solution and the environment of the polymer coil through the two-step procedure of Hunkeler et al.[209] First, 150 $mg \cdot L^{-1}$ of HPMAX010 or HPMAX034 stock solutions were prepared in 100 mM NaCl and these stock solutions were dialyzed with SpectraPor 6 membranes (MWCO 8kD) against 100 mM NaCl for 24 hours. Second, the stock solutions were diluted with dialysate and refractive index increments were determined for the HPMAX solutions against the dialysates with the differential refractometer.

3.2.9 In Situ AFM Measurements

Template stripped gold surfaces were prepared for AFM imaging.[210] Gold films, 100 nm thick were first evaporated onto freshly cleaved mica surfaces at a rate of 1 $Å \cdot s^{-1}$ at 3×10^{-6} Torr with an electron beam evaporator system (Thermionic Vacuum Products). Silicon wafers were glued to the gold-deposited mica sheets by Epo-tek 377. The epoxy glue was cured at 150° C for two hours. Prior to use, the multilayer was soaked in THF until the gold surface detached from the mica substrate. Regenerated cellulose and SAM surfaces were prepared as described above.

A Nanoscope III atomic force microscope (Dimension 3000 scope with a Nanoscope IIIa controller, Digital Instruments) imaged the samples in tapping mode. The probes, standard silicon nitride tips, had a nominal radius of 20 nm and a spring constant of 0.12 $N \bullet m^{-1}$. Cantilevers were exposed to ultraviolet irradiation for at least 30 minutes for the removal of organic contaminants. After the fluid cell was installed, ultrapure water was flowed over the surface. Images of the reference surface were taken after an equilibration flow time of 1 hour. Next, 1 $g \bullet L^{-1}$ polysaccharide solution was injected into the liquid cell for at least 2 hours. Prior to collection of the post-adsorption images, a large excess of ultrapure water was flowed over the surface for 1 hour.

3.2.10 Surface Plasmon Resonance (SPR) Spectroscopy

Polymer adsorption onto regenerated cellulose and SAM surfaces was investigated by SPR spectroscopy. After preparing the desired film (cellulose or SAM) was prepared on the sensor slide, the slide was refractive index-matched to the prism of a Reichert SR 7000 SPR refractometer using immersion oil ($n_D = 1.5150$). This system used a laser diode with an emission wavelength of 780 nm. The flow cell body was equipped with a Viton gasket (Dupont Dow Elastomers, LLC) and was mounted on top of the sensor slide. Solutions were pumped into the flow cell at a flow rate of 0.25 $mL \cdot min^{-1}$ via Teflon tubing connected to a cartridge pump (Masterflex) at 20.0°C. The pump was linked to a switch valve that allowed the polymer solutions and ultrapure water to be switched without the introduction of air bubbles into the system. For SPR experiments, polymer stock solutions were prepared by dissolution of the polymer in Millipore water to ~ 1 $g \cdot L^{-1}$ for P and PCs and ~ 150 $mg \cdot L^{-1}$ for HPXs and HPMAXs. It should be mentioned that BX did not completely dissolve in ultrapure water and formed a suspension which was clearly visible by the naked eye. Nevertheless, SPR experiments with BX

suspensions were performed for the elucidation of the effect of ionic groups on xylan adsorption. From stock solutions, polymer solutions were prepared by dilution with ultrapure water and were degassed before SPR experiments. Prior to data acquisition, the cellulose surfaces were allowed to reach equilibrium swelling as ultrapure water was flowed through the system. Once a stable baseline was established, polymer solutions were pumped into the flow cell. Each solution flowed over the sensor until adsorption ceased and was followed by a switch to water via the solvent selection valve. Key parameters extracted from SPR experiments were schematically depicted in Figure 3.11. Once a new baseline was achieved after water flowed through the flow cell, a solution with the next higher concentration was flowed over the sensor. This process was repeated in succession from the lowest to the highest concentration. The same procedure was followed for SPR experiments with SAM surfaces. For PC adsorption onto SAM-CH_3 surfaces, substantially longer equilibration times were required for each solution concentration. Therefore, separate SPR experiments were run for each PC solution concentration with freshly prepared SAM-CH_3 surfaces. Each SPR experiment was performed three times, and data points on the adsorption isotherms represented the average value with one standard deviation error bars.

For HPMAX adsorption onto SAM-COOH surfaces at different salt concentrations, salt solutions were flowed through the flow cell until a stable baseline was achieved. Next, a polymer solution with the same salt concentration was flowed through the flow cell. Polymer solution concentrations were 100 $mg \cdot L^{-1}$ and 20 $mg \cdot L^{-1}$ for HPMAX010 and HPMAX034, respectively. At these concentrations, the adsorbed amount corresponded to the plateau on the adsorption isotherms.

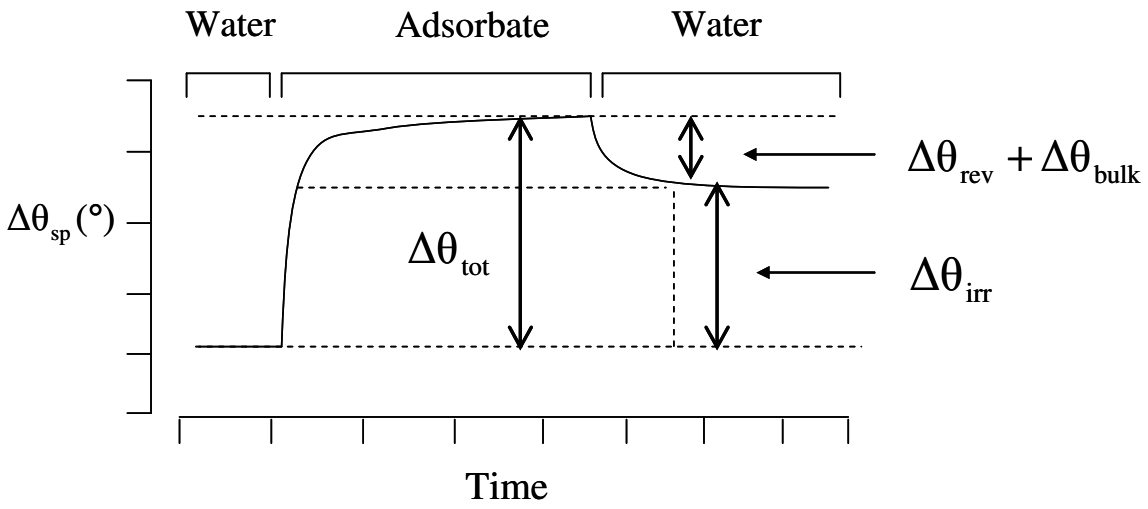

Figure 3.11: A schematic depiction of raw SPR data for the case where water was used to establish a baseline value for $\Delta\theta_{sp}$. A solution containing adsorbate produced a total change in $\Delta\theta_{sp}$ ($\Delta\theta_{tot}$). Switching from adsorbate solution to water eliminated the bulk contribution ($\Delta\theta_{bulk}$), removed reversibly bound adsorbate ($\Delta\theta_{rev}$), and yielded irreversibly bound adsorbate ($\Delta\theta_{irr}$).

3.2.10.1 Analysis of SPR Data

Refractive index changes in the vicinity of the gold surface were detected through changes in the resonant angle (θ_{sp}), the incident angle at which reflected light intensity was at a minimum.[211] θ_{sp} was sensitive to changes that occurred within ~200 nm of the surface, i.e. both adsorbed molecules and bulk concentration changes. This latter effect (bulk effect) produced a displacement in θ_{sp} with respect to analyte concentration. A schematic depiction of how θ_{sp} changed as analyte adsorbed onto the sensor surface and partially desorbed from the sensor surface after water flowed over the surface was provided as Figure 3.11. As shown in Figure 3.11, the total increase in the resonant angle ($\Delta\theta_{tot}$) corresponded to the observed change in the resonant angle ($\Delta\theta_{sp}$) caused by reversible adsorption ($\Delta\theta_{rev}$), irreversible adsorption ($\Delta\theta_{irr}$), and

the bulk effect ($\Delta\theta_{bulk}$). The decrease in $\Delta\theta_{sp}$ after water flowed over the surface corresponded to $\Delta\theta_{sp}$ caused by the desorption of some analyte molecules ($\Delta\theta_{rev}$) and elimination of $\Delta\theta_{bulk}$. The residual $\Delta\theta_{sp}$ corresponded to $\Delta\theta_{irr}$.[194]

$\Delta\theta_{tot}$ and $\Delta\theta_{irr}$ values were deduced for each solution concentration as depicted in Figure 3.11. Next, Eqns. 3.4 and 3.5 were used to obtain the change in the resonant angle associated with adsorption ($\Delta\theta_a = \Delta\theta_{rev} + \Delta\theta_{irr}$) was deduced by subtraction of the contribution of bulk refractive index changes in the dielectric medium from $\Delta\theta_{tot}$:

$$\Delta\theta_a = \Delta\theta_{tot} - c \bullet \frac{d\theta_{sp}}{dc} \tag{3.4}$$

where c was the bulk solution concentration, and

$$\frac{d\theta_{sp}}{dc} = \frac{d\theta_{sp}}{dn} \bullet \frac{dn}{dc} \tag{3.5}$$

where $(d\theta_{sp}/dn) = 61.5°$ was an instrument specific parameter obtained by calibration of the instrument with ethylene glycol standards. The surface excess (Γ) was calculated from $\Delta\theta_a$ for each concentration with the equation of de Feijter et al.:[193]

$$\Gamma = \frac{L\,(n_f - n)}{dn/dc} = \frac{\Delta\theta_a}{d\theta/dL}\frac{(n_f - n)}{dn/dc} \tag{3.6}$$

where, n_f was the refractive index of the film which was assumed to be 1.45, and $n \approx 1.32813$ was the refractive index of the solvent (water).[212] The other constant in Eq 3.6, $(d\theta/dL)$, was obtained from Fresnel calculations. Theoretical Fresnel calculations were carried out with a computer simulation program written in Matlab. The values of n and the thickness of the six layers used in the Fresnel calculations were summarized in Table 3.4. $(d\theta/dL)$ values for model cellulose and SAM surfaces were $(4.2 \pm 0.2) \times 10^{-3}$ and $(3.9 \pm 0.2) \times 10^{-3}$ deg•Å^{-1}, respectively.

The SAM value was in good agreement with the value of 4×10^{-3} deg•Å^{-1} previously reported by Tulpar *et al.* [195] dθ/dL values did not change with increasing NaCl concentration values.

Table 3.4: Layer parameters for SPR studies of polysaccharides.

	Layer	Thickness Å	Refractive Index n	Absorption Coefficient κ
L1	Sapphire prism	5×10^{6}	1.76074[213]	0
L2	Chromium	20	4.1106[214]	4.3492[214]
L3	Gold	480	0.174[214]	4.86[214]
L4	Cellulose or SAM	195[142] 16[215]	1.44[137] 1.45[215]	0 0
L5	Adsorbed Polymer Film	Variable	1.45[a]	0
L6	Water 1 mM NaCl 10 mM NaCl 100 mM NaCl	500	1.32813[212] 1.32814[b] 1.32823[b] 1.32910[b]	0

a. Assumed to be 1.45 which has generally been a good assumption for organic materials.
b. Refractive index increments of aqueous NaCl solutions at concentrations ranging from 0 to 1 M were calculated from data taken from CRC Handbook of Chemistry and Physics[216] and were found to be $(dn/dc) = (9.65 \pm 0.09) \times 10^{-3}\ M^{-1}$. The refractive index for L6 was computed by multiplying (dn/dc) by the salt concentration and adding this product to n for water at 20 °C (780 nm, n = 1.32813).[212]

CHAPTER 4

Surface Plasmon Resonance Studies of Pullulan and Pullulan Cinnamate Adsorption onto Cellulose

This chapter has been published in Biomacromolecules: "Surface Plasmon Resonance Studies of Pullulan and Pullulan Cinnamate Adsorption onto Cellulose," **A. Kaya**, X. Du, Z. Liu, J. W. Lu, J. R. Morris, W. G. Glasser, T. Heinze, and A. R. Esker, Biomacromolecules **2009**, (Accepted).

4.1 Abstract

Surface plasmon resonance studies showed pullulan cinnamates (PCs) with varying degrees of substitution (DS) adsorbed onto regenerated cellulose surfaces from aqueous solutions below their critical aggregation concentrations. Results on cellulose were compared to PC adsorption onto hydrophilic and hydrophobic self-assembled thiol monolayers (SAMs) on gold to probe how different interactions affected PC adsorption. PC adsorbed onto methyl-terminated SAMs (SAM-CH_3) > cellulose > hydroxyl-terminated SAMs (SAM-OH) for high DS and increased with DS for each surface. Data for PC adsorption onto cellulose and SAM-OH surfaces were effectively fit by Langmuir isotherms; however, Freundlich isotherms were required to fit PC adsorption isotherms for SAM-CH_3 surfaces. Atomic force microscopy images from the solid/liquid interfaces revealed PC coatings were uniform with surface roughnesses < 2 nm for all surfaces. This study revealed hydrogen bonding alone could not explain PC adsorption onto cellulose and hydrophobic modification of water soluble polysaccharides was a facile strategy for their conversion into surface modifying agents.

4.2 Introduction

Bone and wood, as biological structural materials, have been classical examples of complex composite materials.[217] In consideration of the relatively poor properties of the basic building blocks, the resulting composites demonstrated remarkable mechanical properties required for their function.[217, 218] These natural composites consisted of a polymer matrix reinforced with either crystallites or fibers, were hierarchically organized on different scales from nano to micron levels, and were sources of inspiration for the design of new materials.[219-221] These factors along with increased environmental consciousness and legislative mandates have driven interest in materials with the focus on renewable raw materials which mimicked natural composites.[220, 222]

Cellulose fibers have received greater attention for use in biocomposites, with substitution of one or more man-made materials in composite materials with a biologically derived component. However, the natural fiber-polymer interfaces have presented a formidable challenge for cellulose based biocomposites. Because of the presence of hydroxyl groups and other polar substances in various natural fibers, moisture absorption in biocomposites has led to poor interfacial bonding between polyhydroxyl fiber surfaces and the hydrophobic matrix component.[222, 223] Hence, modification of wood fiber surfaces has been a significant challenge for the production of novel biocomposites. Bonding between components could often be increased through derivatization of cellulosic fibers with hydrophobic moieties via an ester linkage. This process yielded improved compatibility between the cellulosic fibers and thermoplastics; however, derivatization of cellulose cleaved the glucan chain and disrupted the extensive hydrogen bonded network. As a consequence, derivatization undermined two important contributors to the strength of native cellulose materials. Since the successful

utilization of cellulose materials in many biocomposite applications required the retention of the crystalline character of the cellulose, more gentle modification of cellulose was required.[224] In this context, surface modification of cellulose fibers with adsorbed molecules has been an attractive option for the creation of better interfaces between cellulose and thermoplastics.

The self-aggregation of hydrophobically modified pullulan (HMP) has been previously studied in aqueous solutions,[225-233] as has HMP adsorption at the air/liquid,[231, 232, 234, 235] and solid/liquid interfaces.[236, 237] Akiyoshi et al. observed that chloresterol bearing pullulan (CHP) self-aggregated in aqueous solutions and formed stable nanoparticle hydrogels. The aggregation numbers calculated from the molecular weights of the aggregates corresponded to 10 to 12 for all CHPs regardless of their degrees of substitution (DS) by cholesterol groups.[229] In another study, HMP modified with dodecanoic acid showed a more compact conformation than the starting pullulan, and reduced the contact of alkyl groups with water.[232] When amphiphilic HMPs were monitored at the air/water interface by surface tension measurements, longer equilibration times were observed for the formation of the adsorbed layer.[232, 235, 238] Deme et al.[238] attributed the slow kinetics of the surface tension change to the reorganization of the adsorbed polymer chains at the air/water interface. Studies concerning HMP adsorption onto polystyrene at the solid/liquid interface involved hydrophobically modified 6-carboxypullulan[236] and carboxymethylpullulan.[237] Both of these studies revealed strong adsorption originated from hydrophobic interactions between the polymer and polystyrene.[236, 237] Nonetheless, systematic studies of HMP adsorption at solid/liquid interfaces, where the solid surfaces were both hydrophilic and hydrophobic, have largely been absent.

This study systematically probed HMP adsorption from aqueous solution onto both hydrophilic and hydrophobic solid surfaces. Modification of a water soluble polysaccharide,

pullulan (P), through esterification with cinnamic acid as depicted in Figure 3.1 yielded a series of pullulan cinnamate (PC) derivatives with controlled DS. In general, the DS of these samples were low [< 1 cinnamate group per 12 anhydroglucose units (AGUs)] to ensure the PC derivatives remained soluble in water. Pullulan was chosen as a water-soluble model for a hemicellulose, while cinnamic acid was chosen for derivatization because of its structural similarity to lignin. Thus, the resulting PCs were structurally similar to a lignin-carbohydrate complex. Aggregate formation of PCs in aqueous solution was probed by surface tension and pyrene dye fluorescence measurements. Surface plasmon resonance (SPR) and in situ atomic force microscopy (AFM) experiments explored PC adsorption onto alkane thiol self-assembled monolayers (SAMs) and regenerated cellulose surfaces at concentrations well below the critical aggregation concentrations (CACs) of the PC derivatives. The regenerated cellulose films were easily prepared models for the amorphous portion of cellulose I surfaces. Collectively, these studies revealed the relative contributions of hydrophilic and hydrophobic interactions to PC adsorption from solution, an important starting point for future studies of interactions that might be relevant to cell wall biogenesis.

4.3 Experimental

Synthesis and characterization of pullulan cinnamates was described in Section 3.1.1. Procedures for surface tension measurements and pyrene dye fluorescence measurements were described in Section 3.2.5 and Section 3.2.6, respectively. Finally, procedures for in-situ AFM measurements and SPR experiments were described in Sections 3.2.9 and 3.2.10, respectively.

4.4 Results and Discussion

4.4.1 Surface Tension Measurements

Surface tension measurements and pyrene dye fluorscence measurements discussed in Section 4.3.2 probed pullulan cinnamate aggregation in aqueous solution. Unmodified pullulan exhibited no surface activity at the air/water interface as previously reported,[231, 238] and in contrast to pullulan modified with chloresterol groups,[235] dodecanoic acid,[232] and abietic acid,[239] and carboxymethyl pullulan modified with dodecyl, decyl, and hexyl groups.[231] These HMPs usually decreased the surface tension of water through progressive polymer adsorption at the air/water interface.[231] A plot of surface tension (γ) versus time for 1 g•L^{-1} P and PC solutions was provided as Figure 4.1. The surface tension of P and the lowest DS PC (PC003) were the same as the surface tension of water (γ_{water}).However, higher DS PC derivatives caused a slight depression of the surface tension, $\Delta\gamma = \gamma_{water} - \gamma_{PC}(aq)$, where $\gamma_{PC}(aq)$ was the surface tension of the pullulan cinnamate solution. The maximum change in surface tension ($\Delta\gamma_{max} = \Delta\gamma$ after 1000 min) was ~ 1.5 mN·m^{-1} and ~ 2.8 mN·m^{-1} for PC006 and PC008, respectively. These $\Delta\gamma_{max}$ values were relatively small compared to other HMP derivatives.[231, 232, 235, 239] These small surface tension changes were consistent with cinnamate groups in PC molecules that were too short for the formation of ordered structures at the air/water interface. It was also consistent with very high CACs for PCs. As discussed later in this chapter, the meager surface activity of PCs at the air/water interface was not correlated with a lack of PC surface activity at the cellulose/water interface.

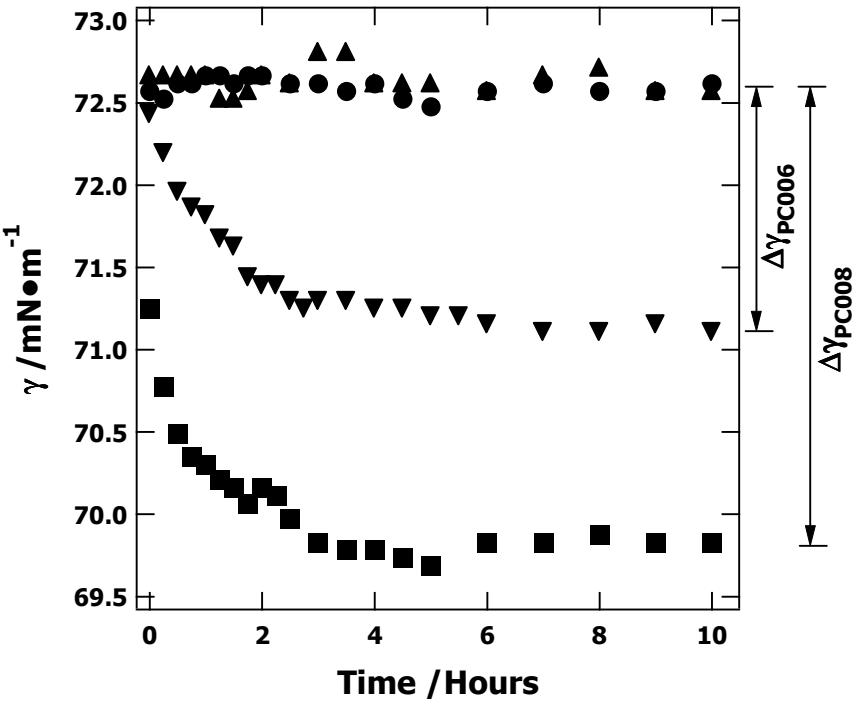

Figure 4.1: γ versus time for P and PC adsorption from a 1 g•L^{-1} solution at the air/water interface at 20.0 ºC. Symbols corresponded to (▲) P, (●) PC003, (▼) PC006, and (■) PC008.

4.4.2 Pyrene Dye Fluorescence Measurements

A plot of I_1/I_3 for solutions that contained a fixed concentration of pyrene and variable concentrations of P and PCs was provided as Figure 4.2. The ratio I_1/I_3 decreased as the local environment for the pyrene probe became more hydrophobic. As seen in Figure 4.2, the I_1/I_3 ratio was constant for P and PC at concentrations below ~ 3 g•L^{-1} (approximately 3X larger than the highest concentration used for SPR and AFM adsorption studies). For P and PC003, the I_1/I_3 ratio only decreased slightly for concentrations > ~ 10 g•L^{-1}. In contrast, I_1/I_3 decreased sharply with increasing concentration from ~ 10 and ~3 g•L^{-1} for PC006 and PC008, respectively. The addition of cinnamate groups to pullulan induced aggregation, however, the CACs were > 3 g•L^{-1} for all PC derivatives used in this study. The surface tension experiments along with the pyrene

dye fluorescence measurements indicated that all SPR and AFM adsorption studies were carried out at concentrations at least a factor of three below the CAC.

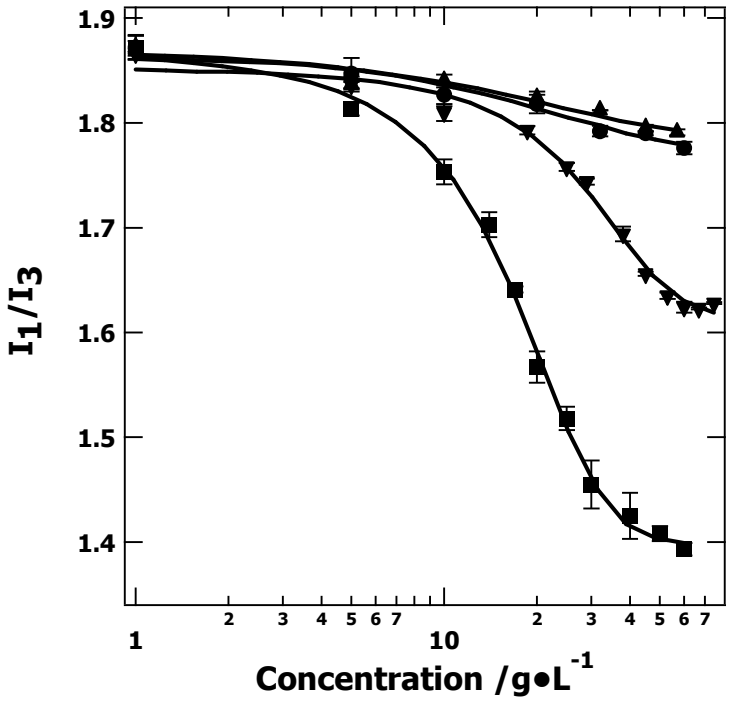

Figure 4.2: I_1/I_3 ratios as a function of bulk solution concentration for (▲) P, (●) PC003, (▼) PC006, and (■) PC008. All samples contained 10^{-6} M pyrene dye. The solid lines were the sigmodial fits to the experimental data.

4.4.3 PC Adsorption onto Regenerated Cellulose Surfaces

Representative raw SPR data for the adsorption of P and the three PCs onto regenerated cellulose surfaces were provided in Figure 4.3. Each individual experiment was carried out three times and values for $\Delta\theta_{tot}$ and $\Delta\theta_{irr}$ for each concentration were extracted from the SPR raw data as depicted in Figure 3.11. $\Delta\theta_{tot}$ (A) and $\Delta\theta_{irr}$ (B) as a function of concentration for each polymer with one standard deviation error bars were shown in Figure 4.4. There was no significant adsorption of P onto regenerated cellulose surfaces. There was a slight increase in the amount of PC003 that adsorbed onto cellulose relative to P, while PC006 and PC008 adsorbed even more

strongly onto cellulose from aqueous solution. The amount of PC006 adsorbed onto cellulose from an aqueous solution was almost 3 times greater than PC003, whereas the amount of PC008 adsorbed onto regenerated cellulose was almost 6 times greater. These results suggested that PC adsorption onto regenerated cellulose surfaces was facilitated by cinnamate groups of the PCs in a hydrophobically driven process. As seen in Figure 4.4, most of the adsorbed polymer was irreversibly bound for all polymers.

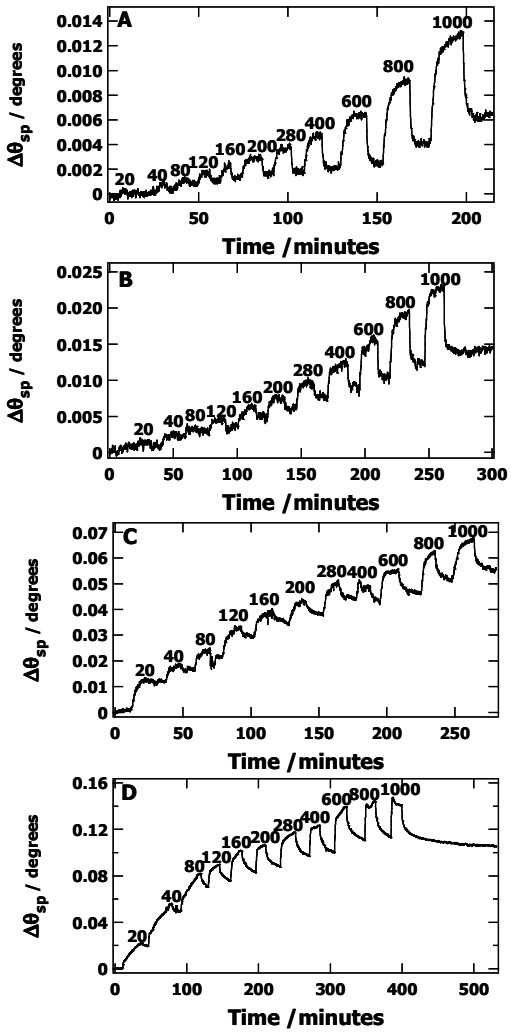

Figure 4.3: Representative SPR data for P and PC adsorbed onto cellulose regenerated from spin-coated TMSC films at 20.0 °C. Graphs A through D correspond to P, PC003, PC006, and PC008, respectively. Solution concentrations in units of $mg \cdot L^{-1}$ correspond to the numbers on A-D. Water was flowed through the SPR instrument before and after each new adsorbate solution.

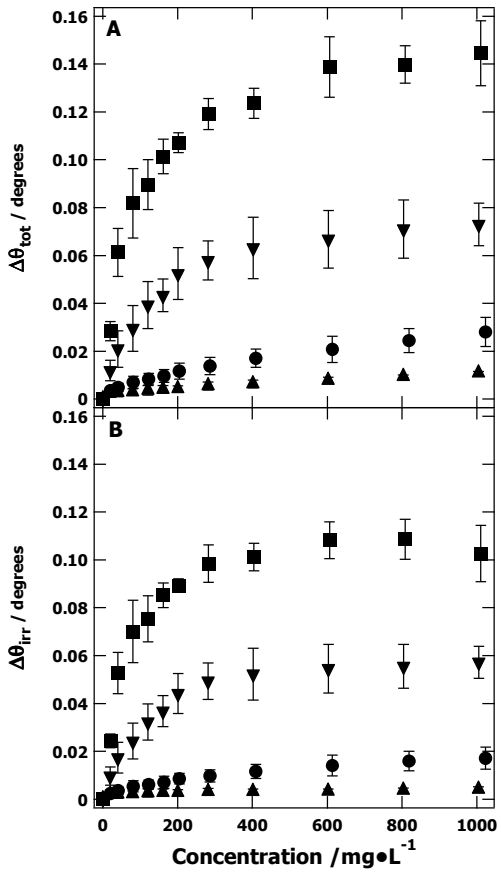

Figure 4.4: (A) $\Delta\theta_{tot}$ and (B) $\Delta\theta_{irr}$ versus concentration for P and PCs adsorbed onto regenerated cellulose surfaces at 20.0 °C. Symbols correspond to (▲) P, (●) PC003, (▼) PC006, and (■) PC008 with one standard deviation error bars.

4.4.4 PC Adsorption onto SAM-OH Surfaces

Representative raw SPR data for the adsorption of P and PCs onto SAM-OH surfaces were provided as Figure 4.5. Each individual experiment was carried out three times and the values for $\Delta\theta_{tot}$ and $\Delta\theta_{irr}$ for each concentration were extracted from the SPR raw data. $\Delta\theta_{tot}$ and $\Delta\theta_{irr}$ versus the concentration of each polymer with one standard deviation error bars were provided as Figure 4.6. There was no significant adsorption of P onto SAM-OH surfaces, just as there was no significant P adsorption onto regenerated cellulose. Qualitatively, a similar trend was observed for PC adsorption onto the SAM-OH surfaces as for PC adsorption onto cellulose.

PC adsorption onto the SAM-OH surfaces increased as cinnamate DS increased. Quantitatively, there was an interesting difference for all PCs. PC003 actually adsorbed onto regenerated cellulose to a lesser extent than onto the SAM-OH surface. PC006 adsorbed at approximately the same level onto the cellulose and SAM-OH surfaces. In contrast, substantially less PC008 adsorbed onto the SAM-OH surface than onto cellulose. Different trends for PC adsorption onto SAM-OH and cellulose surfaces indicated that interactions between polar groups such as hydrogen bonding were not the only factors involved with PC adsorption onto cellulose.

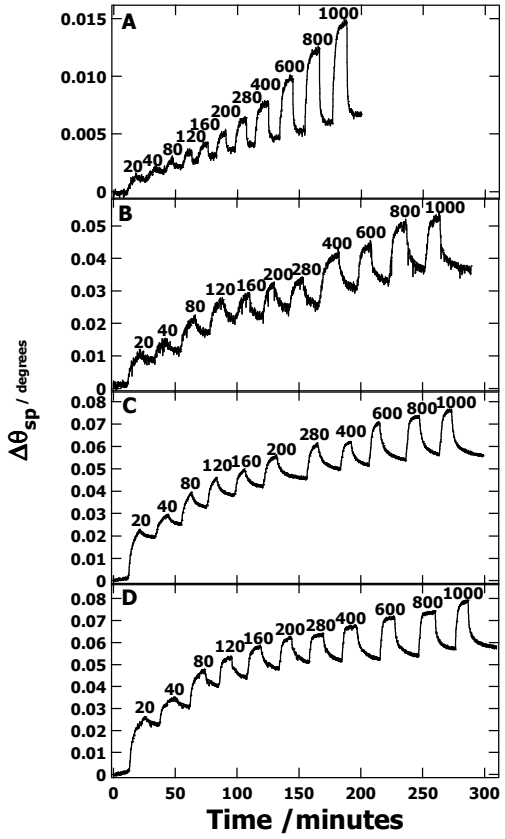

Figure 4.5: Representative SPR data for P and PC adsorbed onto SAM-OH surfaces at 20.0 °C. Graphs A through D correspond to P, PC003, PC006, and PC008, respectively. Solution concentrations in units of $mg \cdot L^{-1}$ correspond to the numbers on A through D. Water was flowed through the SPR instrument before and after each new adsorbate solution.

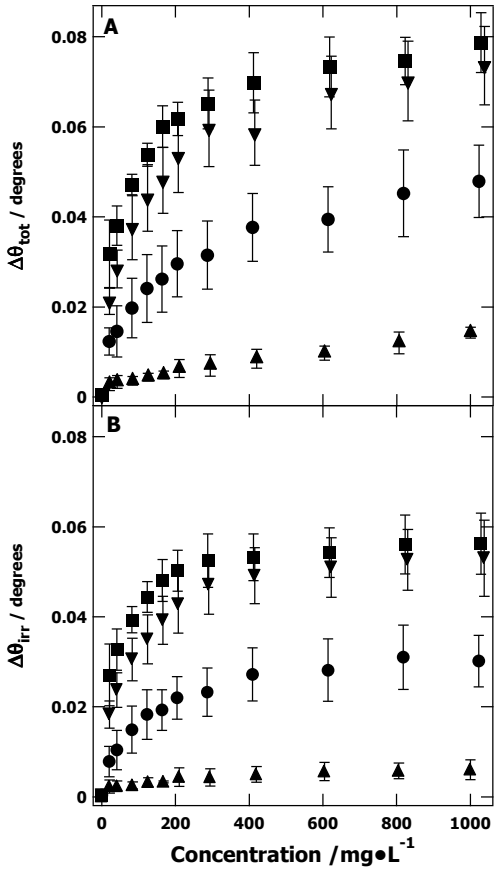

Figure 4.6: (A) $\Delta\theta_{tot}$ and (B) $\Delta\theta_{irr}$ versus concentration for P and PCs adsorbed onto SAM-OH surfaces at 20.0 °C. Symbols correspond to (▲) P, (●) PC003, (▼) PC006, and (■) PC008 with one standard deviation error bars. Note that the axis ranges are one-half the range of the analogous plot in Figure 4.4.

4.4.5 PC Adsorption onto SAM-CH_3 Surfaces

Representative raw SPR data for the adsorption of P and PCs onto SAM-CH_3 surfaces were provided as Figure 4.7. Preliminary experiments, analogous to Figure 4.4, revealed that the adsorption kinetics were slow and adsorption nearly saturated by a solution concentration of ~ 200 mg·L^{-1} for PC adsorption onto SAM-CH_3 surfaces. As a consequence of the slow adsorption kinetics, SPR experiments for PC adsorption onto SAM-CH_3 surfaces were run for each concentration on freshly prepared surfaces. High levels of adsorption occurred even at extremely

low concentrations because of the high affinity of the cinnamate groups for the SAM-CH_3 surfaces. The observed $\Delta\theta_{tot}$ for the lowest PC concentration studied, ~ 0.04 $mg \cdot L^{-1}$, was approximately 40% of $\Delta\theta_{tot}$ observed for the highest PC concentration studied, ~ 200 $mg \cdot L^{-1}$. Each individual experiment was carried out three times and the values for $\Delta\theta_{tot}$ and $\Delta\theta_{irr}$ for each concentration were extracted from the raw SPR data. $\Delta\theta_{tot}$ and $\Delta\theta_{irr}$ versus the solution concentration for each polymer with one standard deviation error bars were provided as Figure 4.8. As seen in Figure 4.8, adsorption onto SAM-CH_3 surfaces increased as cinnamate DS increased. This behavior was analogous to results obtained for the adsorption of hydrophobically modified 6-carboxypullulans onto polystyrene thin films[236] and hydrophobically modified carboxymethylpullulan onto polystyrene latex particles.[237] Moreover, P and PC adsorption onto the hydrophobic SAM-CH_3 surface was even stronger than onto the cellulose and SAM-OH surfaces.

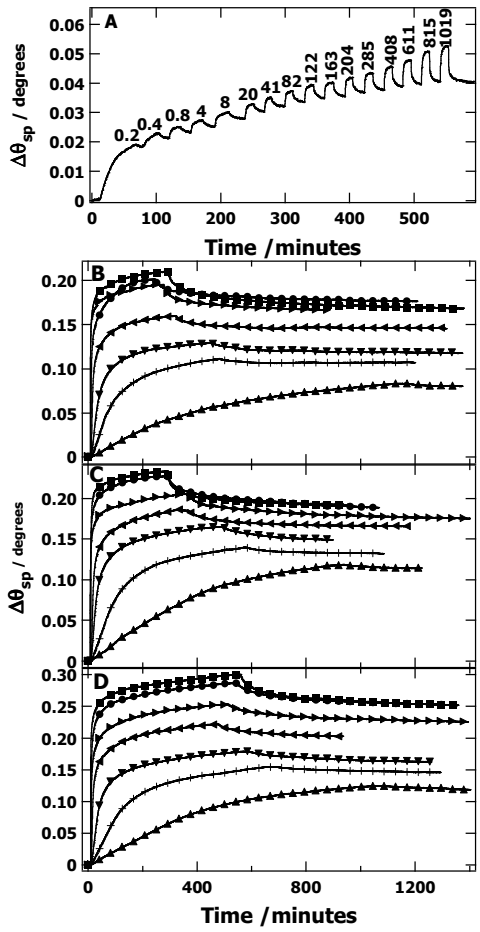

Figure 4.7: Representative SPR data for P and PC adsorbed onto SAM-CH_3 surfaces at 20.0 °C. Graphs A through D correspond to P, PC003, PC006, and PC008, respectively. Solution concentrations in units of $mg \cdot L^{-1}$ correspond to the numbers on (A), where water was flowed through the SPR instrument before and after each new adsorbate solution. Symbols on (B) through (D) correspond to different solution concentrations: (▲) 0.04, (+) 0.2, (▼) 0.8, (◄) 4, (►) 20, (●) 80, and (■) 200 $mg \cdot L^{-1}$.

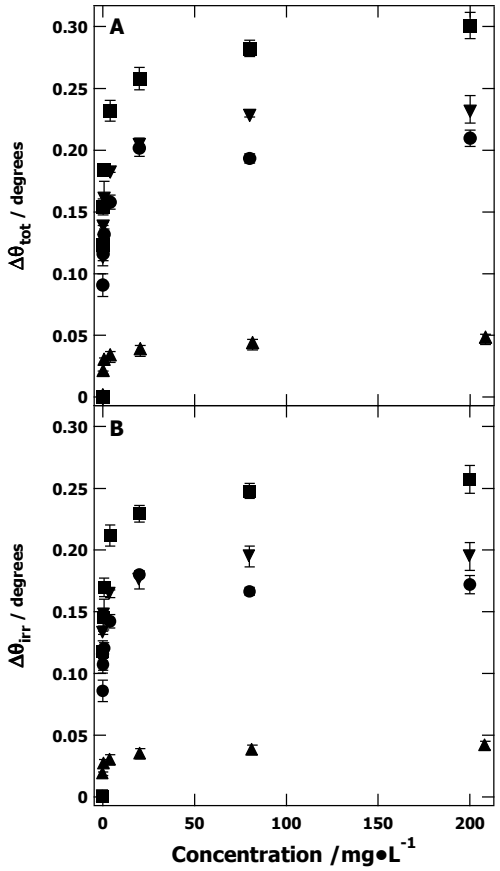

Figure 4.8: (A) $\Delta\theta_{tot}$ and (B) $\Delta\theta_{irr}$ versus concentration for the adsorption of P and PCs onto SAM-CH_3 surfaces at 20.0 °C. Symbols correspond to (▲) P, (●) PC003, (▼) PC006, and (■) PC008 with one standard deviation error bars. Note that the y-axis ranges are approximately twice the range of the analogous plot in Figure 4.4.

4.4.6 AFM Studies of P and PC Adsorption onto Regenerated Cellulose and SAM Surfaces

Representative *in situ* AFM images of the solid/liquid interface for regenerated cellulose, SAM-OH, and SAM-CH_3 surfaces on template stripped gold surfaces prior to adsorption studies and the same surfaces after exposure to 1 g·L^{-1} polymer (P and PC derivatives) solutions for 2 h and water for another hour were provided in Figures 4.9, 4.10 and 4.11, respectively. Table 4.1 summarized the root-mean-square (RMS) roughnesses obtained from the images in Figures 4.9 - 4.11. The small surface roughnesses (< 2 nm) and the surface morphologies were consistent with

generally uniform coverage of the model surfaces by high DS PC derivatives and insignificant adsorption by P and low DS PC derivatives.

Table 4.1: RMS surface roughnesses at the solid/liquid interface before and after P and PC adsorption onto regenerated cellulose, SAM-OH, and SAM-CH_3 surfaces from 1 $g \cdot L^{-1}$ aqueous solutions.

Adsorbed Polymer	Regenerated Cellulose (nm)		SAM-OH (nm)		SAM-CH_3 (nm)	
	Before	After	Before	After	Before	After
P	0.83	0.94	0.73	0.87	0.63	0.72
PC003	0.74	0.92	0.61	0.76	0.71	0.87
PC006	0.74	1.08	0.67	1.18	0.83	1.17
PC008	0.79	1.53	0.63	1.29	0.79	1.43

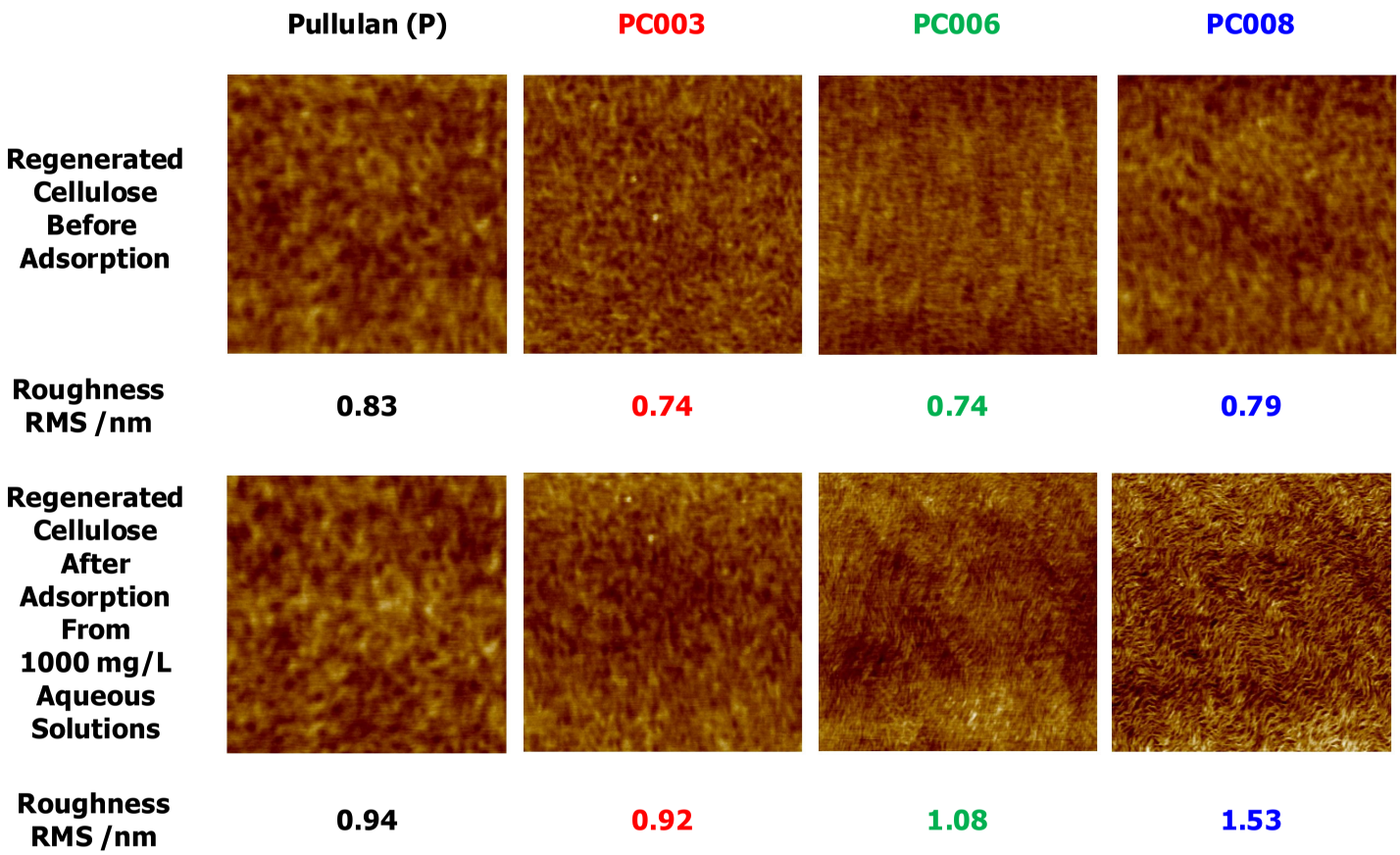

Figure 4.9: Representative AFM height images of the solid/liquid interface of regenerated cellulose surfaces before and after PC adsorption. The AFM images are 2 μm x 2 μm and have Z-axis scales of 0 to 20 nm. RMS surface roughnesses are indicated under each picture.

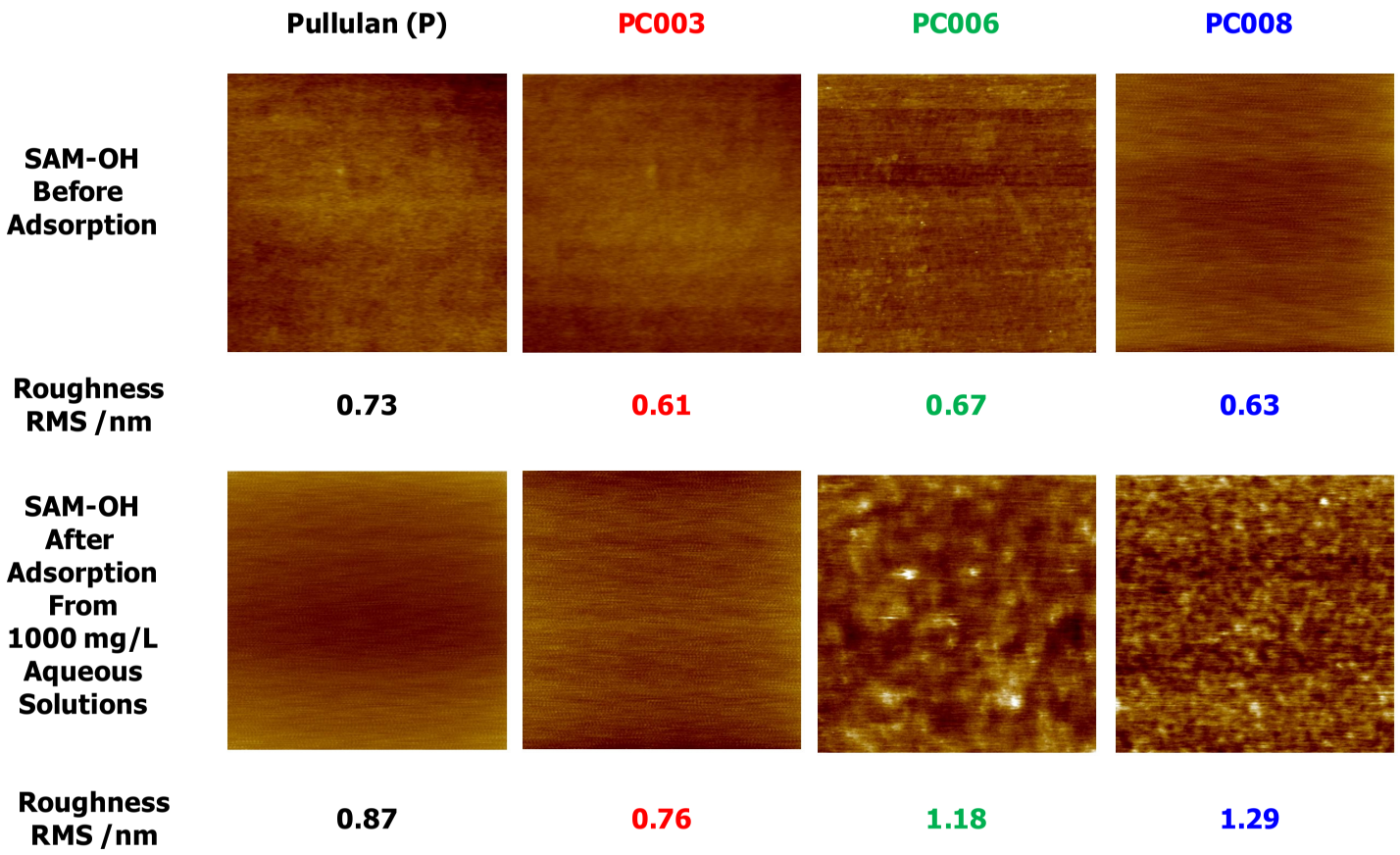

Figure 4.10: Representative AFM height images of the solid/liquid interface of SAM-OH surfaces before and after PC adsorption. The AFM images are 2 μm x 2 μm and have Z-axis scales of 0 to 20 nm. RMS surface roughnesses are indicated under each picture.

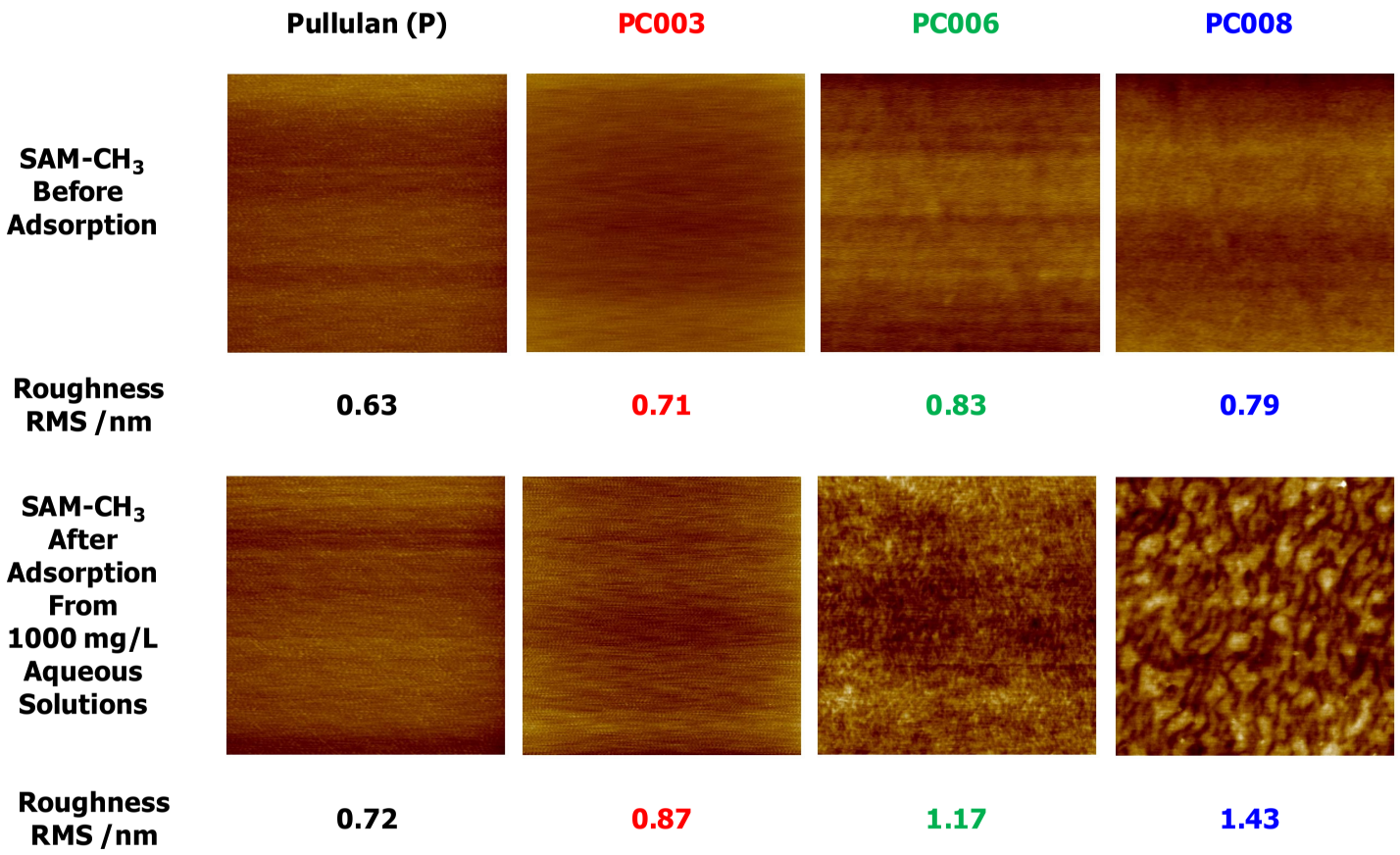

Figure 4.11: Representative AFM height images of the solid/liquid interface of SAM-CH_3 surfaces before and after PC adsorption. The AFM images are 2 μm x 2 μm and have Z-axis scales of 0 to 20 nm. RMS surface roughnesses are indicated under each picture.

4.4.7 Surface Excess (Γ) Values

Values of the adsorbed surface excess or surface concentration (Γ) were deduced from the values of $\Delta\theta_{tot}$ in Figures 4.4, 4.6 and 4.8 using Eqs. 3.4 through 3.6. These deduced values were plotted in Figure 4.12 for all three surfaces. As expected from Figures 4.4, 4.6 and 4.8, there were large differences in the maximum adsorbed amounts (Γ_{max}) for P and PC adsorption onto different surfaces.

Additional information about the adsorption isotherms came from fits with the Langmuir isotherm:

$$\Gamma = \frac{\Gamma_m \bullet K_L \bullet C}{1 + K_L \bullet C} \tag{4.1}$$

where K_L was the Langmuir constant, C was the bulk concentration of the adsorbate, and Γ_m was the maximum surface concentration at infinite bulk concentration.[62] The Langmuir isotherm was developed for equilibrium adsorption onto homogeneous surfaces. The key assumptions of the Langmuir adsorption isotherm were non-interacting, equivalent adsorption sites, a homogeneous surface that lacked dislocations or any other structural non-idealities that induced preferential adsorption, and maximal adsorption of a single monolayer, whereby K_L was effectively the equilibrium constant which was equal to the ratio of the adsorption rate constant (k_{ads}) to the desorption rate constant (k_{des}).[60] Hence, Langmuir isotherms have frequently been applied to gas adsorption onto solid surfaces. In contrast, most cases for polymer adsorption onto solid surfaces have been irreversible with multilayer formation, even at very low solution concentrations. As such, polymer adsorption isotherms have been called high affinity isotherms. While the phenomenological bases for gas and polymer adsorption isotherms differed, the shapes of high affinity isotherms have been found to be similar to a Langmuir adsorption isotherm. For cases

where Γ_{max} has exceeded monolayer coverage and failed to plateau, an empirical Freundlich isotherm has provided reasonable fits of experimental data.[64]

All isotherms in Figure 4.12 were initially fit with the Langmuir and Freundlich models. Fitting parameters for both approaches were summarized in Table 4.2. For the cases of the regenerated cellulose and SAM-OH surfaces, the Langmuir model provided a superior fit. As seen in Figures 4.12B and 4.12C, PC adsorption onto the regenerated cellulose and SAM-OH surfaces was well described by the Langmuir model. Estimated K_L values for cellulose surfaces (0.012 ± 0.002) and SAM-OH surfaces (0.029 ± 0.008) did not show any correlation with PC DS, while $\Gamma_{max} = \Gamma_m$ systematically increased with DS. As Figures 4.9 and 4.10 showed that the adsorbed layers on regenerated cellulose and SAM-OH surfaces were uniform and smooth, the parameters from the Langmuir model were deemed a reasonable representation of the adsorption isotherm.

In contrast to regenerated cellulose and SAM-OH surfaces, PC adsorption onto SAM-CH_3 surfaces did not plateau at large bulk solution concentrations and as a consequence, the Langmuir model did not adequately fit the experimental data (Figure 4.12). Another adsorption isotherm, the Freundlich isotherm:[64]

$$\Gamma = K_F \bullet C^{1/n_F} \tag{4.2}$$

where K_F was the adsorbent capacity, C was the bulk concentration, and $1/n_F$ was the adsorption affinity constant, provided reasonable fits in these situations. Empirical Freundlich adsorption isotherms have described heterogeneous systems[63] and its derivation assumed exponentially increasing heats of adsorption as surface coverage increased.[57] Hence, Freundlich adsorption isotherms have described cases where adsorption continually increased beyond monolayer coverage with increased polymer solution concentration. As seen in Figure 4.12, the Freundlich

isotherm provided a good fit of the adsorption isotherms for PC adsorption onto SAM-CH_3 surfaces. For fitting results summarized in Table 4.2, K_F increased with DS as a reflection of the increasingly hydrophobic character of the PC derivatives. In contrast, $1/n_F$ was relatively independent of PC DS and was on the order of 0.10. Nonetheless, AFM images in Figure 4.11 showed these thicker layers were still fairly uniform and smooth and suggested utilization of the Freundlich isotherm as a description of the adsorption isotherm was reasonable.

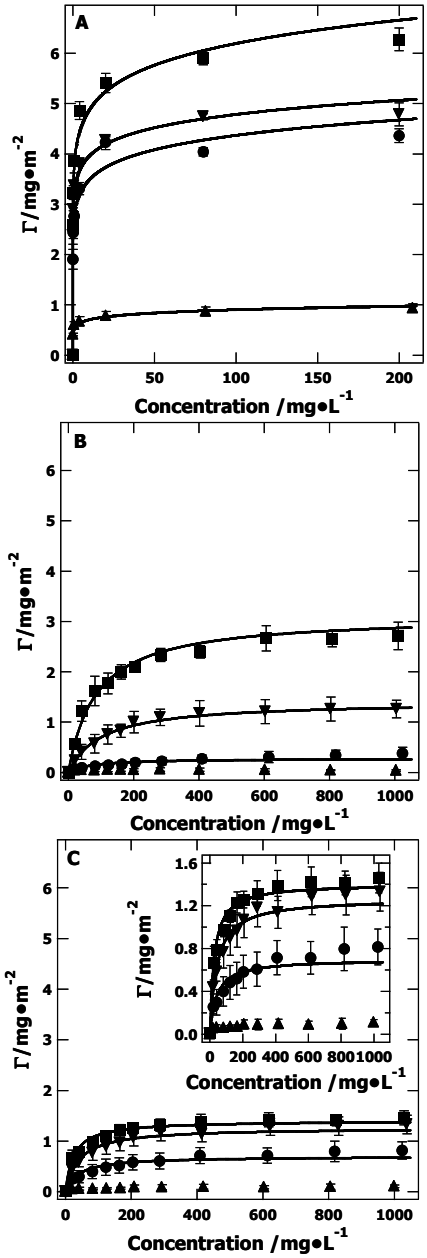

Figure 4.12: Adsorption isotherms for the adsorption of P and PCs onto (A) SAM-CH_3, (B) regenerated cellulose, and (C) SAM-OH surfaces at 20.0 °C. Symbols correspond to (▲) P, (●) PC003, (▼) PC006, and (■) PC008 with one standard deviation error bars. The inset of (C) simply expands the relevant y-axis range to more clearly show the trend. The solid lines in (A) represent fits with Freundlich isotherms, whereas solid lines in (B) and (C) represent fits with Langmuir isotherms.

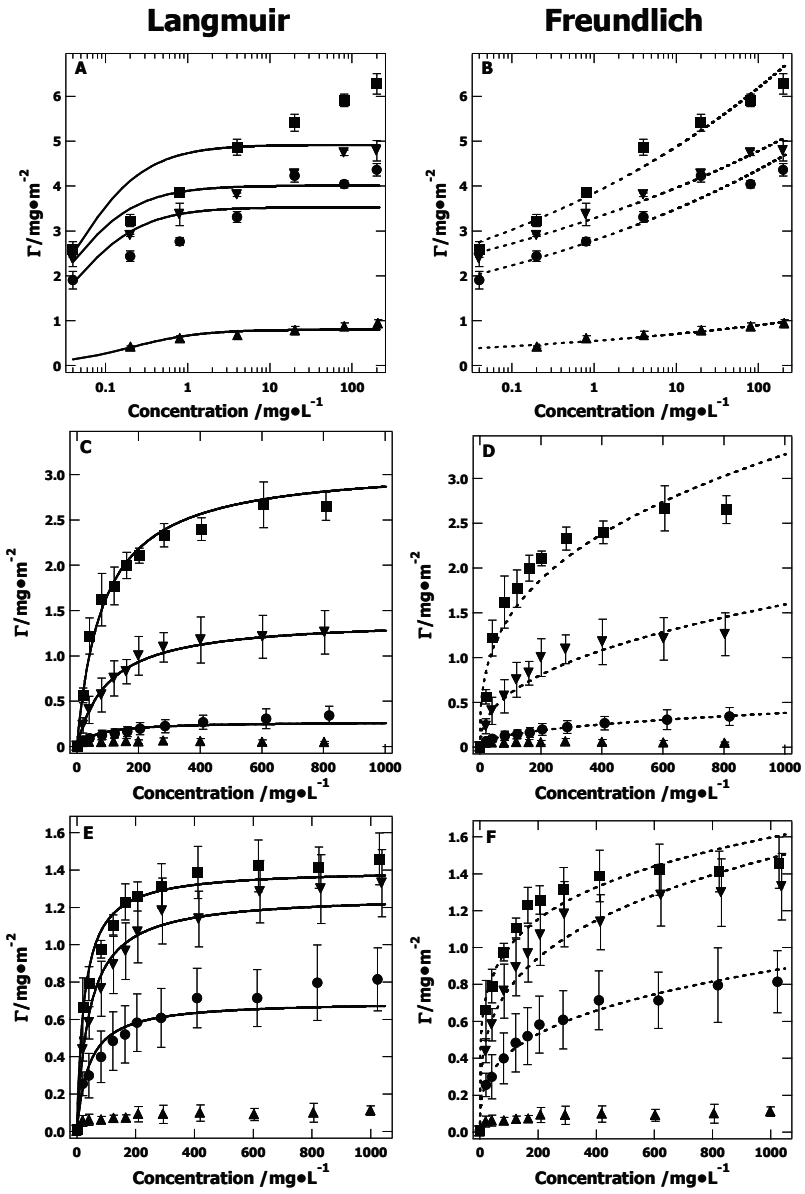

Figure 4.13: Adsorption isotherms for P and PC adsorption onto (A) and (B) SAM-CH_3, (C) and (D) regenerated cellulose, and (E) and (F) SAM-OH surfaces at 20.0 °C. Symbols correspond to P (▲), PC003 (●), PC006 (▼), and PC008 (■) with one standard deviation error bars. The solid lines in (A), (C), and (E) represent fits with Langmuir isotherms, whereas the dashed lines in (B), (D), and (F) represent fits with Freundlich isotherms. (A) and (B) use a semi-logarithmic scale to better show the fitting curves at low surface concentrations.

Table 4.2: Isotherm parameters for P and PC adsorption onto different surfaces.

Polymer	Surface	Γ_m ($mg \bullet m^{-2}$)[a]	K_L ($L \bullet mg^{-1}$)[a]	Coefficient of Determination (R^2)[a]	K_F ($L \bullet m^{-2}$)[b]	$1/n_F$[b]	Coefficient of Determination (R^2)[b]	Maximum $\Delta\theta_a$ degrees	Γ_{max}[c] ($mg \bullet m^{-2}$)	d_{max}[c] (Å)
P	Cellulose	—	—	—	—	—	—	0.002±0.001	0.06±0.03	0.8±0.4
PC003	Cellulose	0.27±0.03	0.015±0.002	0.964	0.018±0.001	2.26±0.04	0.998	0.019±0.006	0.27±0.03	3.2±0.4
PC006	Cellulose	1.41±0.05	0.009±0.001	0.998	0.09±0.02	2.4±0.3	0.954	0.064±0.009	1.41±0.05	17±1
PC008	Cellulose	3.11±0.26	0.011±0.001	0.986	0.30±0.08	2.9±0.4	0.923	0.14±0.01	3.11±0.26	37±3
P	SAM-OH	—	—	—	—	—	—	0.005±0.001	0.11±0.03	1.3±0.4
PC003	SAM-OH	0.70±0.05	0.025±0.003	0.952	0.10±0.01	3.2±0.2	0.988	0.038±0.009	0.70±0.05	8±1
PC006	SAM-OH	1.26±0.05	0.024±0.002	0.986	0.21±0.03	3.6±0.3	0.968	0.064±0.009	1.26±0.05	15±1
PC008	SAM-OH	1.40±0.05	0.040±0.003	0.974	0.39±0.04	4.9±0.5	0.960	0.069±0.007	1.40±0.05	17±1
P	SAM-CH_3	0.80±0.05	5.1±0.8	0.963	0.55±0.03	9±1	0.965	0.045±0.004	0.93±0.08	11±1
PC003	SAM-CH_3	3.5±0.3	27±7	0.875	2.79±0.09	10±1	0.974	0.21±0.01	4.36±0.14	52±2
PC006	SAM-CH_3	4.0±0.3	34±9	0.873	3.28±0.06	12.2±0.9	0.988	0.23±0.01	4.79±0.24	58±3
PC008	SAM-CH_3	4.9±0.5	26±7	0.871	3.84±0.09	9.6±0.7	0.986	0.30±0.01	6.28±0.23	75±3

a. Determined by fitting the data to a linearized Langmuir model: $\frac{1}{\Gamma} = \frac{1}{\Gamma_m} + \left(\frac{1}{\Gamma_m \bullet K_L}\right)\frac{1}{C}$

b. Determined by fitting the data to a linearized Freundlich model: $\ln\Gamma = \ln K_F + \left(\frac{1}{n_F}\right) \bullet \ln C$

c. From a Langmuir fit for PC adsorption onto SAM-OH and cellulose surfaces and from $\Delta\theta_a$ at the maximum bulk concentration for PC adsorption onto all surfaces and PC adsorption onto SAM-CH_3 surfaces.

The key observed parameters for P and PC adsorption onto the different surfaces, Γ_{max} and the maximum film thickness (d_{max}) obtained with the assumption that the film had n_f = 1.45, were summarized in Table 4.3. For PC adsorption onto cellulose and SAM-OH surfaces, Γ_{max} were simply Γ_m obtained from Langmuir adsorption isotherm fits. For the case of the SAM-CH_3 surface, $\Delta\theta_a$ at the highest studied bulk concentration (200 mg·L^{-1}) was used to calculate Γ_{max}. d_{max} values were then calculated from Γ_{max}. Key parameters for the calculation of d_{max} were summarized in Table 4.2.

As seen in Table 4.3, Γ_{max} systematically increased with cinnamate DS for all surfaces. For adsorption onto SAM-OH and cellulose surfaces, Γ_{max} values followed a similar trend. However, weaker adsorption of PC003 onto cellulose than onto SAM-OH, and the higher adsorption of PC008 onto cellulose than onto SAM-OH surfaces indicated that hydrophobic interactions played a significant role in the mechanism for PC adsorption onto cellulose surfaces. The latter comparison was somewhat analogous to the adsorption of poly(ethylene oxide) alkyl ethers onto cellulose surfaces, where adsorption onto cellulose was stronger than onto hydrophilic silica surfaces.[240] A comparison of PC adsorption onto cellulose and SAM-CH_3 surfaces revealed, Γ_{max} values for hydrophobic SAM-CH_3 surfaces were substantially greater than Γ_{max} values for cellulose surfaces. This result was interesting because the trend was the opposite of a previous study with hexadecyltrimethylammonium bromide (C_{16}TAB), where only enough C_{16}TAB adsorbed onto hydrophobic surfaces to form a monolayer,[241] but greater amounts adsorbed onto cellulose.[240, 241] The observation that PC adsorbed more strongly onto SAM-CH_3 surfaces than cellulose likely meant strong hydrophobic interactions between cinnamate groups and SAM-CH_3 molecules promoted the formation of thicker, highly looped PC aggregates on SAM-CH_3 surfaces.

Table 4.3: Observed Γ_{max} values for P and PC adsorption onto various surfaces.[a]

Polymer	Cellulose		SAM-OH		SAM-CH_3	
	Γ_{max}[b] (mg•m^{-2})	d_{max} (Å)	Γ_{max}[b] (mg•m^{-2})	d_{max} (Å)	Γ_{max}[c] (mg•m^{-2})	d_{max} (Å)
P	0.06±0.03[c]	0.8±0.4	0.11±0.03[c]	1.3±0.4	0.93±0.08	11±1
PC003	0.27±0.03	3.2±0.4	0.70±0.05	8±1	4.36±0.14	52±2
PC006	1.41±0.05	17±1	1.26±0.05	15±1	4.79±0.24	58±3
PC008	3.11±0.26	37±3	1.40±0.05	17±1	6.28±0.23	75±3

a. Assumed $n_f \sim 1.45$.
b. $\Gamma_{max} = \Gamma_m$ for Langmuir isotherm fits.
c. Γ_{max} was calculated from $\Delta\theta_a$ observed at 200 mg·L^{-1}.

4.4.8 Discussion

4.4.8.1 Relationship Between Γ_{max} and Molecular Dimensions

The values of Γ_{max} in Table 4.3 were interesting when compared to the value of a polysaccharide monolayer adsorbed flat on a surface. For a flat polysaccharide monolayer, $\Gamma_{max} \sim 0.45$ mg•m^{-2} with a cross-sectional area of ~60 Å^2•molecule^{-1} and hence a thickness of $d_{max} \sim 5.4$ Å.[242] Γ_{max} values in Table 4.3 showed that P did not adsorb onto regenerated cellulose or SAM-OH surfaces at even the monolayer level (i.e. submonolayer coverage), whereas thicker films (> monolayer coverage) were observed for P adsorption onto SAM-CH_3 surfaces. With the exception of PC003, PC adsorption onto cellulose was greater than onto SAM-OH surfaces and increased with DS. For the case of PC003, adsorption onto cellulose and SAM-OH surfaces yielded films on the order of monolayer coverage. For the higher DS samples, PC006 and PC008 adsorbed onto SAM-OH surfaces in comparable amounts (~ 3 "monolayers"). On the basis of these observations, it could be concluded that hydrogen bonding to the homogeneous SAM-OH and cellulose surfaces was important for PC adsorption onto hydrophilic surfaces. While PC006 also adsorbed onto cellulose to a similar extent as onto SAM-OH surfaces (~3 "monolayers"),

PC008 adsorbed more strongly onto cellulose (~7 "monolayers") than onto SAM-OH surfaces (~3 "monolayers"). The latter observation showed that PC adsorption onto cellulose could not arise solely from hydrogen bonding and that enhanced interactions between hydrophobes with higher DS enhanced adsorption onto cellulose. Adsorption of P and PC onto SAM-CH_3 surfaces clearly yielded films several monolayers thick. Furthermore, PC adsorption onto the SAM-CH_3 surfaces was a factor of 2 stronger than PC adsorption onto regenenerated cellulose for the highest DS. For PC008 adsorption onto cellulose, the thickness was ~7 “monolayers,” whereas the thickness was on the order of ~14 “monolayers” for the SAM-CH_3 surface. The fact that P adsorbed onto SAM-CH_3 surfaces clearly indicated that hydrophobic interactions, such as van der Waals interactions, were also present for AGUs and may have provided a minor contribution to polysaccharide adsorption onto the hydrophilic surfaces. Likewise, hindered hydrogen bonding and aggregation of cinnamate groups through van der Waals interactions likely enhanced PC adsorption onto cellulose as DS increased.

4.4.8.2 Possible Conformations of PC on Different SAMs

In recognition of the fact that P adsorption onto regenerated cellulose and SAM-OH surfaces was at submonolayer levels, a schematic depiction of how PC molecules may adsorb onto different surfaces was provided in Figure 4.14. In Figure 4.14A, PC003 adsorption onto SAM-OH and cellulose surfaces was depicted as flat (train-like structures), one to two monolayers thick. With increasing DS, intramolecular and intermolecular aggregates of hydrophobic cinnamate esters likely facilitated short, looped structures that enhanced adsorption as depicted in Figure 4.14B for PC006 and PC008 adsorption onto SAM-OH surfaces. For the case of the SAM-CH_3 surfaces (Figure 4.14C), a layer enriched with cinnamate groups probably formed directly at the interface and served as stronger anchoring points for the formation of

relatively long loops stabilized by both intramolecular and intermolecular aggregation of hydrophobic cinnamate groups.

The enhanced adsorption of PC008 onto cellulose likely arose from behavior depicted in Figure 4.14B and C. For SAMs formed from alkanethiols on gold, linear spacings between adjacent SAM molecules of ~ 5 Å, or one hydroxyl group per ~ 25 $Å^2$ have been reported.[169] Likewise, reported values for the length of an AGU were also ~5 Å; however, cross-sectional areas of ~ 60 $Å^2$ per AGU yielded ~ 20 $Å^2$ per hydroxyl group.[243] As a consequence of the stereochemistry of the AGUs, hydroxyl group surface densities between SAM-OH and cellulose surfaces were not as close as indicated by these numbers. For any given AGU on the surface, some of the hydroxyl groups must be oriented back into the film and were thus unavailable for hydrogen bonding with the adsorbate. In essence, part of the cellulose surface was hydrophobic, a factor that likely contributed to the greater adsorption of PC008 onto regenerated cellulose than onto the SAM-OH surface. Hence, some cinnamate groups may have interacted directly with the cellulose surface as depicted in Figure 4.14C for SAM-CH_3 surfaces and with each other in looped structures as depicted in Figure 4.14B and C. While the conformations depicted in Figure 4.14 were speculative, they were consistent with the small RMS surface roughnesses observed by AFM, the thicknesses of the films deduced from SPR experiments, and the probable roles hydrophobes played in the adsorption process.

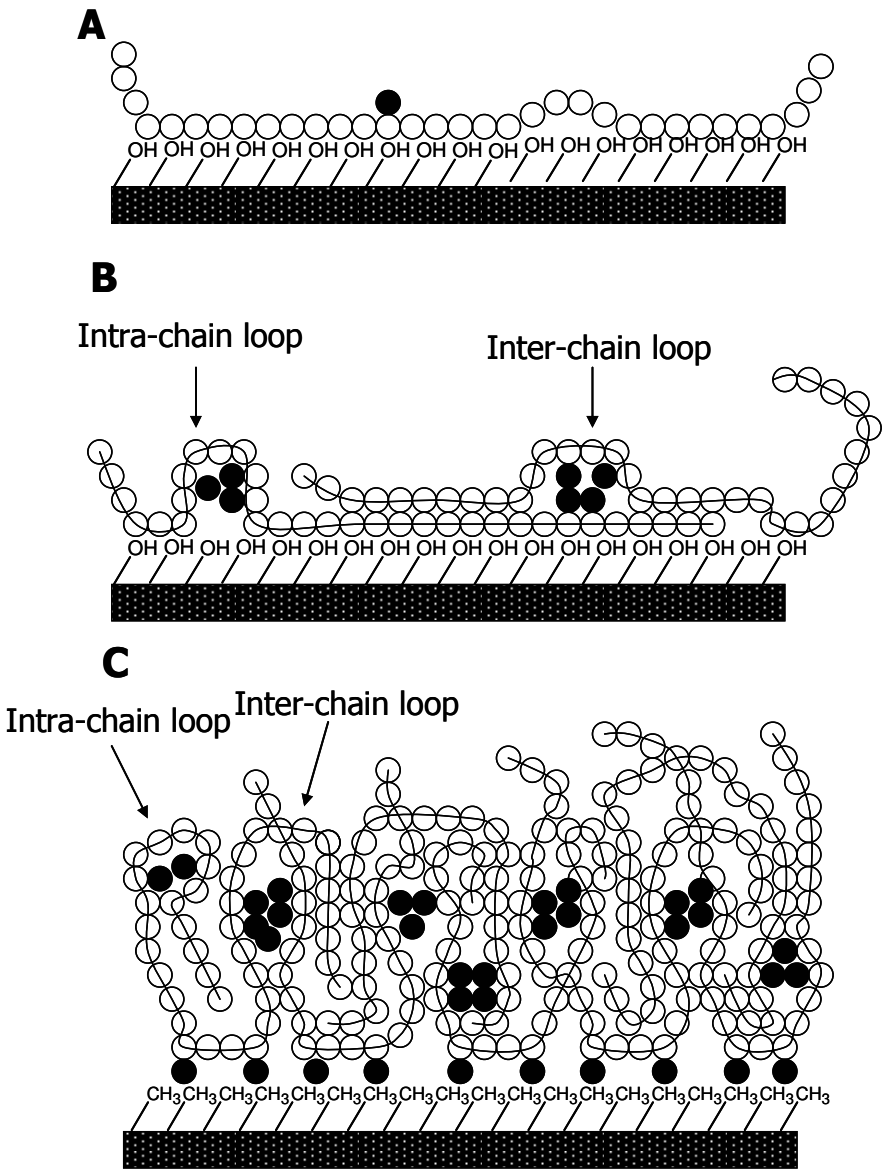

Figure 4.14: Schematic depiction of possible chain conformations for (A) PC003 adsorption onto SAM-OH surfaces, (B) PC006 and PC008 adsorption onto SAM-OH surfaces, and (C) PC008 adsorption onto SAM-CH_3 surfaces. Open circles represent AGUs and filled circles represent cinnamate groups which are attached to a polymer chain.

4.4.8.3 Relationship Between Regenerated and Native Cellulose Surfaces

Until this point, cellulose has been referred to as a model surface. In general, regenerated cellulose hydrolyzed from TMSC has been found largely in the amorphous state. Conversely,

native cellulose is normally composed of both amorphous and crystalline cellulose I (parallel chains) regions.[207] Electron diffraction and reflection absorption infrared spectroscopy (RAIRS) experiments[206] confirmed that the regeneration process used in this study yielded amorphous bulk and film samples, respectively. Furthermore, the model regenerated cellulose surfaces exhibited no features characteristic of crystalline cellulose II (anti-parallel chains) structures. All of these observations were in line with a previous study.[142] Hence, conclusions drawn in this study should be consistent with adsorption onto the amorphous regions of the native cellulose I structure. Future studies will explore the role of surface crystallinity on the adsorption process.

4.5 Conclusions

This study demonstrated that pullulan cinnamates adsorbed onto regenerated cellulose surfaces at levels far greater than pullulan. The resulting layers were uniform, smooth, and the adsorbed amount increased with DS. Similar studies on hydroxyl-terminated self-assembled monolayers showed that hydrogen bonding alone was not the sole driving force for enhanced PC adsorption onto cellulose. Likewise, studies on hydrophobic, methyl-terminated self-assembled monolayers provided insight into how hydrophobic modification enhanced adsorption onto cellulose. These results suggested that the hydrophobic modification of water-soluble polysaccharides was a good strategy for promoting adsorption onto the amorphous regenerated cellulose surfaces. Future work will probe the role crystallinity of the cellulose surface plays in this process and if this strategy is generally applicable to other polysaccharides, especially xylans (hemicelluloses), using other lignin-like hydrophobic substituents. If this approach is general, new classes of surface modifying agents for cellulosic and even synthetic materials could be created from sustainable natural materials.

CHAPTER 5

Adsorption of 2-Hydroxypropyltrimethylammonium Xylan onto Self-assembled Monolayers and Model Cellulose Surfaces

5.1 Abstract

Adsorption of cationic 2-hydroxypropyltrimethylammonium (HPMA) xylans (HPMAXs) with different degrees of substitution (DS) onto self-assembled monolayers (SAMs) and regenerated cellulose surfaces was investigated by surface plasmon resonance (SPR) spectroscopy. Maximal HPMAX adsorption onto carboxyl-terminated SAMs (SAM-COOH) occured at an intermediate HPMA DS of 0.10. This observation was ascribed to relatively flat conformations for adsorbed HPMAX at higher HPMA DS values because of higher linear charge densities. In contrast to SAM-COOH surfaces, there was submonolayer adsorption of any HPMAX onto hydrophilic hydroxyl-terminated SAMs with slightly greater adsorption onto methyl-terminated SAMs (SAM-CH_3). HPMAX adsorption onto regenerated cellulose surfaces was also at submonolayer levels. Unlike the SAM-COOH surfaces, HPMAX adsorption onto SAM-CH_3 surfaces increased as HPMA DS decreased, a correlation which tracked HPMAX solubility in water. These studies showed polysaccharide polyelectrolytes could be prepared where adsorption onto various model surfaces was controlled by electrostatic interactions.

5.2 Introduction

Diminished reserves and price pressures for fossil fuels have created growing urgency for the development of novel bio-based products and innovative technologies. Bio-based materials, made from renewable agricultural and forestry feed stocks, including wood wastes and residues,

grasses, crops, and crop by-products, are required for high volume industrial applications.[244] Cellulosic and lignocellulosic fibers have attracted the greatest interest. Recent results have suggested that lignocellulosic fibers will be a viable alternative to inorganic/mineral based reinforcing fibers in commodity fiber-thermoplastic composite materials.[223] Some of the advantages of these natural fibers relative to traditional reinforcing fibers were low cost, low density, high toughness, acceptable specific strength properties, good thermal properties, ease of separation, enhanced energy recovery, and biodegradability.[245] However, chemical incompatibilities between lignocellulosic fibers and synthetic matrices have yielded poor interfacial stability for natural fiber-thermoplastic composite materials.[222, 223] Surface modification of cellulose fibers with polyelectrolytes has been explored as an attractive option for the creation of better interfaces between cellulose and thermoplastics. In this context, the adsorption of polyelectrolytes onto both hydrophobic surfaces (thermoplastic surfaces) and hydrophilic or charged surfaces (cellulose fibers) has been identified as a crucial factor for better engineered interfaces.

General agreement throughout the chemical literature has identified salt concentration (c_s), surface charge density (σ_0), linear charge density of the polyelectrolyte (τ), and nonelectrostatic interactions between the surface and the polyelectrolyte as the main governing factors for polyelectrolyte adsorption onto surfaces.[106] Some of these factors have been extensively explored. Polyelectrolyte adsorption theories predicted decreased adsorption with increasing salt concentration when electrostatic interactions were the primary reason for adsorption.[55, 107] Van de Steeg et al.[116] defined two regimes for salt-dependent polyelectrolyte adsorption: screening-enhanced adsorption and screening-reduced adsorption. For the screening-reduced adsorption regime, electrostatic attractions between polyelectrolyte chain segments and the surface were

dominant and adsorption decreased as salt concentration increased because the salt screened the electrostatic attraction between the surface and the adsorbate. In contrast, the screening-enhanced adsorption regime was characterized by dominant, nonelectrostatic interactions between the segment and the surface that caused increased adsorption with increased salt concentration because the salt screened electrostatic repulsions between the segments and the surface.[116] A scaling approach for polyelectrolyte adsorption by Dobrynin and Rubinstein[126] predicted a two-dimensional (2D) adsorbed layer formed at low surface charge densities, and a three-dimensional (3D) adsorbed layer occurred at higher surface charge densities. 2D adsorbed layers were caused by the balance between the energy gained through electrostatic attraction between charged monomers and the surface and the loss of confinement entropy that arose from chain localization at low surface charge densities. In contrast, 3D adsorbed layers resulted from the balance of electrostatic attractions between charged monomers and the surface, and short-range monomer-monomer repulsions at high surface charge densities. The crossover between a 2D adsorbed layer and a 3D adsorbed layers occured at $\sigma_e \approx fa^{-2}$ where f was the fraction of charged monomers and "a" was the bond length.[126] For a 2D adsorbed layer, screening enhanced adsorption arose when added salt screened the repulsion between segments and largely overcompensated for the surface charge. At higher salt concentrations, the adsorbed amount was independent of surface charge, depended on the linear charge density of the polyelectrolyte chains, and increased with the square root of the ionic strength. For a 3D adsorbed layer, polyelectrolyte adsorption increased at low salt concentrations (screening-enhanced adsorption) and decreased at higher salt concentrations (screening-reduced adsorption). These competing effects yielded a maximum in the adsorbed amount at intermediate salt concentrations.[99]

Polyelectrolyte adsorption onto model cellulose surfaces has been quantitatively studied with surface plasmon resonance (SPR) spectroscopy,[140] reflectometry,[141] X-ray photoelectron spectroscopy,[246] and the quartz crystal microbalance with dissipation monitoring.[243, 247, 248] Geffroy et al.[141] studied poly(vinylamine) (PVAm) adsorption onto model cellulose surfaces as a function of pH and ionic strength. At pH = 10.6, they observed a maximum in the adsorbed amount which was attributed to a subtle balance between an increased linear charge density of the polymer as pH decreased and increased surface charge density for the cellulose surface as the pH of the system increased. They also observed a decrease in adsorbed amount with increased ionic strength which demonstrated the significance of electrostatic interactions on the adsorption process. Rojas et al.[246] investigated the adsorption of random copolymers of uncharged acrylamide (AM) and positively charged [3-(2-methylpropionamido)propyl] trimethylammonium chloride (MAPTAC) with different linear charge densities onto mica and Langmuir-Blodgett (LB) cellulose surfaces. It was observed that adsorption onto highly negatively charged mica surfaces was considerably greater than onto a nearly uncharged cellulose surface. It was also demonstrated that adsorbed amounts of AM-MAPTAC polyelectrolytes onto cellulose decreased as the linear charge density of the polyelectrolytes increased. Tammelin et al.[247] investigated the adsorption of cationic poly(acrylamide) (C-PAM) and poly(diallydimethyammonium chloride) (PDADMAC) onto LB cellulose surfaces. It was observed that an increase in ionic strength caused increased adsorption onto LB cellulose for polyelectrolytes with higher linear charge densities, whereas increased ionic strength did not have a pronounced effect on the adsorption of polyelectrolytes with lower linear charge densities. Recently, Kontturi et al.[243] investigated the adsorption of cationically modified starch (CS) onto a LB cellulose surface and silica at different ionic strengths. They observed that the adsorption of CS with higher linear charge density

increased as soon as NaCl (1 mM) was added to the system, but did not increase further with additional NaCl (100 mM).

For the study performed here, exploitation of xylans as biopolymer sources for polysaccharide-based polyelectrolytes was considered. Xylans were chosen as they were representative of the most common hemicelluloses found in wood and other plants such as grasses, cereals, and herbs.[37] The parent xylan used for this study was from a hardwood species, birch, where the principal hemicellulose was a glucuronoxylan (GX) with a β-(1→4) linked xylose backbone and 4-*O*-methylglucuronic acid (MeGA) substituents attached at various positions along the polysaccharide chain.[249] Previous studies of birch showed, the GX contained approximately one MeGA linked to the xylan chain per ten xylose residues.[250] As such every xylan used in this study contained ~0.1 MeGA per anhydroxylose unit (AXU) in addition to 2-hydroxypropyltrimethylammonium (HPMA) groups covalently added to the birch xylan (BX) as depicted in Figure 3.8 to form 2-hydroxypropyltrimethylammonium xylans (HPMAXs) with controlled degrees of substitution (DS). This study concentrated on the adsorption of HPMAX with variable HPMA DS onto negatively charged, hydrophilic, and hydrophobic self-assembled monolayers (SAMs), and regenerated cellulose.

5.3 Experimental

HPMAXs were provided by Prof. Thomas Heinze's group at the Friedrich-Schiller-University in Jena, Germany. Refractive index increments and DS of HPMAXs were provided in Section 3.1.2. The procedure for SPR experiments was described in Section 3.2.10.

5.4 Results and Discussion

5.4.1 HPMAX Adsorption onto SAM-COOH Surfaces

Representative SPR data for HPMAX010 adsorption onto a SAM-COOH surface was provided in Figure 5.1. The saw-tooth pattern observed in Figure 5.1 arose from the sequential pattern of sensor exposure to water, analyte solution, water, analyte solution of a higher concentration, water, etc. Extraction of $\Delta\theta_{tot}$ and $\Delta\theta_{irr}$ from the SPR data was systematically depicted in the inset of Figure 5.1. Similar data for other HPMAX samples were provided as Figure 5.2. From Figure 5.1, it was readily apparent that there were no significant differences between $\Delta\theta_{tot}$ and $\Delta\theta_{irr}$ (also provided as Figure 5.3), an indication of completely irreversible adsorption. Analysis of the data in Figure 5.3 to obtain adsorption isotherms revealed that the maximum HPMAX surface concentration on the SAM-COOH surface occurred for an intermediate HPMA DS of 0.10 as shown in Figure 5.4A, and was ~ 3X larger than HPMAX006 and HPMAX034 adsorption onto SAM-COOH surfaces.

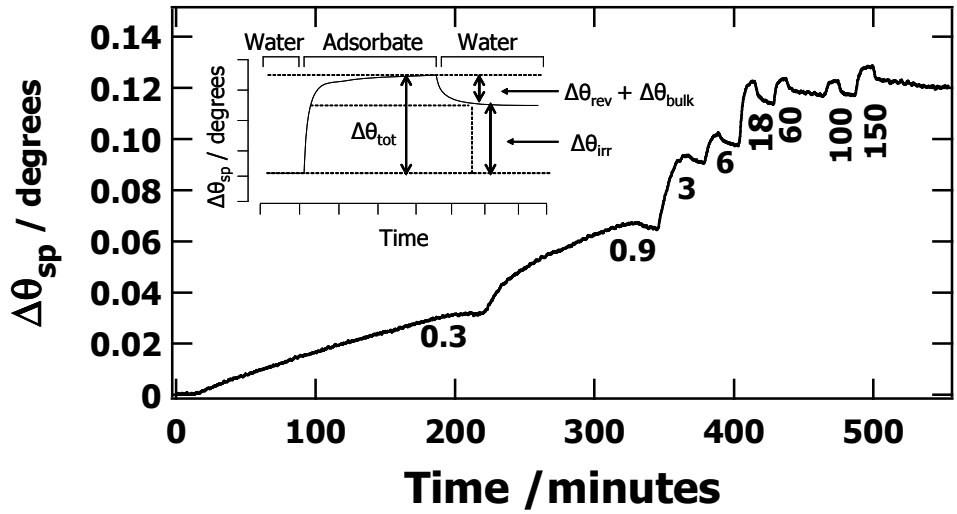

Figure 5.1: Representative SPR data for HPMAX010 adsorption onto a SAM-COOH surface at 20.0 °C. Solution concentrations in $mg \cdot L^{-1}$ correspond to the numbers on the graph. Water was flowed through the SPR instrument before and after each new adsorbate solution. The inset shows a schematic depiction of raw SPR data for the case where water was used to establish a baseline value for $\Delta\theta_{sp}$. A solution containing adsorbate produced a total change in $\Delta\theta_{sp}$ ($\Delta\theta_{tot}$). Switching from adsorbate solution to water eliminated the bulk contribution ($\Delta\theta_{bulk}$), removed reversibly bound adsorbate ($\Delta\theta_{rev}$), and yielded irreversibly bound adsorbate ($\Delta\theta_{irr}$).

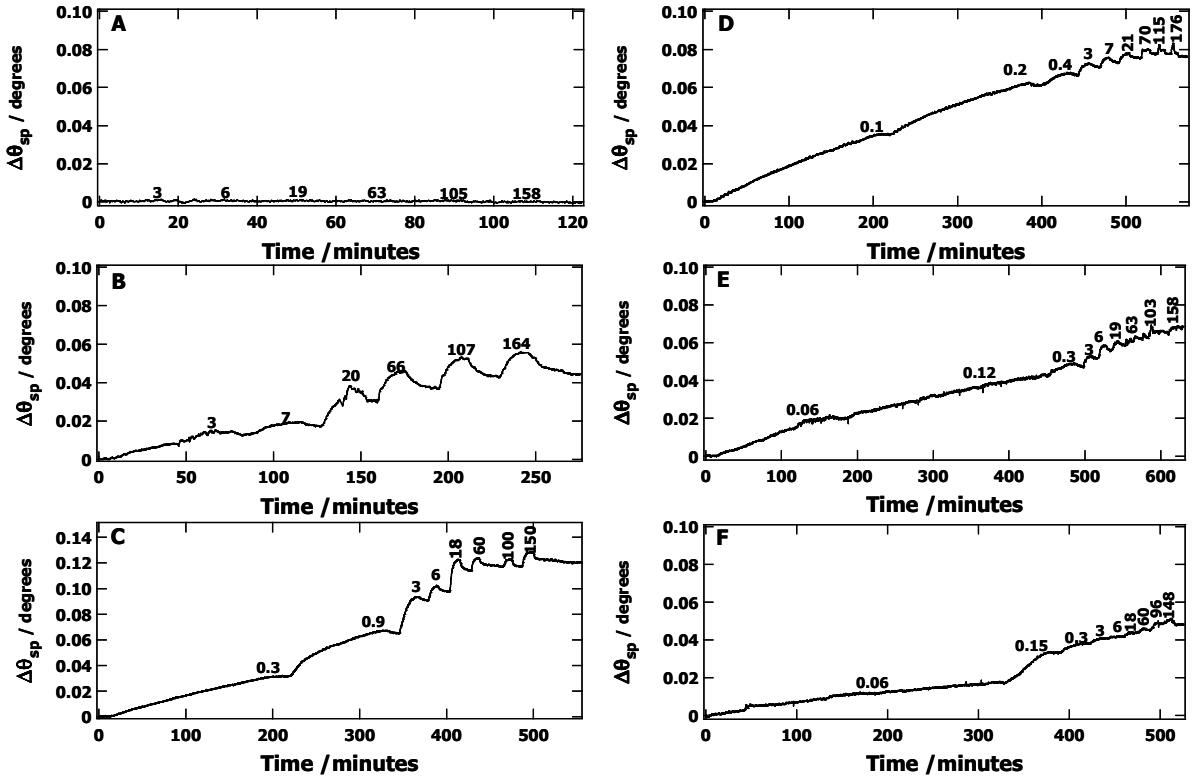

Figure 5.2: Representative SPR data for HPMAX adsorption onto SAM-COOH surfaces at 20.0 °C. Graphs (A) through (F) correspond to BX, HPMAX006, HPMAX010, HPMAX014, HPMAX019, and HPMAX034, respectively. Solution concentrations in $mg \cdot L^{-1}$ correspond to the numbers on (A) through (F). Water was flowed through the SPR instrument before and after each new adsorbate solution.

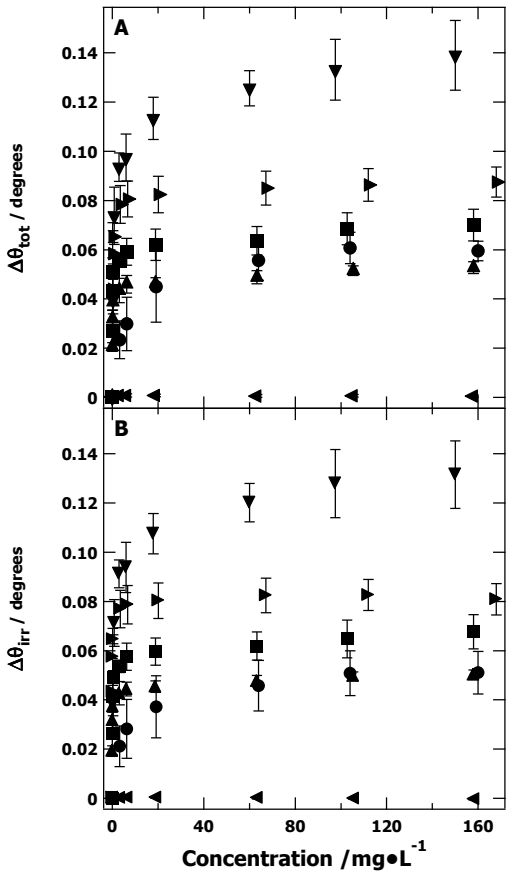

Figure 5.3: (A) $\Delta\theta_{tot}$ and (B) $\Delta\theta_{irr}$ versus concentration for HPMAX adsorption onto SAM-COOH surfaces at 20.0 °C. Symbols correspond to BX (◄), HPMAX006 (●), HPMAX010 (▼), HPMAX014 (►), HPMAX019 (■), and HPMAX034 (▲) with one standard deviation error bars.

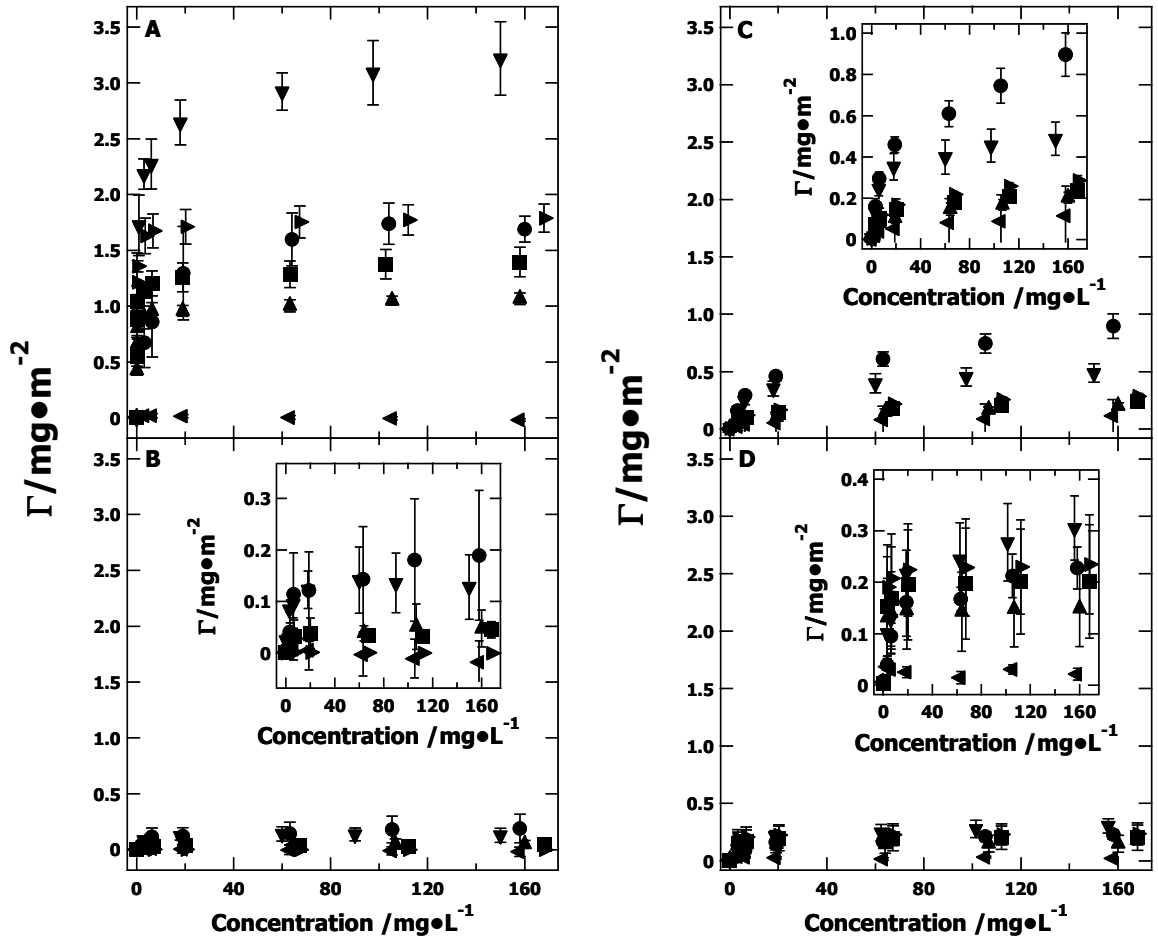

Figure 5.4: Adsorption isotherms for HPMAX adsorption onto (A) SAM-COOH, (B) SAM-OH, (C) SAM-CH_3, and (D) regenerated cellulose surfaces at 20.0 °C. Symbols correspond to BX (◄), HPMAX006 (●), HPMAX010 (▼), HPMAX014 (►), HPMAX019 (■), and HPMAX034 (▲) with one standard deviation error bars. The insets of (B) through (D) simply expand the relevant y-axis range to more clearly show the trend.

5.4.2 HPMAX Adsorption onto SAM-OH, SAM-CH_3, and Regenerated Cellulose Surfaces

The strong dependence for HPMAX adsorption onto SAM-COOH surfaces from water (pH = 5.5) presumably arose from electrostatic interactions between the cationic HPMA substituents and the partially deprotonated, anionic, SAM-COOH surface. This deduction was consistent with the fact that BX suspensions did not adsorb onto the SAM-COOH surfaces

(Figure 5.4A). Further verification of this supposition required the exploration of other potential driving forces. The contributions of other possible molecular factors to the adsorption process were probed through studies of HPMAX adsorption onto SAM-OH, SAM-CH_3, and regenerated cellulose surfaces. Representative raw SPR adsorption data and plots of $\Delta\theta_{tot}$ and $\Delta\theta_{irr}$ for HPMAX adsorption onto SAM-OH surfaces were provided as Figures 5.5 and 5.6, respectively. These data were used to generate the adsorption isotherms provided later in Figure 5.4B. The maximum Γ, ~ 0.2 $mg \cdot m^{-2}$, represented irreversible adsorption and was at least a factor of five smaller than Γ for HPMAX034 adsorption onto the SAM-COOH surface, the lowest maximum Γ for any HPMAX. Hence, hydrogen bonding, alone could not explain the HPMAX adsorption behavior seen with the SAM-COOH surface.

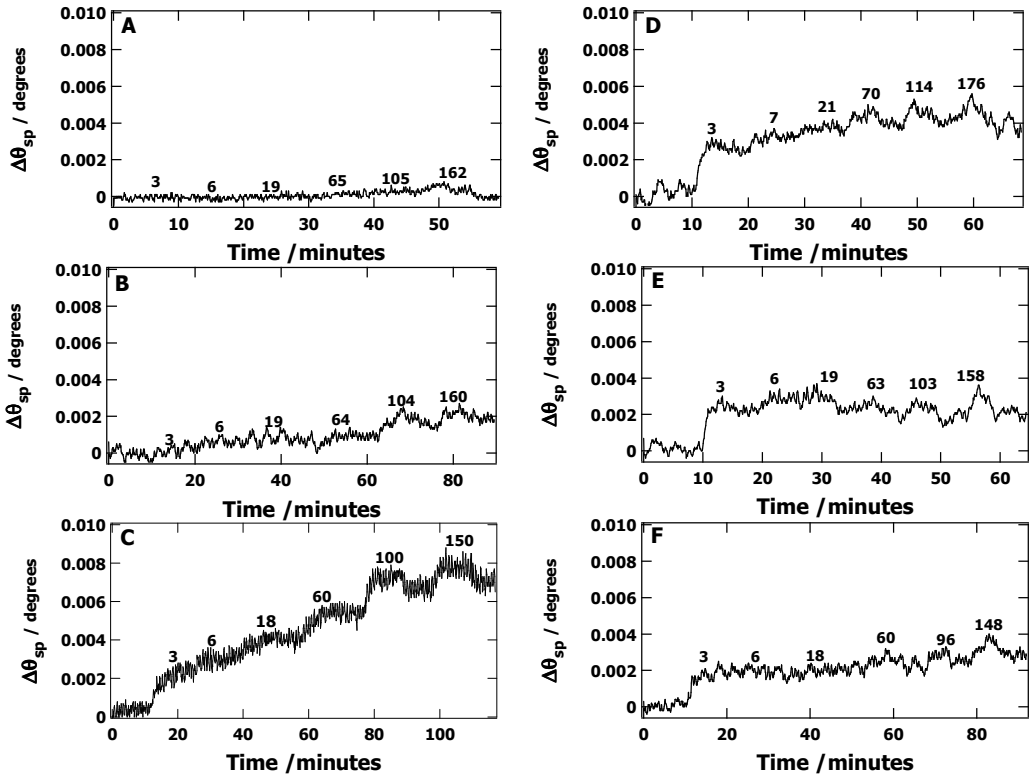

Figure 5.5: Representative SPR data for HPMAX adsorption onto SAM-OH surfaces at 20.0 °C. Graphs (A) through (F) correspond to BX, HPMAX006, HPMAX010, HPMAX014, HPMAX019, and HPMAX034, respectively. Solution concentrations in $mg \cdot L^{-1}$ correspond to the numbers on (A) through (F). Water was flowed through the SPR instrument before and after each new adsorbate solution. Note that the y-axes on the graphs are ~1/10 the range of the corresponding plots in Figure 5.2.

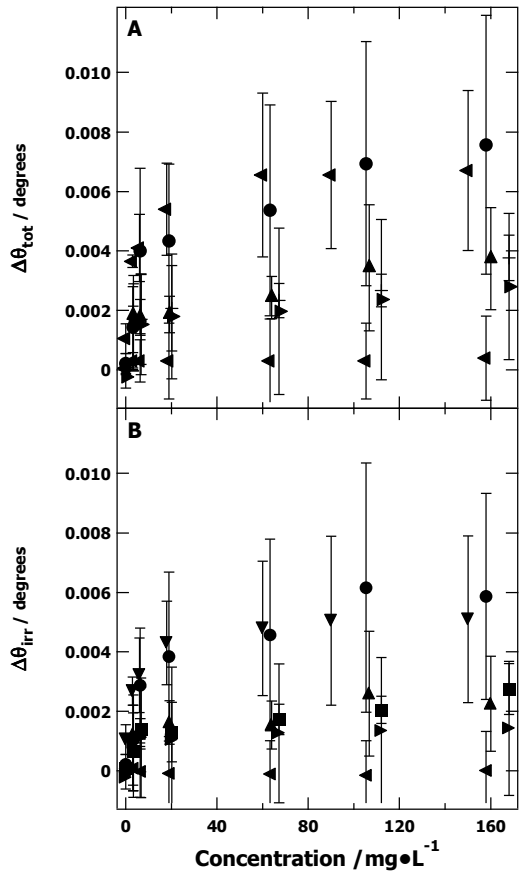

Figure 5.6: (A) $\Delta\theta_{tot}$ and (B) $\Delta\theta_{irr}$ versus concentration for HPMAX adsorption onto SAM-OH surfaces at 20.0 °C. Symbols correspond to BX (◄), HPMAX006 (●), HPMAX010 (▼), HPMAX014 (►), HPMAX019 (■), and HPMAX034 (▲) with one standard deviation error bars.

HPMAX adsorption onto SAM-CH_3 surfaces probed hydrophobic contributions to the adsorption process. Representative raw SPR adsorption data and plots of $\Delta\theta_{tot}$ and $\Delta\theta_{irr}$ for HPMA adsorption onto SAM-CH_3 surfaces were provided as Figures 5.7 and 5.8, respectively. The adsorption isotherms deduced from these data (Figure 5.4C) revealed two important features: First, HPMAX adsorption onto SAM-CH_3 surfaces was significantly smaller than onto SAM-COOH surfaces; and Second, HPMAX adsorption onto SAM-CH_3 surfaces increased

systematically with decreasing DS. The latter trend was very different from Figure 5.4A where a clear adsorption maximum at intermediate HPMA DS was observed. Nonetheless, hydrophobic interactions were clearly not the major contributor to HPMAX adsorption onto SAM-COOH surfaces.

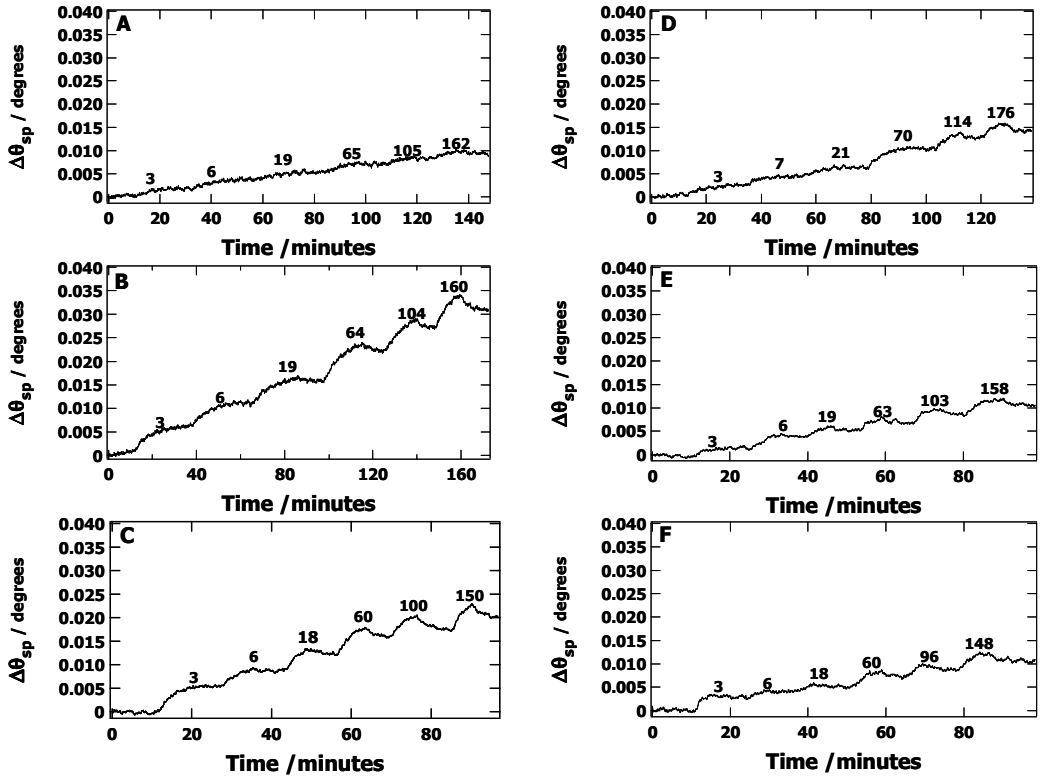

Figure 5.7: Representative SPR data for HPMAX adsorption onto SAM-CH_3 surfaces at 20.0 °C. Graphs (A) through (F) correspond to BX, HPMAX006, HPMAX010, HPMAX014, HPMAX019, and HPMAX034, respectively. Solution concentrations in $mg \cdot L^{-1}$ correspond to the numbers on (A) through (F). Water was flowed through the SPR instrument before and after each new adsorbate solution. Note that the y-axes on the graphs are ~1/3 the range of the corresponding plots in Figure 5.2.

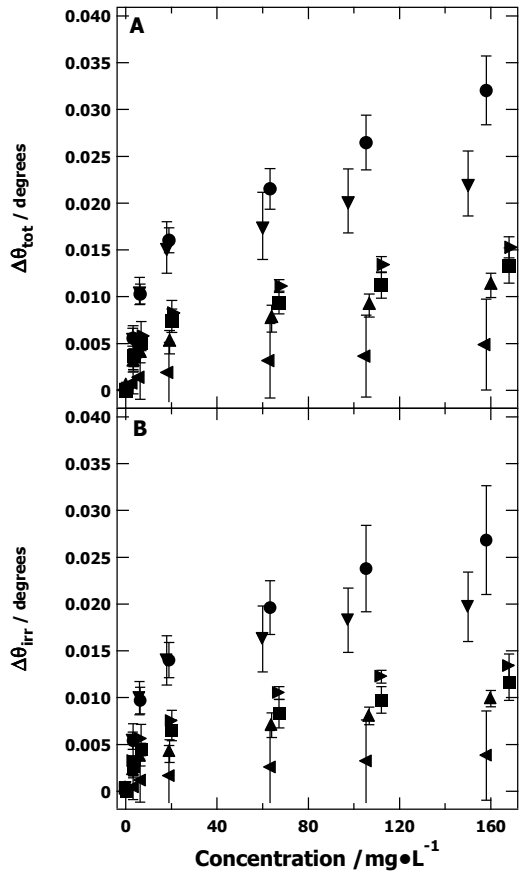

Figure 5.8: (A) $\Delta\theta_{tot}$ and (B) $\Delta\theta_{irr}$ versus concentration for HPMAX adsorption onto SAM-CH_3 surfaces at 20.0 °C. Symbols correspond to BX (◄), HPMAX006 (●), HPMAX010 (▼), HPMAX014 (►), HPMAX019 (■), and HPMAX034 (▲) with one standard deviation error bars.

In nature, interactions between cellulose and hemicelluloses have been recognized as physical in nature.[30, 32, 251] In these systems, specific hydrogen bonding and van der Waals interactions have arisen from stereochemical constraints. Hence, HPMAX adsorption onto a regenerated cellulose surface (one with essentially no surface charge)[137, 252] was also tested. Representative raw SPR data and $\Delta\theta_{tot}$ and $\Delta\theta_{irr}$ data used to generate Figure 5.4D were provided as Figures 5.9 and 5.10, respectively. As seen in Figure 5.4D, the completely irreversible

HPMAX adsorption onto regenerated cellulose was not significantly greater than HPMAX adsorption onto SAM-OH surfaces, and no significant DS dependence was observed.

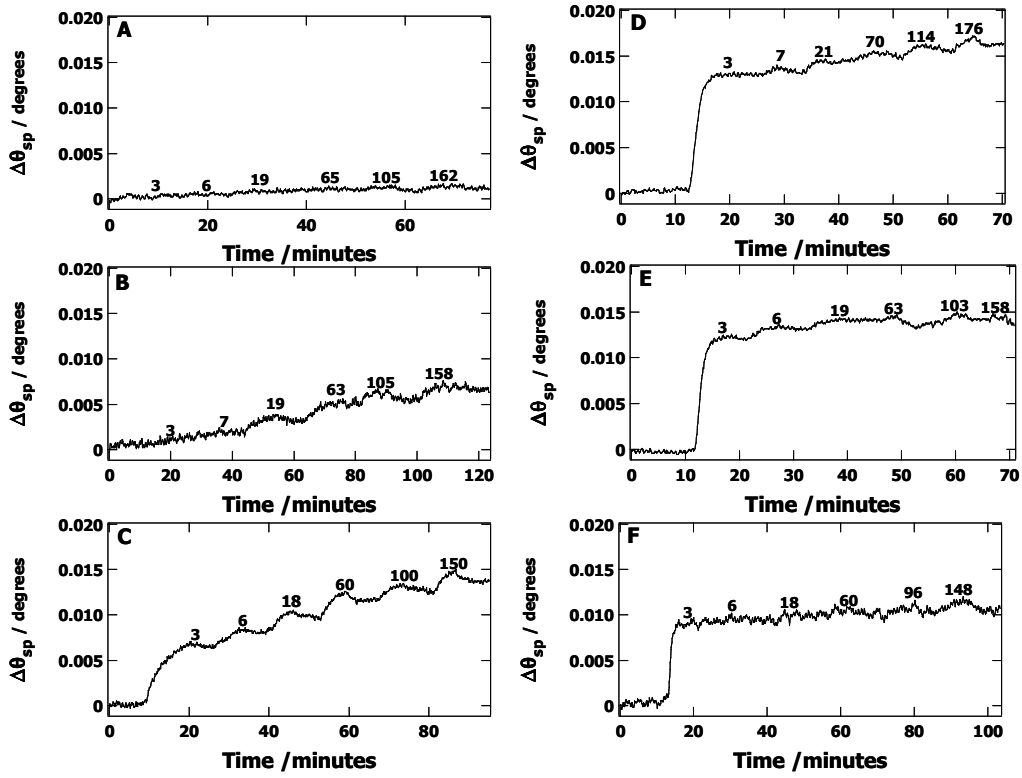

Figure 5.9: Representative SPR data for HPMAX adsorption onto regenerated cellulose derived from spincoated TMSC films at 20.0 °C. Graphs (A) through (F) correspond to BX, HPMAX006, HPMAX010, HPMAX014, HPMAX019, and HPMAX034, respectively. Solution concentrations in $mg \cdot L^{-1}$ correspond to the numbers on (A) through (F). Water was flowed through the SPR instrument before and after each new adsorbate solution. Note that the y-axes on the graphs are ~1/5 the range of the corresponding plots in Figure 5.2.

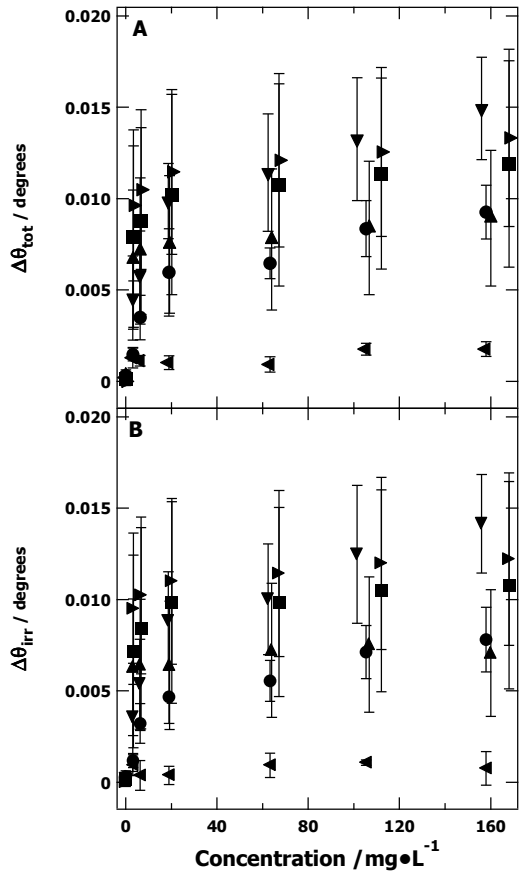

Figure 5.10: (A) $\Delta\theta_{tot}$ and (B) $\Delta\theta_{irr}$ versus concentration for HPMAX adsorption onto regenerated cellulose surfaces at 20.0 °C. Symbols correspond to BX (◄), HPMAX006 (●), HPMAX010 (▼), HPMAX014 (►), HPMAX019 (■), and HPMAX034 (▲) with one standard deviation error bars.

5.4.3 Salt Effects on HPMAX Adsorption

Representative raw SPR data for the adsorption of HPMAX010 and HPMAX034 onto SAM-COOH surfaces at different salt concentrations were provided in Figure 5.11. Each individual experiment was carried out at least three times and the values for $\Delta\theta_{tot}$ for each salt concentration were extracted from the SPR raw data. Adsorption experiments were conducted at polymer concentrations of 100 mg·L^{-1} and 20 mg·L^{-1} for HPMAX010 and HPMAX034, respectively. At these concentrations, adsorption occurred on the plateau of the HPMAX

adsorption isotherms for SAM-COOH surfaces in polymer solutions without added salt. In general, adsorption equilibrium was attained after 10 minutes for HPMAX010 and HPMAX034 adsorption at all salt concentrations studied with the exception of HPMAX034 adsorption onto SAM-COOH surfaces in the presence of 100 mM NaCl. For the adsorption of HPMAX034 from 100 mM NaCl solutions, longer equilibration times were observed and $\Delta\theta_{sp}$ values increased relative to lower salt concentrations. This observation was indicative of salting-out of the polyelectrolyte, a common phenomenon for polyelectrolytes at higher salt concentrations.[105]

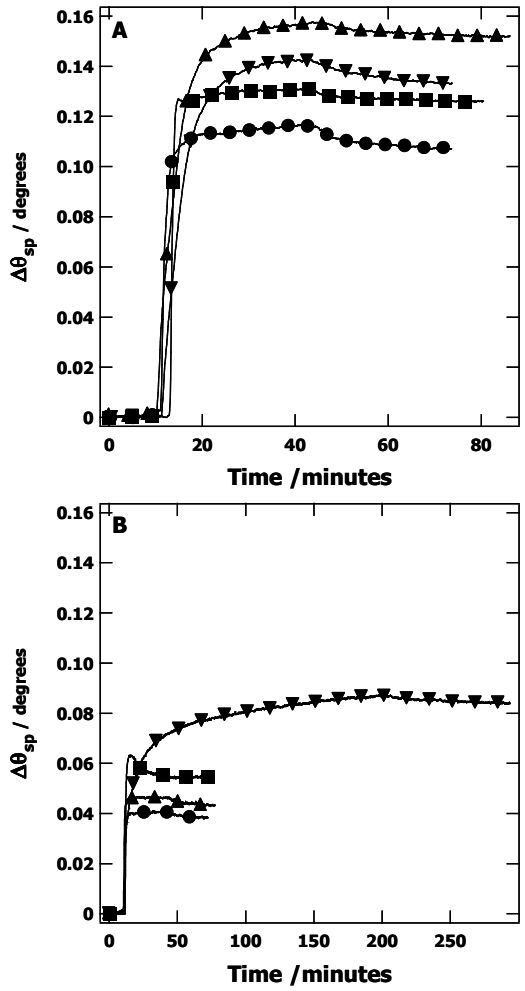

Figure 5.11: Representative SPR data for HPMAX adsorption onto SAM-COOH surfaces from solutions with different salt concentrations at 20.0 °C. Graphs (A) and (B) correspond to HPMAX010 and HPMAX034, respectively. HPMAX solution concentrations were 100 $mg \cdot L^{-1}$ and 20 $mg \cdot L^{-1}$ for HPMAX010 and HPMAX034, respectively. Symbols on (A) and (B) correspond to different salt concentrations, (■) 0 M NaCl, (●) 1 mM NaCl, (▲) 10 mM NaCl, and (▼) 100 mM NaCl.

5.4.4 Discussion

Maximum surface excess (Γ_{max}) values obtained as a function of HPMA DS from Figure 5.4 for the adsorption of HPMAX onto SAM-COOH surfaces were replotted in Figure 5.12.

There was a clear maximum in Γ_{max} at HPMA DS = 0.10 for HPMAX adsorption onto the SAM-COOH surfaces. Several theories have predicted the existence of an adsorption maximum as a function of linear charge density. Hesselink et al.[107] predicted an adsorption maximum at $\tau \sim 0.10$ charged groups per repeat unit for polyelectrolyte adsorption at a salt concentration of 100 mM. Van de Steeg et al.[116] theoretically predicted this maximum at $\tau \sim 0.015$. These theoretical treatments showed the maximum shifted to lower τ values and became sharper as salt concentration decreased. Experimentally, a maximum was observed at $\tau \sim 0.01$ for the adsorption of copolymers of acrylamide and an acrylate of trimethylaminoethylchloride onto silica surfaces[119] and copolymers of acrylamide and an acrylate with a quarternary ammonium group onto montmorillonite (clay)[122] under low electrolyte conditions (no added electrolyte). The discrepancy between the position of the maximum in Figure 5.12 ($\tau \sim 0.10$ with respect to HPMA) and previous studies ($\tau \sim 0.01$) under low electrolyte conditions likely reflected the presence of negatively charged MeGA groups on the xylan backbone. Polyelectrolyte titrations[253] revealed HPMAX006 in the pH range of 6 to 10 was negative, whereas HPMAX with higher DS were positively charged over the same pH range (Figure 5.13). The MeGA groups lowered the effective linear charge density of the polyelectrolyte and shifted the observed maximum to a higher apparent DS value.

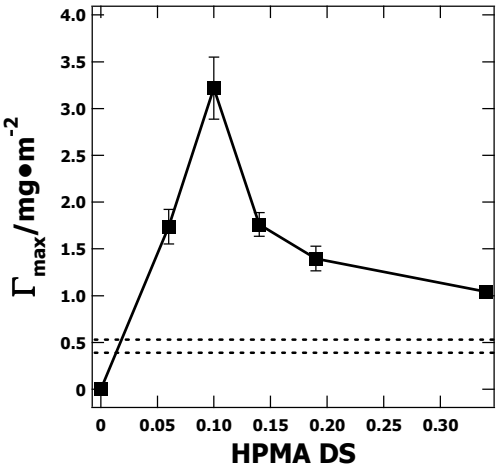

Figure 5.12: Γ_{max} versus HPMA DS for the adsorption of HPMAXs onto SAM-COOH surfaces at 20.0 °C. The dashed horizontal lines correspond to the approximate values for a flat unsubstituted AXU (lower limit) and the fully substituted HPMAX034 (upper limit).[242]

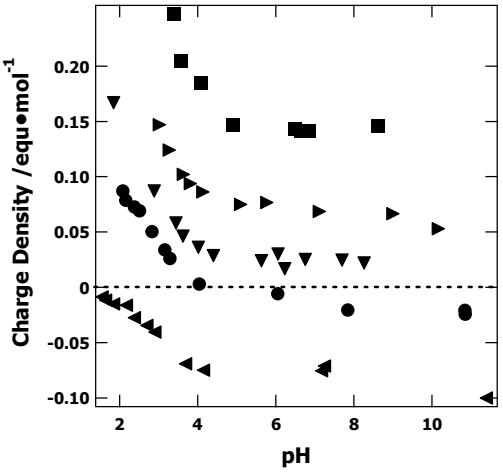

Figure 5.13: The total surface charge of HPMAX with various HPMA DS measured by polyelectrolyte titration using polystyrenesulfonate or polydiallyldimethylammonium chloride as the simplex building components. Symbols correspond to (◄) BX, (●) HPMAX006, (▼) HPMAX010, (►) HPMAX014, and (■) HPMAX019. The horizontal dashed line highlights charge neutrality.

In the context of the theory of Dobrynin and Rubinstein,[126] the profile observed in Figure 5.12 could be interpreted as a 2D layer at high DS and a 3D layer in the vicinity of the adsorption maximum. As seen in Figure 5.12, the Γ_{max} value for HPMAX034 was only ~2X the value of a flat substituted AXU. Further support for this conclusion was provided in Figure 5.14 where Γ_{max} values for HPMAX034 and HPMAX010 were plotted as a function of [NaCl]. For a 2D layer (HPMAX034 adsorption onto SAM-COOH surfaces), an increase in adsorbed amount (~2X) was consistent with theoretical predictions.

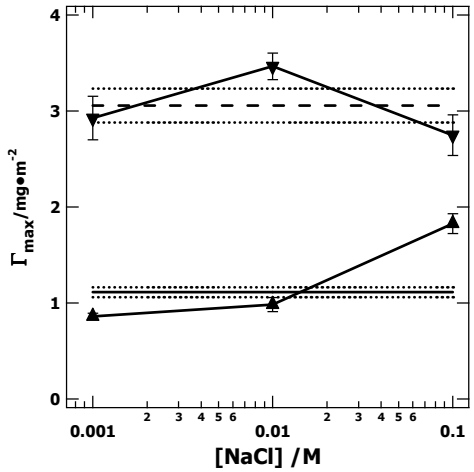

Figure 5.14: Γ_{max} versus [NaCl] for HPMAX010 and HPMAX034 adsorption onto SAM-COOH surfaces at 20.0 °C. The solution concentrations of HPMAX010 and HPMAX034 were 100 $mg \cdot L^{-1}$ and 20 $mg \cdot L^{-1}$, respectively. The graph has a semi-logarithmic scale. Symbols correspond to HPMAX010 (▼) and HPMAX034 (▲) with one standard deviation error bars. The dashed line and solid line represent HPMAX010 and HPMAX034 adsorption under no added salt conditions with one standard deviation error bars (dotted lines), respectively.

Another interesting feature of Figure 5.12 was the strong correlation between the observed trend, and a similar trend for paper strength observed when HPMAX was used as a papermaking additive (Figure 5.15 and 5.16). Most pulping processes have led to the introduction of negative

charges (carboxylates) onto the cellulose fibers. As a consequence, rapid strength decreases have been observed upon the exposure of untreated paper to water. The addition of wet-strength chemicals has shown that paper strength losses could be slowed with a resultant, temporary wet paper strength.[254] Exposure of birch sulfate pulp to aqueous HPMAX with subsequent tensile testing of fabricated hand sheets, revealed tensile indices (Figure 5.15) that depended upon HPMA DS. A plot of maximum tensile index, obtained at HPMAX concentrations of 0.8 g HPMAX/kg birch sulfate pulp as a function of HPMA DS showed a maximum for HPMAX010, just like HPMAX adsorption onto SAM-COOH surfaces (Figure 5.16). In essence, the negatively charged SAM-COOH surface was a reasonable model for the negatively charged birch sulfate pulp.

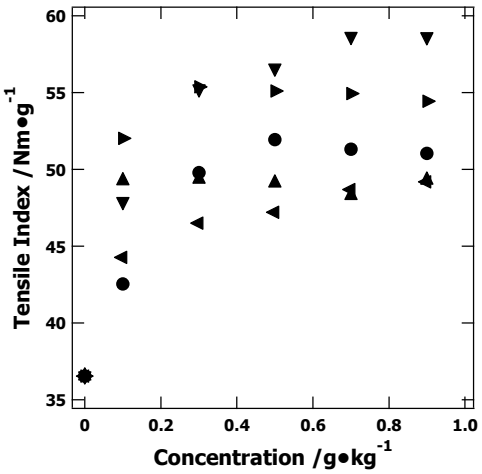

Figure 5.15: Tensile strength of birch sulfate pulp after adding BX and HPMAXs with various DS values. Symbols correspond to (◀) BX, (●) HPMAX006, (▼) HPMAX010, (▶) HPMAX014, and (■) HPMAX019.

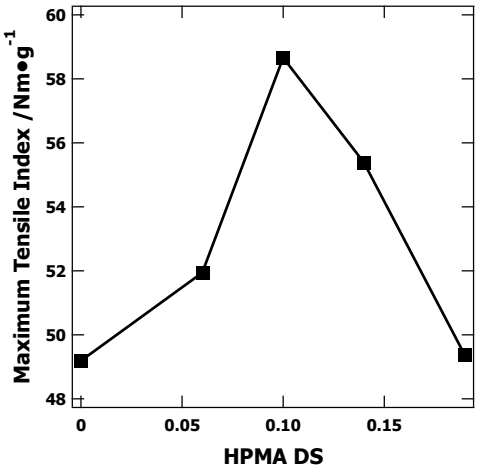

Figure 5.16: Maximum tensile index versus HPMA DS from Figure 5.15.

Electrostatic interactions may have also contributed to the behavior observed for HPMAX adsorption onto regenerated cellulose and SAM-CH_3 surfaces. As shown in Figure 5.4, HPMAX adsorption onto regenerated cellulose was comparable to adsorption onto SAM-OH surfaces and was much smaller than adsorption onto SAM-COOH surfaces. This observation was consistent with two important factors. First, surface force apparatus (SFA) measurements showed that regenerated cellulose obtained from Langmuir-Blodgett films had very low surface charge densities (~ 460 nm^2 per charge),[252] in contrast to carboxyl densities for SAM-COOH films (~0.25 nm^2 per carboxyl). While bulk 11-mercaptoundecanoic acid has a pK_a of 4.75,[255] titrations by chemical force microscopy[256] provided an estimate of a surface pK_a of ~ 8. As such, partial deprotonation of the SAM-COOH could be expected in water (pH ~ 5.5). Moreover, experiments performed in citrate buffer (ionic strength, I = 0.02) at pH = 3 showed adsorption could be reduced to levels comparable to regenerated cellulose, while experiments performed in phosphate buffer (I = 0.03) at pH = 8 showed increased adsorption (Figure 5.17). As such, the SAM-OH and regenerated cellulose surfaces could be regarded as uncharged. Second, the relatively small surface charge densities of the regenerated cellulose surfaces meant that

accumulation of HPMAX at the surface was unfavorable because of electrostatic repulsion between segments on HPMAX. This result was also observed for the adsorption of synthetic polyelectrolytes onto regenerated cellulose by Rojas et al.[246] In those X-ray photoelectron spectroscopy studies, Γ values for cationic polyelectrolytes adsorbed onto regenerated cellulose were quantitatively consistent with SPR results in Figure 5.4D for HPMAX.

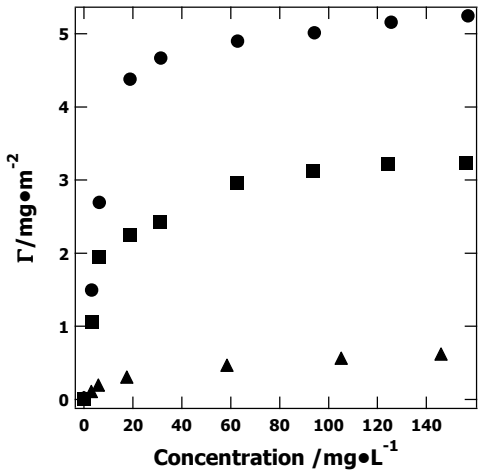

Figure 5.17: Adsorption isotherms for HPMAX010 adsorption onto SAM-COOH surfaces at 20.0 °C at three different pH values. Symbols correspond to (▲) acetate buffer (I = 0.02) at pH = 3, (■) water (pH = 5.5), and (●) citrate buffer (I = 0.03) at pH = 8.

HPMAX adsorption onto SAM-CH_3 surfaces increased as HPMA DS decreased. Previously, Nephelometric turbidity unit (NTU) results for 1 wt% aqueous solutions of HPMAX suggested that as DS increased, HPMAX solubility in water increased.[203] Therefore, Γ for HPMAX adsorption onto SAM-CH_3 surfaces was correlated with aqueous solubility. As electrostatic interactions between HPMA polymers and the hydrophobic SAM-CH_3 surfaces were insignificant, non-electrostatic interactions (e.g. van der Waals) were important for the adsorption process. However, like HPMA adsorption onto the regenerated cellulose surface,

electrostatic repulsions between cationic polymer segments adsorbed on the surface contributed to the trend of smaller Γ as HPMA DS increased.

5.5 Conclusions

Cationization of GX from birch produced a series of cationic xylans which exhibited an adsorption maximum on SAM-COOH surfaces at intermediate DS. The adsorbed layer in the vicinity of the adsorption maximum was consistent with a 3D layer, whereas higher linear charge densities for the polyelectrolyte led to 2D layers. These results were qualitatively consistent with scaling theories. As such, these materials should be compatible with layer-by-layer assembly to create complex lignocellulosic nanocomposites with controlled layer thicknesses. Moreover, the adsorption of HPMAX onto SAM-COOH surfaces was strongly correlated with tensile index studies of HPMAX as a paper additive. Future studies will probe this correlation further with model cellulose surfaces containing surface charge.

CHAPTER 6

Hydroxypropyl Xylan Self-Assembly at Air/Water and Water/Cellulose Interfaces

This chapter has been accepted for publication in an ACS Symposium Series Book: "Hydroxypropyl Xylan Self-Assembly at Air/Water and Water/Cellulose Interfaces," **A. Kaya**, D. A. Drazenovich, W. G. Glasser, T. Heinze, and A. R. Esker, In A.C.S. Symposium Series No. 1019, Model Cellulosic Surfaces, Maren Roman, Ed., 2009, (Accepted).

6.1 Abstract

Hydroxypropylation of polysaccharides is one strategy for enhancing aqueous solubility. The degree of hydroxypropyl substitution can be controlled through the pH of the hydroxypropylation reaction. Surface tension measurements of aqueous solutions of hydroxypropyl xylan (HPX), synthesized from barley husk xylans, by the Wilhelmy plate technique show that surface tension changes ($\Delta\gamma = \gamma_{water} - \gamma_{HPX(aq)}$) increase and critical aggregation concentrations generally decrease with increasing degree of substitution. Hence, even though hydroxypropyl substitution is necessary to induce aqueous solubility, excessive hydroxypropylation promotes aggregation in water. While surface tension studies reveal HPX affinity for the air/water interface, surface plasmon resonance spectroscopy studies indicate that HPXs do not adsorb significantly onto model regenerated cellulose surfaces (submonolayer coverage). Likewise, the HPXs do not show significant adsorption onto hydroxyl-terminated self-assembled monolayers of 11-mercapto-1-undecanol (SAM-OH). In contrast, HPX does

adsorb (~monolayer coverage) onto methyl-terminated self-assembled monolayers of 1-dodecanethiol (SAM-CH_3). These results show hydroxypropylation is a sound approach for creating soluble xylan derivatives, suitable for further chemical modification.

6.2 Introduction

Cellulose is one of the most important natural polymers and is used extensively in the textile and paper industries.[257] In nature, cellulose is located in the core of plant cell walls[258] and is associated with hemicellulose and lignin in a hierarchial (composite) superstructure.[6] Hemicelluloses, which serve as a matrix for the cellulose superstructure, are lower molar mass polysaccharides containing short side chains.[1] These polysaccharides consist of various five (D-xylose, L-arabinose) and six carbon (D-glucose, D-galactose, D-mannose etc.) sugars.[30] Xylans are the most common hemicelluloses and are considered to be the second most abundant biopolymer in land plants.[37] Structurally, xylans are a class of heteropolysaccharides consisting of poly(anhydroxylose) with varying degrees of 4-O methyl glucuronic acid, acetyl groups, and anhydroarabinose substituents depending on the source and isolation procedures used to obtain the xylan.[259] During the past several years, the need for effective biomass utilization has renewed interest in the exploitation of xylans as sources of biopolymers. This interest is aided by the fact that xylans are readily available as organic wastes from renewable forest and agricultural residues, such as wood meal and shavings, stems, stalks, hulls, cobs, and husks.[260] Even though the isolation of xylans from biomass is relatively easy, the potential application of xylans has not yet been completely realized.[204, 260-262] Possible reasons for the lack of xylan utilization as a material stream include a shortage of high molar mass xylans on an industrial scale,[261]

heterogeneity of xylan structures within even a single plant,[260] and the partial degradation of hemicelluloses during pulping processes.[263]

Another complication hindering widespread use of xylans is that they are usually difficult to dissolve in aqueous media and aprotic solvents even when they are isolated by aqueous extraction. Hence, investigations of xylan solution properties and molecular weight determinations are difficult.[264] The substitution of a xylan's hydroxyl groups by alkoxy or acetoxy groups enhances solubility in water and/or organic solvents.[204] Therefore, chemical modification of xylans provides one avenue to make soluble xylans for molecular weight determinations and producing materials with interesting physical properties.[204, 265-269] Glaudemans and Timmel prepared xylan acetate that was completely soluble in chloroform and chloroform–ethanol mixtures. These polymers had a degree of polymerization of ~200.[265] In addition to xylan acetates, other esters of xylans, such as benzoate, caprate, laurate, myristate, and palmitate have been synthesized.[266] In another study, xylans fully substituted with carbamate groups showed thermoplastic behavior at high temperatures.[267] Likewise, Jain et al. prepared water-soluble hydroxypropyl xylans and acetoxypropyl xylans that showed thermoplastic behavior and solubility in most organic solvents.[204] Trimethylammonium-2-hydroxypropyl xylan prepared from beechwood and corn cob xylan showed promise as a papermaking additive by improving the strength of bleached hardwood kraft pulp and unbleached thermomechanical pulp, and by increasing the retention of fiber fines.[268, 269]

The enhancement of pulp properties by some xylan derivatives provides strong incentive for studying xylan self-assembly onto model cellulose and cellulose fiber surfaces. Mora et al. investigated xylan retention on cellulose fibers and concluded that the driving force for xylan aggregate sorption and retention on cellulose fibers was hydrogen bonding between cellulose

fibers and the xylans.[52] Henrikkson et al. also invoked hydrogen bonding along with changes in colloidal stability to explain the adsorption behavior of autoclaved xylans onto cellulose fibers at elevated temperatures under alkaline conditions.[53] In another study, it was observed that commercial birch xylan adsorbed slowly and irreversibly onto model cellulose surfaces at pH = 10.[270] However, it was argued that the driving force for adsorption was a combination of weak van der Waals attractions and an entropically favorable release of solvent molecules when the polymer chains adsorbed. Recently, Esker et al. have shown that cationic and hydrophobic modification of xylan enhances xylan adsorption onto regenerated cellulose films prepared by the Langmuir–Blodgett technique.[51] This result demonstrates that the hydrophobic forces and electrostatic interactions also influence xylan self-assembly onto cellulose surfaces.

In this study, the adsorption of hydroxypropyl xylans (HPXs) onto model surfaces is studied as a function of the degree of hydroxypropyl (HP) substitution (DS). The source of the "parent" xylans for the HPX derivatives is barley husks (*Hordeum* spp.)[204] HPX self-assembly at the air/water interface is probed through the Wilhelmy plate technique, whereas surface plasmon resonance (SPR) spectroscopy studies allow quantification of HPX adsorption onto regenerated cellulose, and self-assembled monolayers (SAMs) of 11-mercaptoundecanol (SAM-OH) and 1-dodecanethiol (SAM-CH_3) on gold substrates. These studies provide insight into molecular factors influencing HPX self-assembly at surfaces and potential use of further-derivatized water-soluble HPX derivatives to modify surfaces and interfaces.

6.3 Experimental

HPX samples were provided by Prof. Wolfgang Glasser's group at Virginia Tech. Procedures for surface tension measurements and SPR experiments were described in Sections 3.2.5 and 3.2.10, respectively.

6.4 Results and Discussion

6.4.1 HPX Characterization

In addition to the properties of the HPX samples reported elsewhere,[204] the DSs of the specific HPX samples used in this study were deduced from ^{1}H NMR studies by preparing chloroform-soluble acetoxypropyl xylan (APX) derivatives. Figure 6.1 shows ^{1}H NMR spectra of the four APX derivatives. The DSs for the HPX derivatives were determined by assuming that there were only two available hydroxyl groups for derivatization in each xylose unit. Furthermore, assuming complete acetylation and the addition of only a single HP unit at any given xylose hydroxyl group yields

$$\mathrm{DS} = \frac{\left(\text{Integral of the HP } -\mathrm{CH_3} \text{ peak at } \delta \approx 1.2 \text{ ppm}\right)}{\left(\text{Integral of the acetyl } -\mathrm{CH_3} \text{ peak at } \delta \approx 2.0 \text{ ppm}\right)} \times 2 \tag{6.1}$$

DS values are summarized in Table 6.1. The data are consistent with the general trend of DS increasing with the pH of the hydroxypropylation reaction.

In addition to ^{1}H NMR, one additional bulk solution characterization technique was carried out on the HPX derivatives. Differential refractometer studies were performed in water to determine the refractive index increment (dn/dc) at a wavelength of 690 nm. These values, necessary for analyzing SPR results, are also summarized in Table 6.1. As seen in the table, dn/dc in water is independent of DS. Additionally, the values are assumed to be relatively independent of wavelength between 690 nm and 780 nm, the wavelength for SPR experiments.

Table 6.1: Selected properties of HPX derivatives.

HPX Acronym	HP DS[a]	dn/dc[b] $mL \cdot g^{-1}$	CAC $mg \cdot L^{-1}$	$\Delta\gamma_{max}$ $mN \cdot m^{-1}$	Γ_{max}[c] $\mu mol \cdot m^{-2}$
HPX120	0.37	0.128 ± 0.001	~ 90	~3	~ 0.8
HPX125	0.88	0.128 ± 0.001	~ 8	~9	~ 1.5
HPX127	1.69	0.128 ± 0.001	~ 20	~19	~ 11
HPX130	1.54	0.125 ± 0.002	~ 4	~18	~ 6

a. DS from ^{1}H NMR of acetylated HPXs.
b. Water at 20.0 °C and a wavelength of 690 nm.
c. From Eqn. 6.2.

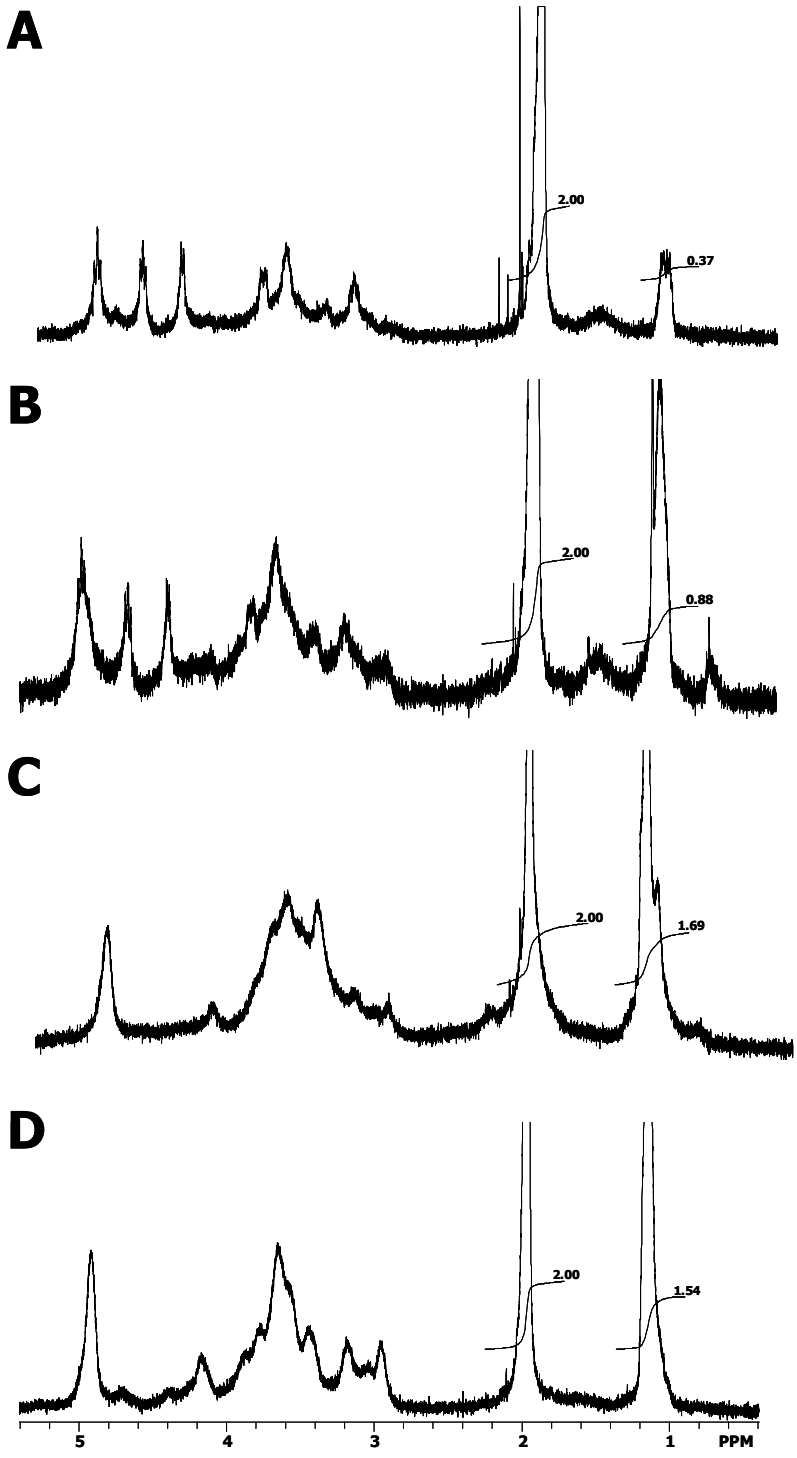

Figure 6.1: [1]H NMR spectra of acetylated HPX derivatives. Spectra A through D correspond to acetylated versions of HPX120, HPX125, HPX127, and HPX130, respectively.

6.4.2 Surface Tension of Aqueous HPX Solutions

Gibbs derived an expression for the surface excess of a solute at constant temperature and pressure at an air/liquid interface:[60]

$$\Gamma = -\frac{1}{RT}\left(\frac{\partial\gamma}{\partial \ln a}\right)_{T,p} \approx -\frac{1}{RT}\left(\frac{\partial\gamma}{\partial \ln c}\right)_{T,p} \tag{6.2}$$

where R is the gas constant, γ is the surface tension, and a and c are the activity and concentration of the solute in solution, respectively. Hence, Γ at the air/water interface can be estimated from measurements of γ as a function of c. Additionally, γ–c plots which show drops in γ and a concentration invariant γ at high c can be used to estimate critical micelle concentrations (CMCs) of surfactants. Estimates of the CMC are generally made by extrapolating the sharply decreasing γ region and plateau regions to a common intercept as done in Figures 6.2 and 6.3. The sharpness of the transition increases with aggregation number. For random coil polymers, aggregation numbers are small (as small as 1–2 polymer chains) and aggregates are irregularly shaped leading to broad transitions. As a consequence, the concentration of the transition is more appropriately termed a critical aggregation concentration (CAC).

Several points in Figures 6.2 and 6.3 are worth noting. First, HPX with the lowest DS (HPX120) has the highest CAC, ~90 mg·L–1, and the smallest overall change in surface tension, $\Delta\gamma \approx 2.9$ mN·m–1. As DS increases, there is a shift to smaller CAC values, and Δγ increases with DS. These values are summarized in Table 6.1. Similar estimates of the CAC are obtained for plots of γ vs. ln c. Second, Γ calculated from Eqn. 6.2 (insets of Figures 6.2 and 6.3) increases with DS. Maximum values (Γ_{max}) are also provided in Table 6.1.

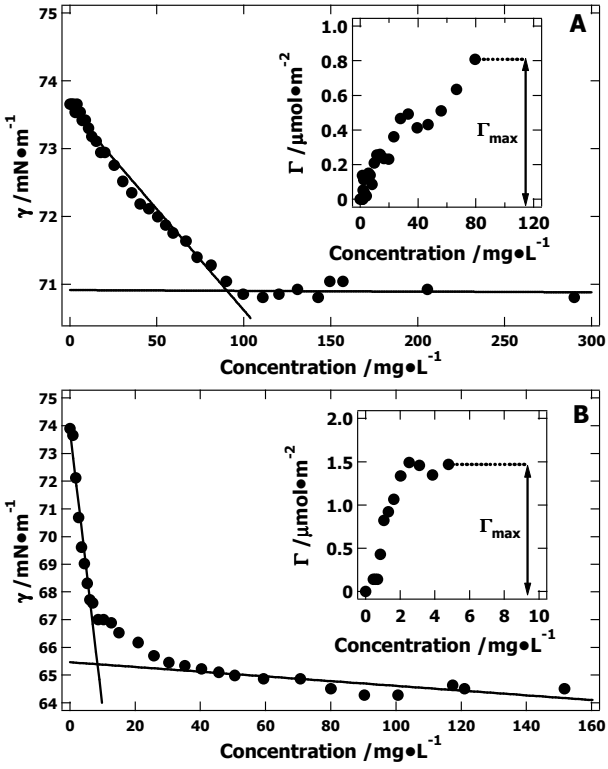

Figure 6.2: γ–c curves for HPX derivatives at the air/water interface at T = 20.0 °C. Graphs A and B correspond to HPX120 and HPX125, respectively. The solid lines provide estimates of the CAC. The insets provide estimates of Γ–c deduced from Eqn. 6.2.

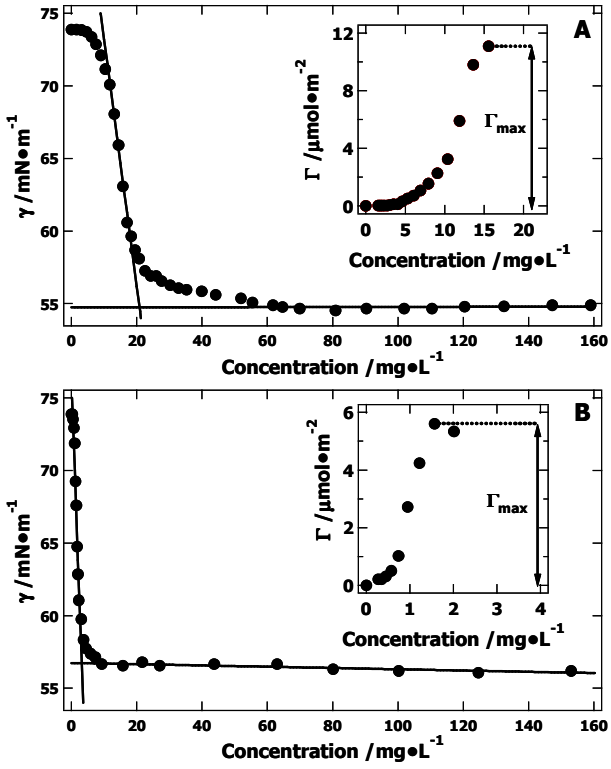

Figure 6.3: γ–c curves for HPX derivatives at the air/water interface at T = 20.0 °C. Graphs A and B correspond to HPX127 and HPX130, respectively. The solid lines provide estimates of the CAC. The insets provide estimates of Γ–c deduced from Eqn. 6.2.

On the basis of the data in Figures 6.2 and 6.3, it can be concluded that even though hydroxypropylation enhances polysaccharide aqueous solubility and dispersion by breaking up hydrogen bonding, the HP groups enhance the amphiphilic character of the xylan. Similar behavior is seen in hydroxypropyl cellulose (HPC) where $\Delta\gamma \approx 28$ mN·m^{-1}.[271] The principle differences between xylan and cellulose are two vs. three hydroxyl groups available for hydroxypropylation, respectively, and a more rigid backbone structure for cellulose. It is also interesting to consider the observed behavior for the HPX derivatives relative to ethylene oxide–propylene oxide copolymers. Block copolymers (Pluronics) show that propylene oxide units

enhance the hydrophobic character of the copolymer. These surfactants show increasing $\Delta\gamma$ and decreasing CACs with increasing propylene oxide content,[272-274] ultimately leading to water insoluble surfactants.[272] Similar effects are believed to be the cause for the enhancement of HPX surface activity at the air/water interface with increasing DS. As we will show shortly, HPX derivatives have stronger affinity for model hydrophobic surfaces than for cellulose and other hydrophilic model surfaces.

6.4.3 Adsorption onto Regenerated Cellulose and SAM-OH Surfaces

Figure 6.4 and 6.5 show representative SPR raw data for HPX adsorption onto model cellulose and SAM-OH surfaces, respectively. The maximum change in $\Delta\theta_{sp}$ from all sources (reversible adsorption, irreversible adsorption, and the bulk effect) of ~0.003°–0.005° and the contribution arising solely from irreversible adsorption of ~0.002°–0.003° is small. A better way to verify this interpretation is to use Eqns. 3.4 through 3.6 to produce adsorption isotherms (Figure 6.6 for reversible and irreversible adsorption). The y-axis for Figure 6.6 is chosen to be 0 to 0.9 $mg \cdot m^{-2}$ for the sake of subsequent comparisons of HPX adsorption onto cellulose and SAM-OH surfaces with HPX adsorption onto SAM-CH_3 surfaces. Additionally, two dotted horizontal lines have been added as an estimate of Γ for a flat monolayer (Γ_{mono}) of the HPX derivatives with the lowest and highest DS. These estimates assume that the cross-sectional area of the xylose unit is comparable to the cross-sectional area for a cellulose unit, ~60 $Å^2$.[242] The lower dotted line represents Γ_{mono} for DS ~0.37 and the upper dotted line represents Γ_{mono} for DS ~1.69. In order to better see the trends with respect to DS, insets are provided. Figure 6.6 clearly indicates that HPX has the same affinity for the cellulose and SAM-OH surfaces, the affinity is insensitive to DS, and HPX adsorbs at submonolayer coverage. The relatively weak adsorption to these hydrophilic surfaces suggests hydrogen bonding interactions are insufficient to promote

HPX adsorption from aqueous solution. Moreover, the amphiphilicity observed at the air/water interface for HPX derivatives, where air can be regarded as hydrophobic, clearly did not provide predictive insight into HPX adsorption onto hydrophilic surfaces. In the next section, HPX adsorption onto hydrophobic surfaces is considered.

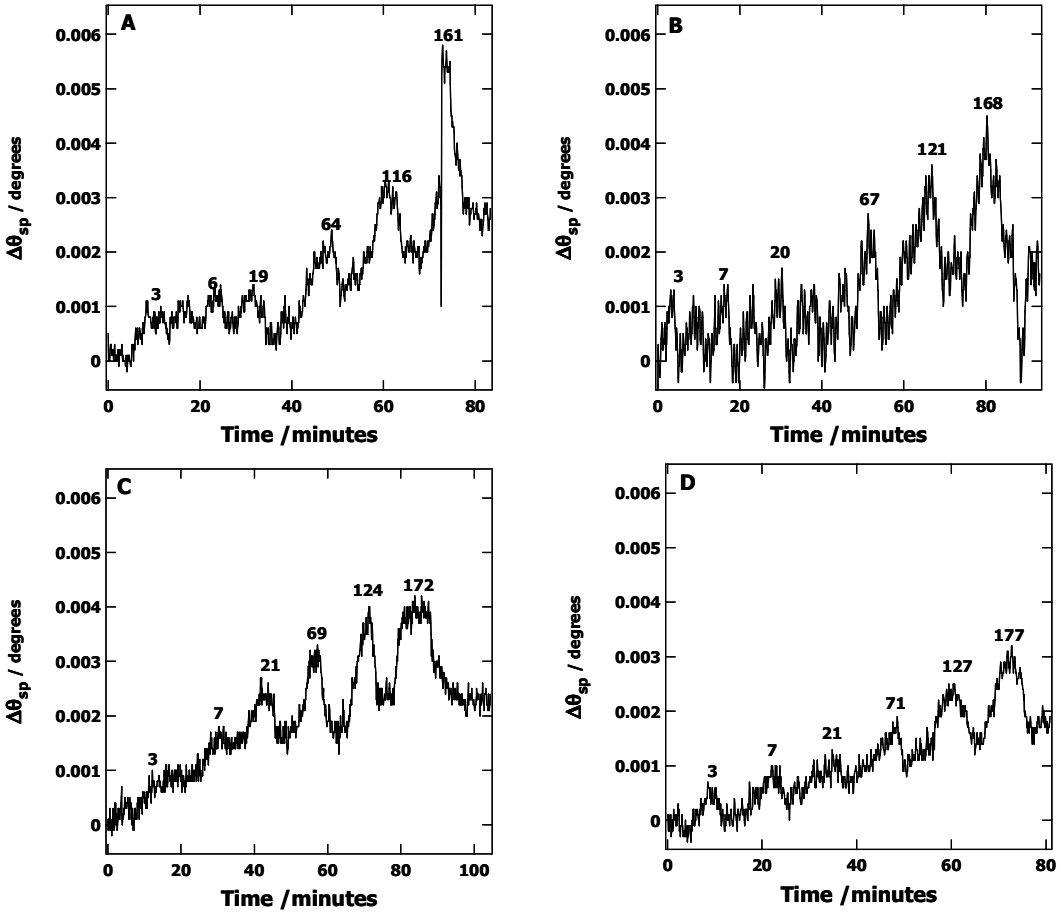

Figure 6.4: Representative SPR data for HPX adsorption onto cellulose regenerated from spin-coated TMSC films at 20.0 °C. Graphs A through D correspond to HPX120, HPX125, HPX127, and HPX130, respectively. Solution concentrations in $mg \cdot L^{-1}$ correspond to the numbers on A through D. Water is flowed through the SPR instrument before and after each new adsorbate solution leading to the observed saw-tooth pattern.

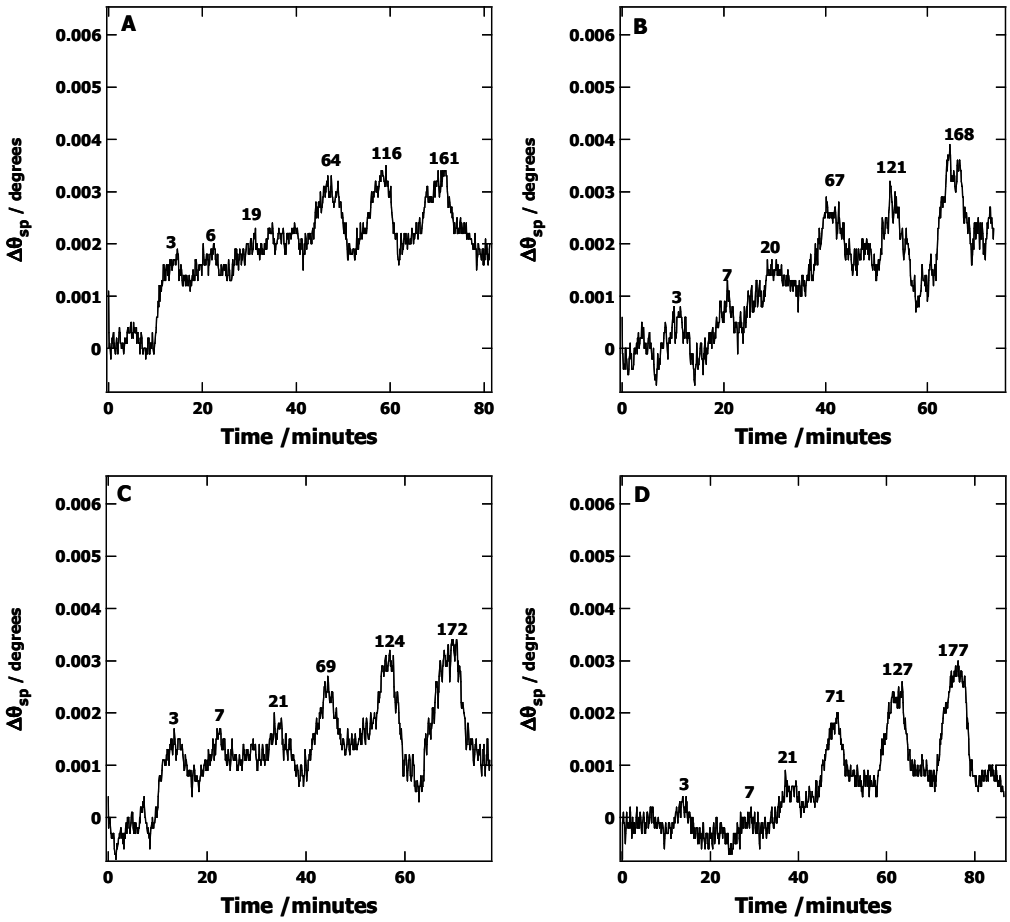

Figure 6.5: Representative SPR data for HPX adsorption onto SAM-OH surfaces at 20.0 °C. Graphs A through D correspond to HPX120, HPX125, HPX127, and HPX130, respectively. Solution concentrations in $mg \cdot L^{-1}$ correspond to the numbers on A through D. Water is flowed through the SPR instrument before and after each new adsorbate solution leading to the observed saw-tooth pattern.

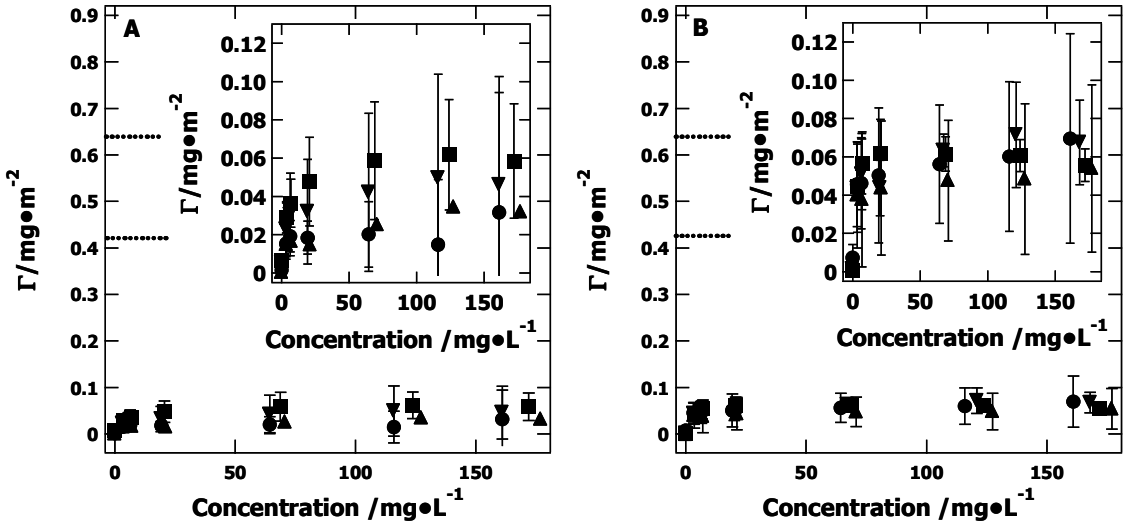

Figure 6.6: HPX adsorption isotherms (reversible and irreversible) for (A) regenerated cellulose, and (B) SAM-OH at 20.0 °C. Symbols correspond to HPX120 (circles), HPX125 (inverted triangles), HPX127 (squares), and HPX130 (triangles) with one standard deviation error bars. Dotted lines on the main graph correspond to estimates of monolayer coverage for the lowest (bottom line) and highest (top line) DS HPX samples.

6.4.4 Adsorption onto SAM-CH_3 surfaces

Figure 6.7 shows representative SPR data for HPX adsorption onto SAM-CH_3 surfaces. Comparing these curves with Figures 6.4 and 6.5, there is at least a 10-fold increase in $\Delta\theta_{sp}$ for both total angle change (reversible adsorption, irreversible adsorption, and the bulk effect) and irreversible HPX adsorption onto cellulose and SAM-OH surfaces. Following the procedure outlined in Eqns. 3.4 through 3.6, the data in Figure 6.7 is converted into adsorption isotherms (Figure 6.8) for total (Figure 6.8A, reversible and irreversible) and irreversible adsorption (Figure 6.8B). More than 90% of the total adsorbed amount comes from irreversible adsorption. Figure 6.8 also contains dotted horizontal lines corresponding to Γ values for a flat HPX monolayer of DS ~0.37 (bottom dotted line) and DS ~1.69 (top dotted line). As one can see, HPX adsorption is consistent with an adsorbed monolayer on the SAM-CH_3 surface. It is also

worth noting that there may be a slight (though statistically insignificant for this study) tendency for HPX adsorption onto SAM-CH_3 surfaces to increase with decreasing DS. If this trend is real, it would be consistent with poorer HPX solubility for low DS HPX promoting deposition onto hydrophobic surfaces.

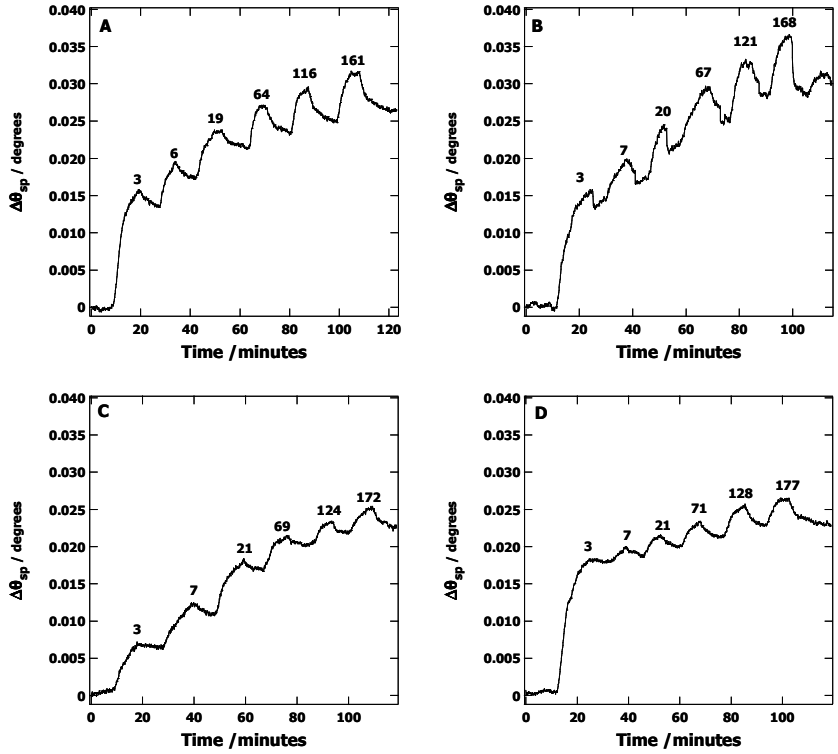

Figure 6.7: Representative SPR data for HPX adsorption onto SAM-CH_3 surfaces at 20.0 °C. Graphs A through D correspond to HPX120, HPX125, HPX127, and HPX130, respectively. Solution concentrations in mg·L^{-1} correspond to the numbers on A through D. Water is flowed through the SPR instrument before and after each new adsorbate solution leading to the observed saw-tooth pattern.

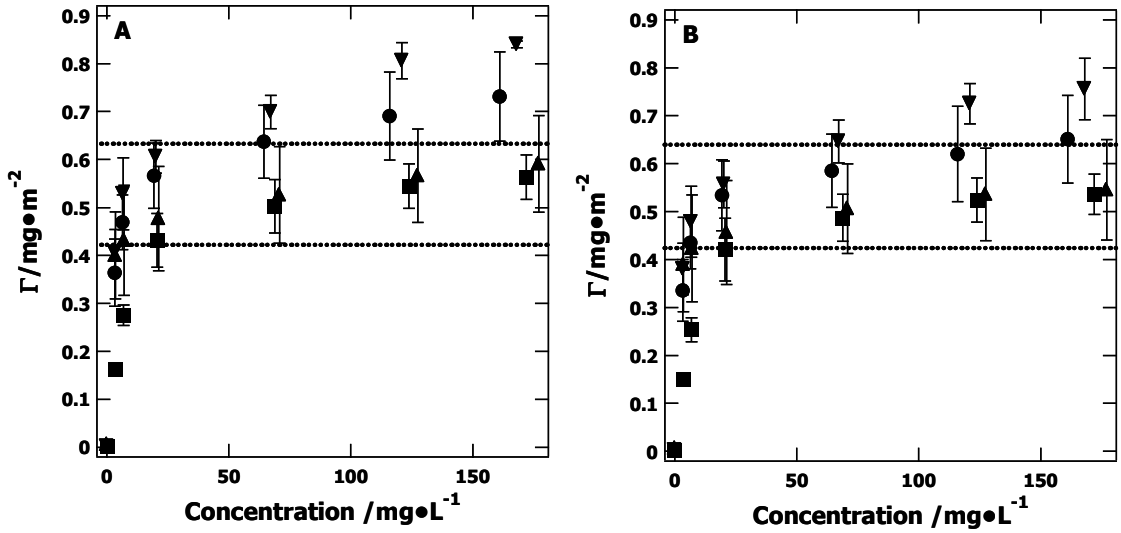

Figure 6.8: HPX adsorption isotherms for SAM-CH_3 surfaces at 20.0 °C. Graph A corresponds to total adsorption (reversible and irreversible) whereas B corresponds to irreversible adsorption. The symbols correspond to HPX120 (circles), HPX125 (inverted triangles), HPX127 (squares), and HPX130 (triangles) with one standard deviation error bars. The dotted horizontal lines correspond to estimates of monolayer coverage for the lowest (bottom line) and highest (top line) DS HPX derivatives.

6.3.5 Conclusions

Water-soluble HPX derivatives are amphiphilic and exhibit increasing affinity for the air/water interface with increasing DS. This behavior is in stark contrast to hydrophilic cellulose and SAM-OH surfaces, where HPX adsorbs at submonolayer coverage. Hence, even though hydroxypropylation yields water-soluble polysaccharides, the derivatives are not necessarily strongly hydrophilic. This interpretation is supported by the observation of HPX adsorption onto hydrophobic SAM-CH_3 surfaces at essentially monolayer coverage. Collectively, these studies show that hydroxypropylation is a good strategy for making soluble hemicellulose derivatives that could be further derivatized to produce surface modifying agents.

CHAPTER 7

Overall Conclusions and Suggestions for Future Work

7.1 Overall Conclusions

This study demonstrated that pullulan cinnamates (PCs) adsorbed onto regenerated cellulose surfaces at levels far greater than pullulan. The resulting layers were uniform, and smooth, and the adsorbed amount increased with increasing degrees of substitution (DS). Similar studies on hydroxyl-terminated self-assembled monolayers (SAM-OH) showed that hydrogen bonding alone could not be the sole driving force for enhanced PC adsorption onto cellulose. Likewise, studies on hydrophobic, methyl-terminated self-assembled monolayers (SAM-CH_3) provided insight into how hydrophobic modification enhanced adsorption onto cellulose. These results suggested that the hydrophobic modification of water-soluble polysaccharides was a good strategy for the promotion of their adsorption onto regenerated cellulose surfaces. Future work should probe the general applicability of this strategy to other polysaccharides, especially xylans (hemicelluloses), and other lignin-like hydrophobic substituents. Successful implementation of this strategy could yield new classes of surface modifying agents for cellulosic and even synthetic materials from sustainable natural materials.

Cationization of glucuronoxylan (GX) from birch produced a series of cationic 2-hydroxypropyltrimethylammonium (HPMA) xylans (HPMAXs) which exhibited an adsorption maximum on carboxyl-terminated SAM (SAM-COOH) surfaces at intermediate DS. The adsorbed layer in the vicinity of the adsorption maximum was consistent with a three dimensional (3D) layer, whereas higher linear charge densities for the polyelectrolyte led to two dimensional (2D) layers. These results were qualitatively consistent with scaling theories. As

such, these materials should be compatible with layer-by-layer assembly to create complex lignocellulosic nanocomposites with controlled layer thicknesses. Moreover, HPMAX adsorption onto SAM-COOH surfaces was strongly correlated with tensile index studies of HPMAX as a paper additive. For HPMAX adsorption onto SAM-CH_3 surfaces, HPMAX aqueous solubility played a critical role as HPMAX adsorption decreased with increasing HPMA DS.

Water-soluble hydroxypropyl xylan (HPX) derivatives were amphiphilic and exhibited increasing affinity for the air/water interface with increasing DS. This behavior was in stark contrast to hydrophilic cellulose and SAM-OH surfaces, where HPX adsorbed at submonolayer coverage. Hence, even though hydroxypropylation yielded water-soluble polysaccharides, the derivatives were not necessarily strongly hydrophilic. This interpretation was supported by the observation of HPX adsorption onto hydrophobic SAM-CH_3 surfaces at essentially monolayer coverage. Collectively, these studies showed that hydroxypropylation was a good strategy for the synthesis of soluble hemicellulose derivatives that could be further derivatized for the production of surface modifying agents.

7.2 Suggested Future Work

The studies of polysaccharide adsorption onto cellulose and SAMs provided in this thesis yielded a fundamental understanding of aspects of interfacial properties of polysaccharides. However, a complete understanding of polysaccharide adsorption onto cellulose fibers and thermoplastic surfaces remains a challenge. In this section, some suggestions for future work based on existing knowledge, and experience and knowledge acquired during the course of this work will be provided.

7.2.1 Pullulan and Pullulan Cinnamate Self-Assembly

Several variables that influence polymer adsorption at solid/liquid interfaces could be studied. Polymer molecular weight is an important variable that affects polysaccharide adsorption onto surfaces. The molecular weight of pullulan can be controlled from 10^3 g·mol^{-1} or lower to 10^6 g·mol^{-1} and possibly higher by selecting the optimal fungal strain and varying the fermentation conditions.[275] Lazoridou et al.[276] showed that it was also possible to obtain pullulan with different molecular weights by fractionation of commercial pullulan by a solvent-gradient technique. As pullulan molecular weight can be adjusted, the effect of molecular weight on polysaccharide self-assembly could be easily studied with a linear, non-branched and non-ionic water soluble polysaccharide.

Model cellulose surfaces studied in this thesis were amorphous surfaces of cellulose[142, 277] which are structurally different from cellulosic fibers (comprised of crystalline cellulose I and amorphous regions).[9] In order to correlate our results to cellulosic fibers, highly crystalline cellulose I surfaces as well as semicrystalline cellulose I surfaces with amorphous regions must be studied. Edgar and Gray[277] introduced a method to prepare cellulose model surfaces from cellulose nanocrystal suspensions. These surfaces yielded smooth films of crystalline cellulose I, however these films lack the amorphous regions that are originally found in cellulosic fibers. These surfaces may also contain sulfate groups due to the hydrolysis reaction during the nanocrystal preparation. Recently, Ahola et al.[207] prepared native cellulose model films containing both amorphous and crystalline cellulose I regions by spin-coating aqueous cellulose nanofibril dispersions onto silica substrates. Nanofibrils from wood pulp with low and high charge density were used to prepare model films. Because the weakly charged nanofibrils did not fully cover the silica substrates, an anchoring substance was selected to improve the coverage.

The best coverage of the fibrils was achieved using 3-aminopropyltrimethoxysilane (APTS) as a cationic anchoring substance. Highly charged fibrils formed fully covered and smooth films on bare silica and hence no anchoring substances were needed.[207] In the future, the method of Ahola et al. could be used to prepare model cellulose films on gold surfaces. For anchoring substances, SAMs with cationic functional end groups such as 11-amino-1-undecanethiol, hydrochloride, (SAM-$NH_3^+Cl^-$) could be used in order to promote the adhesion of cellulose nanofibrils to gold surfaces. These surfaces would be more representative of cellulose surfaces found in nature.

Quartz crystal microbalance with dissipation monitoring (QCM-D) was a recently improved technique for the study of viscoelastic properties of adsorbed film. Quartz crystal microbalances have been commonly configured with electrodes on both sides of a thin disk of AT-cut quartz. Due to the piezoelectric properties and crystalline orientation of the quartz, the application of a voltage between these electrodes caused a shear deformation of the crystal. The crystal could be electrically excited into resonance when the excitation frequency was such that the crystal thickness was an odd multiple of half the acoustic wavelength.[278] The electrodes have been of a number of metals (Au and Pt, etc) deposited upon the upper and lower quartz surfaces. Any mass bound to the surface tended to oscillate with the same lateral displacement and frequency as the underlying crystal. If the coupling between the film and crystal was elastic, there was no energy loss for this process. If energy losses accompany the mass oscillation, the process was inelastic. An increase in mass bound to the quartz surface caused a frequency decrease for the oscillating crystal.[279] For the situation of purely elastic mass added on the surface of the crystal, it was possible to obtain the mass from the Sauerbrey equation with ng sensitivity.[280] Sauerbrey first showed that in vacuum the amount of mass added to the electrodes (Δm) was linearly related to the resulting shift in resonant frequency (Δf) of the oscillator, i.e.,

$$\Delta m = -C(\frac{\Delta f}{n}) \tag{7.1}$$

where C was a constant that depended only on the thickness of the quartz slab and on the intrinsic properties of the quartz, and n was the overtone number.

For modern QCM-D measurements the resonant frequency, Δf, and energy dissipation, ΔD have been simultaneously measured. Here, dissipation refered to the frictional and viscoelastic energy losses on the sensing surface. In normal applications, frequency was measured intermittently, while the oscillator or sensor was driven to resonate, and D was measured when the driving field was disconnected. More specifically, energy dissipation was quantified from the dampening of the oscillating signal as its vibration amplitude decayed exponentially. The dissipation factor was proportional to the power dissipation in the oscillatory system and gave valuable information concerning film rigidity. For example, soft (viscoelastic) films did not fully couple to the oscillation of the crystal and dissipation values were defined as

$$D = \frac{E_{dissipated}}{2\pi E_{stored}} \tag{7.2}$$

where $E_{dissipated}$ and E_{stored} were the values of energy dissipation and storage during one oscillation in the oscillating system, respectively. Hence, the measured changes in D were due to contributions from, for example, slip and viscous losses.[281] Even greater dissipation occurred when an adsorbed material deformed during an oscillation. Soft materials adsorbed on a crystal surface gave higher D values, whereas rigid materials produced low D values. A preliminary example for the adsorption of pullulan and a pullulan cinnamate with a DS = 0.08 onto regenerated cellulose surfaces by using QCM-D was provided in Figure 7.1 for the same experimental conditions (20.00 °C and a flow rate of 0.25 mL•min^{-1}) as the SPR experiments in water presented in Chapter 4. As seen in Figure 7.1A, there was no significant scaled frequency

change (Δf/n) when the regenerated cellulose coated QCM-D crystal was exposed to a pullulan solution. Changes in the dissipation occurred when pullulan solutions flowed over the crystal surfaces, however, ΔD returned to zero after a switch back to water. This result meant that adsorption, if any, in the presence of the pullulan solution was reversible and that ΔD likely reflected a change in the viscosity of the solution rather than reversible adsorption. As seen in Figure 7.1B and in contrast to pullulan, (Δf/n) values indicated that cinnamate groups promoted adsorption, and the failure of the (Δf/n) values to return to zero after a switch back to water indicated that irreversible adsorption had occurred. The observation of $\Delta D > \sim 5\times10^{-6}$ also meant that viscoelastic modeling would be required to interpret the pullulan cinnamate adsorption data. Further systematic experiments will be needed to interpret QCM-D data and to obtain the viscoelastic properties of the adsorbed film on regenereated cellulose surfaces.

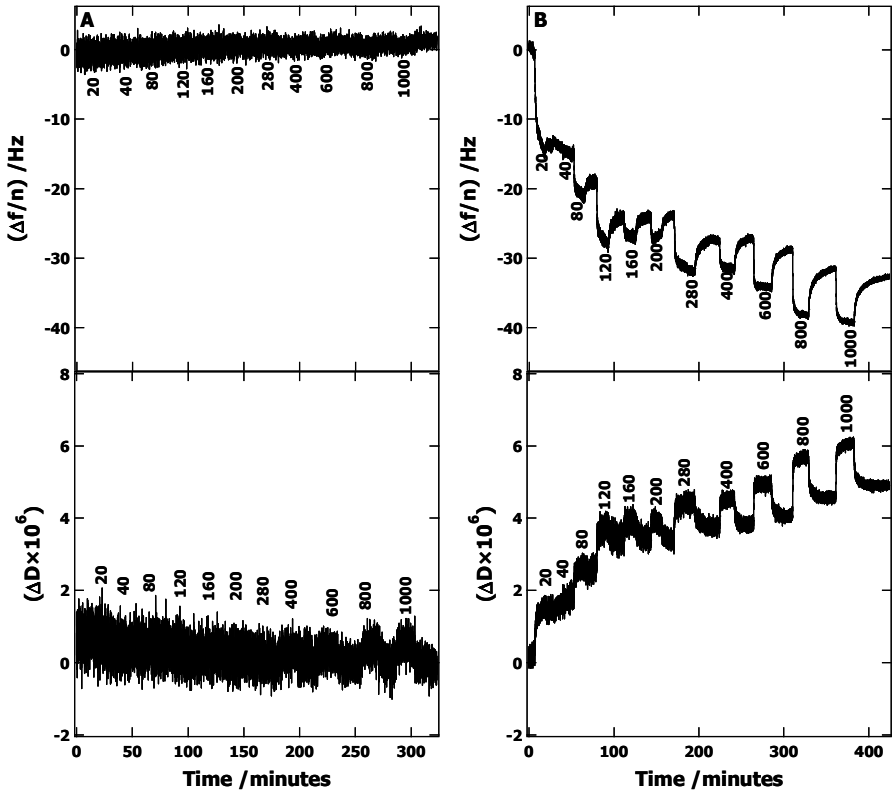

Figure 7.1: (Δf/n) and ΔD from QCM-D for regenerated cellulose surfaces exposed to (A) pullulan and (B) pullulan cinnamate (DS = 0.08). Polymer solution concentrations in $mg \cdot L^{-1}$ corresponded to the numbers on A and B. Curves corresponded to the 5th overtone (n = 5). Water that flowed through the QCM-D instrument before and after each new adsorbate solution yielded the observed saw-tooth pattern.

7.2.2 Layer-by-Layer Assembly of Polysaccharide Films

One powerful method for the fabrication of organic thin films involved the alternate adsorption of polycations and polyanions onto a charged surface which led to the formation of ionically self-assembled multilayer (ISAM) films, through a process more commonly referred to as layer-by-layer (LbL) assembly.[282] For this process, polyelectrolyte adsorption onto an oppositely charged surface produced a charge reversal on the surface; this facilitated the

adsorption of the next layer of an oppositely charged polymer. In fact, films with an arbitrary number of bilayers have been fabricated in this fashion.[283] Multilayer structures composed of polyions or other charged molecular or colloidal objects (or both) have been fabricated into multilayers structures as schematically outlined in Figure 7.2. Because the process only involved adsorption from solution, there were in principle no restrictions with respect to substrate size and topology; multilayers have been prepared on colloids and on objects with dimensions of several tens of centimeters. Film deposition onto substrates from ordinary beakers could be automated or carried out manually as depicted in Figure 7.2A. At the molecular level, this process has yielded films comprised of alternately charged bilayers as depicted in Figure 7.2B. While any polyelectrolyte could be used, sodium poly(styrene sulfonate) and poly(allylamine hydrochloride) (Figure 7.2C) have been the most commonly used.[282]

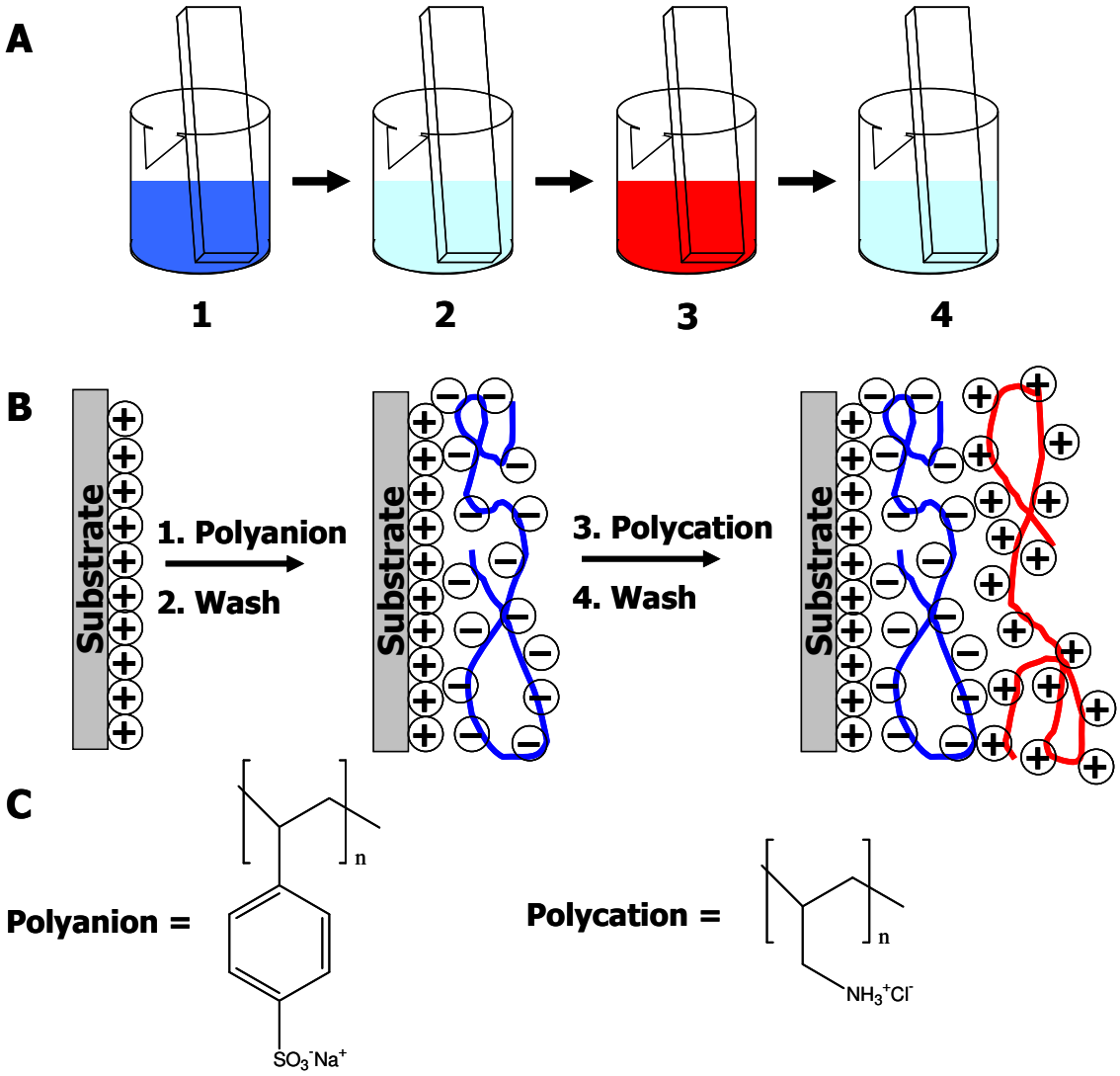

Figure 7.2: (A) Schematic of the film deposition using slides and beakers. Steps 1 and 3 represent the adsorption of a polyanion and polycation, respectively, and steps 2 and 4 are rinsing steps. (B) Simplified molecular pictures of the first two adsorption steps, depicting film deposition starting with a positively charged substrate. Counterions were omitted for clarity. The polyion conformation and layer interpenetration were an idealization of the surface charge reversal with each adsorption step. (C) Chemical structures of two typical polyions, the sodium salt of poly(styrene sulfonate) and poly(allylamine hydrochloride). Adapted from Decher.[282]

In the future, LbL films of HPMAs and cellulose nanocrsytals (CNXLs) could be prepared on both gold and silicon surfaces. CNXLs have been obtained by sulfuric acid hydrolysis of native cellulose leading to stable aqueous suspensions of rodlike nanocrystals whose size and aspect ratio depended upon their biological origin.[284, 285] Gold surfaces and silicon wafers or glass slides have been cationized by SAM-$NH_3^+Cl^-$ and APTS molecules, respectively. Then, successive deposition of CNXLs and HPMAs would then yield the desired number of bilayers. As seen in Chapter 5, ionic strength and charge density of HPMAXs play an important role in HPMAX adsorption onto SAM-COOH surfaces. Likewise, they would play an important role in the ultimate layer structure of LbL films of HPMAs and CNXLs.

7.2.3 Other Xylan Derivatives

Chapter 5 and 6 decribed self-assembly of HPMAX and HPX on cellulose surfaces and SAMs, respectively. The chemical structure of other xylan derivatives which could be studied were provided as Figure 7.3. A comparison of the properties of adsorbed films of carboxymethyl xylan (CMX) (Figure 7.3a) on cellulose with carboxymethyl cellulose (CMC) films would be interesting. CMC adsorbed onto cellulose surfaces at high ionic strengths though it did not show adsorption onto cellulose surfaces in salt-free conditions.[286] Self-assembly studies of methyl xylan (MX) (Figure 7.3b) and hydroxyethyl xylan (HEX) (Figure 7.3c) at the air/water interfaces would be interesting for comparison to HPX discussed in Chapter 6. It would also be interesting to compare xylan sulfate (XS) adsorption onto cellulose with CMX adsorption onto cellulose surfaces to define the role anion structure plays in the process. Finally, it would be interesting to study diisopropylaminoethyl xylan (DIPEX) as it and HPMAX (Chapter 5) have similar structures. Because DIPEX is more sterically hindered, steric effects on self-assembly could be studied.

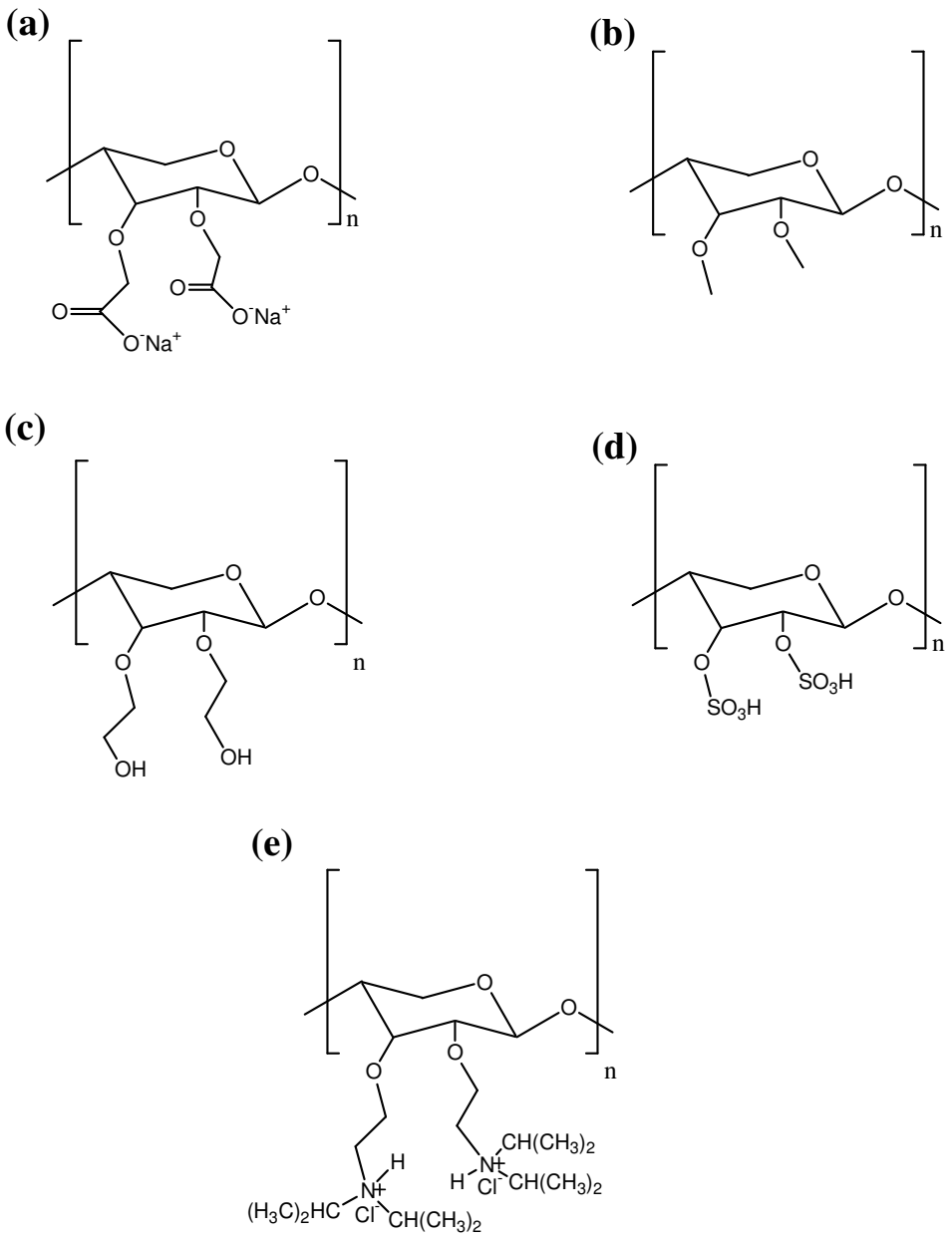

Figure 7.3: Chemical structures of xylan derivatives for possible study. (a) Carboxymethyl xylan (CMX), (b) methyl xylan (MX), (c) hydroxyethyl xylan (HEX), (d) xylan sulfate (XS), and (e) diisopropylaminoethyl xylan (DIPEX).

Bibliography

(1) Parham, R. A.; Gray, R. L. *Advances in Chemistry Series* **1984**, *207*, 3-56.
(2) Thomas, R. J. *ACS Symposium Series* **1977**, *43*, 1-23.
(3) Jane, F. W.; Wilson, K.; White, D. J. B. *The Structure of Wood*; Adam & Charles Black: London, UK, 1970.
(4) Fujita, M.; Harada, H. In *Wood and Cellulosic Chemistry*; 2nd ed.; Hon, D. N.-S. and Shiraishi, N., Eds.; Marcel Dekker, Inc.: New York, NY, 2001, p 1-49
(5) Dadswell, H. E.; Hillis, W. E. In *Wood Extractives*; Hillis, W. E., Ed.; Academic Press Inc: New York, NY, 1962, p 3-55
(6) Reiter, W.-D. *Current Opinion in Plant Biology* **2002**, *5*, 536-542.
(7) Saka, S. In *Wood and Cellulosic Chemistry*; 2nd ed.; Hon, D. N.-S. and Shiraishi, N., Eds.; Marcel Dekker, Inc.: New York, N. Y., 2001, p 51-81
(8) Singh, S. K.; Gross, R. A. *ACS Symposium Series* **2001**, *786*, 2-40.
(9) O'Sullivan, A. C. *Cellulose* **1997**, *4*, 173-207.
(10) Klemm, D.; Heublein, B.; Fink, H.-P.; Bohn, A. *Angewandte Chemie* **2005**, *44*, 3358-3393.
(11) Kontturi, E.; Tammelin, T.; Osterberg, M. *Chemical Society Reviews* **2006**, *5*, 1287-1304.
(12) Currey, J. D. *The Journal of Materials Education* **1983**, *9*, 119-196.
(13) Williamson, R. E.; Burn, J. E.; Hocart, C. H. *Cellular and Molecular Life Sciences* **2001**, *58*, 1475-1490.
(14) Sarko, A. In *Wood and cellulosics: Industrial utilization, biotechnology, structure and properties*; Kennedy, J. F., Phillips, G. O. and Williams, P. A., Eds.; Ellis Horwood Limited: Chichester, 1987, p 55-69
(15) Brown, R. M. J. *Journal of Polymer Science, Part A: Polymer Chemistry* **2004**, *42*, 487-495.
(16) Langan, P.; Nishiyama, Y.; Chanzy, H. *Journal of the American Chemical Society* **1999**, *121*, 9940-9946.
(17) Nishiyama, Y.; Langan, P.; Chanzy, H. *Journal of the American Chemical Society* **2002**, *124*, 9074-9082.
(18) Nishiyama, Y.; Sugiyama, J.; Chanzy, H.; Langan, P. *Journal of the American Chemical Society* **2003**, *125*, 14300-14306.
(19) Michell, A. J.; Higgins, H. G. *Cellulose* **1999**, *6*, 89-91.
(20) Lora, J. H.; Glasser, W. G. *Journal of Polymers and the Environment* **2002**, *10*, 39-48.
(21) Higuchi, T. *Journal of Wood Science* **2006**, *52*, 2-8.
(22) Suhas, P. J. M. C.; Carrott, M. M. L. R. *Bioresource Technology* **2007**, *98*, 2301-2312.
(23) Alen, R. In *Forest Products Chemistry*; Stenius, P., Ed.; Fabet Oy: Jyvaskyla, Finland, 2000, p 11-57
(24) Chakar, F. S.; Ragauskas, A. J. *Industrial Crops and Products* **2004**, *20*, 131-141.
(25) Davin, L. B.; Lewis, N. G. *Current Opinion in Biotechnology* **2005**, *16*, 407-415.
(26) Glasser, W. G. *ACS Symposium Series* **2000**, *742*, 216-238.
(27) Sakakibara, A.; Sano, Y. In *Wood and Cellulosic Chemistry*; 2nd ed.; Hon, D. N.-S. and Shiraishi, N., Eds.; Marcel Dekker, Inc.: New York, NY, 2001, p 109-173
(28) Goring, D. A. I. *ACS Symposium Series* **1989**, *397*, 2-10.
(29) Lin, S. Y.; Dence, C. W. In *Methods in Lignin Chemistry*; Lin, S. Y. and Dence, C. W., Eds.; Springer-Verlag: Berlin 1992
(30) Sun, R.; Sun, X. F.; Tomkinson, J. *ACS Symposium Series* **2004**, *864*, 2-22.

(31) Ishii, T.; Shimizu, K. In *Wood and Cellulosic Chemistry*; Hon, D. N.-S. and Shiraishi, N., Eds.; Marcel Dekker, Inc.: New York, NY, 2001, p 175-212
(32) Zhang, Y. H. P. *Journal of Industrial Microbiology & Biotechnology* **2008**, *35*, 367-375.
(33) Ebringerova, A.; Hromadkova, Z.; Heinze, T. *Advances in Polymer Science* **2005**, *186*, 1-67.
(34) Stephen, A. M. In *The Polysaccharides*; Aspinall, G. O., Ed.; Academic Press: New York, 1983; Vol. 2, p 97-194
(35) Cronquist, A. *Basic Botany* Harper & Row Publishers: New York, 1982.
(36) Ebringerova, A. *Macromolecular Symposia* **2006**, *232*, 1-12.
(37) Ebringerová, A.; Heinze, T. *Macromolecular Rapid Communications* **2000**, *21*, 542-556.
(38) Salmen, L.; Burgert, I. *Holzforschung* **2009**, *63*, 121-129.
(39) Lawoko, M.; Henriksson, G.; Gellerstedt, G. *Biomacromolecules* **2005**, *6*, 3467-3473.
(40) Kaplan, D. S. *Journal of Applied Polymer Science* **1976**, *20*, 2615-2629.
(41) Kelley, S. S.; Rials, T. G.; Glasser, W. G. *Journal of Materials Science* **1987**, *22*, 617-624.
(42) Glasser, W. G.; Rials, T. G.; Kelley, S. S.; Dave, V. *ACS Symposium Series* **1998**, *688*, 265-282.
(43) Yaku, F.; Tsuji, S.; Koshijima, T. *Holzforschung* **1979**, *33*, 54-59.
(44) Koshijima, T.; Watanabe, T.; Yaku, F. *ACS Symposium Series* **1989**, *397*, 11-28.
(45) Johnson, K. G.; Overend, R. P. *Holzforschung* **1991**, *45*, 469-475.
(46) Uraki, Y.; Hashida, K.; Sano, Y. *Holzforschung* **1997**, *51*, 91-97.
(47) Barlow, R. J.; Zimmerman, S.; Khougaz, K.; Eisenberg, A. *Journal of Polymer Science, Part B: Polymer Physics* **1996**, *34*, 1197-1212.
(48) Hirai, M.; Takizawa, T.; Yabuki, S.; Nakata, Y.; Hirai, T.; Hayashi, K. *Journal of Physical Chemistry* **1996**, *100*, 11675-11680.
(49) Winnik, F. M.; Regismond, S. T. A.; Goddard, E. D. *Langmuir* **1997**, *13*, 111-114.
(50) Sau, A. C.; Landoll, L. M. *Advances in Chemistry Series* **1989**, *223*, 343-364.
(51) Esker, A.; Becker, U.; Jamin, S.; Beppu, S.; Renneckar, S.; Glasser, W. *ACS Symposium Series* **2004**, *864*, 198-219.
(52) Mora, F.; Ruel, K.; Comtat, J.; Joseleau, J.-P. *Holzforschung* **1986**, *40*, 85-91.
(53) Henriksson, Å.; Gatenholm, P. *Holzforschung* **2001**, *55*, 494-502.
(54) Linder, Å.; Bergman, R.; Bodin, A.; Gatenholm, P. *Langmuir* **2003**, *19*, 5072-5077.
(55) Fleer, G. J.; Stuart, M. A. C.; Scheutjens, J. M. H. M.; Cosgrove, T.; Vincent, B. *Polymers at Interfaces*; Chapman & Hall: London, 1993.
(56) Dabrowski, A. *Advances in Colloid and Interface Science* **2001**, *93*, 135-224.
(57) Myers, D. *Surfaces, Interfaces, and Colloids: Principles and Applications*; VCH Publishers, Inc.: New York, 1991.
(58) Hiemenz, P. C.; Rajagopalan, R. *Principles of Colloid and Surface Chemistry*; Marcel Dekker, Inc.: New York, 1997.
(59) Adamson, A. W. *Physical Chemistry of Surfaces*; 5 ed.; John Wiley & Sons, Inc.: New York, 1990.
(60) Evans, D. F.; Wennerström, H. *The Colloidal Domain: Where Physics, Chemistry, Biology, and Technology Meet* 2nd ed.; Wiley-VCH: New York, 1999.
(61) Langmuir, I. *Journal of the American Chemical Society* **1918**, *40*, 1361-1402.
(62) Romero-Cano, M. S.; Martin-Rodriguez, A.; de las Nieves, F. J. *Journal of Colloid and Interface Science* **2000**, *227*, 322-328.

(63) Blackburn, R. S.; Harvey, A.; Kettle, L. L.; Payne, J. D.; Russell, S. J. *Langmuir* **2006**, *22*, 5636-5644.
(64) Kaggwa, G. B.; Stefanie Froebe; Huynh, L.; Ralston, J.; Bremmell, K. *Langmuir* **2005**, *21*, 4695-4704.
(65) Norde, W. *Surfactant Science Series* **2003**, *110*, 21-43.
(66) Silberberg, A. *Journal of Chemical Physics* **1968**, *48*, 2835-2851.
(67) Roe, R.-J. *Journal of Chemical Physics* **1974**, *60*, 4192-4207.
(68) Netz, R. R.; Andelman, D. *Physics Reports* **2003**, *380*, 1-95.
(69) de Gennes, P. G. *Advances in Colloid and Interface Science* **1987**, *27*, 189-209.
(70) Scheutjens, J. M. H. M.; Fleer, G. J. *Journal of Physical Chemistry* **1980**, *84*, 178-190.
(71) Simha, R.; Frisch, H. L.; Eirich, F. R. *Journal of Physical Chemistry* **1953**, *57*, 584-589.
(72) Silberberg, A. *Journal of Physical Chemistry* **1962**, *66*, 1884-1907.
(73) Silberberg, A. *Journal of Physical Chemistry* **1962**, *66* 1872-1883.
(74) DiMarzio, E. A. *Journal of Chemical Physics* **1965**, *42*, 2101-2106.
(75) Roe, R. J. *Journal of Chemical Physics* **1965**, *3*, 1591-1598.
(76) Scheutjens, J. M. H. M.; Fleer, G. J. *Journal of Physical Chemistry* **1979**, *83*, 1619-1635.
(77) de Gennes, P. G. *Scaling Concepts in Polymer Physics*; Cornell Univ. Press: Ithaca, N. Y., 1979.
(78) de Gennes, P. G. *Macromolecules* **1980**, *13*, 1069-1075.
(79) Eisenriegler, E.; Kremer, K.; Binder, K. *Journal of Chemical Physics* **1982**, *77*.
(80) Milchev, A.; Binder, K. *Macromolecules* **1996**, *29*, 343-354.
(81) Skau, K. I.; Blokhuis, E. M.; Male, J. v. *Macromolecules* **2004**, *37*, 1969-1979.
(82) Ploehn, H. J.; Russel, W. B.; Hall, C. K. *Macromolecules* **1988**, *21*, 1075-1085.
(83) Kawaguchi, M.; Takahashi, A. *Advances in Colloid and Interface Science* **1992**, *37*, 219-317.
(84) Ploehn, H. J.; Russel, W. B. *Macromolecules* **1989**, *22*, 266-276.
(85) Edwards, S. F. *Proceedings of the Physical Society* **1965**, *85*, 613-624.
(86) Hlady, V.; Lyklema, J.; Fleer, G. J. *Journal of Colloid and Interface Science* **1982**, *87*, 395-406.
(87) de Gennes, P. G. *Macromolecules* **1981**, *14*, 1637-1644.
(88) Eisenriegler, E. *Journal of Chemical Physics* **1983**, *79*, 1052-1064.
(89) O'Shaughnessy, B.; Vavylonis, D. *Journal of Physics: Condensed Matter* **2005**, *17*, R63-R99.
(90) Auvray, L.; Cotton, J. P. *Macromolecules* **1987**, *20*, 202-207.
(91) Lee, L. T.; Guiselin, O.; Farnoux, B.; Lapp, A. *Macromolecules* **1991**, *24*, 2518-2522.
(92) Guiselin, O.; Lee, L. T.; Farnoux, B.; Lapp, A. *Journal of Chemical Physics* **1991**, *95*, 4632-4640.
(93) Barrat, J.-L.; Joanny, J.-F. *Advances in Chemical Physics* **1996**, *94*, 1-66.
(94) Mandel, M. In *Polyelectrolytes: Science and Technology*; Hara, M., Ed.; Marcel Dekker, Inc.: New York, N. Y., 1993
(95) Volk, N.; Vollmer, D.; Schmidt, M.; Oppermann, W.; Huber, K. *Advances in Polymer Science* **2004**, *166*, 29-65.
(96) Foerster, S.; Schmidt, M.; Antonietti, M. *Journal of Physical Chemistry* **1992**, *96*, 4008-4014.
(97) Borochov, N.; Henryk Eisenberg, H. *Macromolecules* **1994**, *27*, 1440-1445.

(98) Ise, N.; Okubo, T.; Yamamoto, K.; Kawai, H.; Hashimoto, T.; Fujimura, M.; Hiragi, Y. *1980* **1980**, *102*, 7901-7906.
(99) Dobrynin, A. V.; Rubinstein, M. *Progress in Polymer Science* **2005**, *30*, 1049-1118.
(100) Flory, P. J.; Osterheld, J. E. *Journal of Physical Chemistry* **1954**, *58*, 653-661.
(101) Eisenberg, H.; Woodside, D. *Journal of Chemical Physics* **1962**, *36*, 1844-1854.
(102) Schweins, R.; Hollmann, J.; Huber, K. *Polymer* **2003**, *44*, 7131-7141.
(103) Eisenberg, H.; Mohan, G. R. *Journal of Physical Chemistry* **1959**, *63*, 671-680.
(104) Eisenberg, H.; Casassa, E. F. *Journal of Polymer Science* **1960**, *47*, 29-44.
(105) Ikegami, A.; Iami, N. *Journal of Polymer Science* **1962**, *56*, 133-152.
(106) Shubin, V. *Journal of Colloid and Interface Science* **1997**, *191*, 372-377.
(107) Hesselink, F. T. *Journal of Colloid and Interface Science* **1977**, *60*, 448-466.
(108) Hoeve, C. A. J. *Journal of Polymer Science, Polymer Symposia* **1971**, *34*, 1-10.
(109) Hoeve, C. A. J. *Journal of Polymer Science, Polymer Symposia* **1970**, *30* 30 361-367.
(110) van der Schee, H. A.; Lyklema, J. *Journal of Physical Chemistry* **1984**, *88*, 6661-6667.
(111) Papenhuijzen, J.; Schee, H. A. V. d.; Fleer, G. J. *Journal of Colloid and Interface Science* **1985**, *104*, 540-552.
(112) Evers, O. A.; Fleer, G. J.; Scheutjens, J. M. H. M.; Lyklema, J. *Journal of Colloid and Interface Science* **1986**, *111*, 446-454.
(113) Bohmer, M. R.; Evers, O. A.; Scheutjens, J. M. H. M. *Macromolecules* **1990**, *23*, 2288-2301.
(114) Vermeer, A. W. P.; Leermakers, F. A. M.; Koopal, L. K. *Langmuir* **1997**, *13*, 4413-4421.
(115) Blaakmeer, J.; Bohmer, M. R.; Stuart, M. A. C.; Fleer, G. J. *Macromolecules* **1990**, *23*, 2301-2309.
(116) van de Steeg, H. G. M.; Cohen Stuart, M. A.; Keizer, A. D.; Bijsterbosch, B. H. *Langmuir* **1992**, *8*, 2538-2546.
(117) Hendrickson, E. R.; Neuman, R. D. *Journal of Colloid and Interface Science* **1986**, *110*, 243-251.
(118) Pelton, R. H. *Journal of Colloid and Interface Science* **1986**, *111*, 475-485.
(119) Wang, T. K.; Audebert, R. *Journal of Colloid and Interface Science* **1988**, *121*, 32-41.
(120) Shubin, V.; Linse, P. *Journal of Physical Chemistry* **1995**, *99*, 1285-1291.
(121) Davies, R. J.; Dix, L. R.; Toprakcioglu, C. *Journal of Colloid and Interface Science* **1989**, *129*, 145-152.
(122) Durand, G.; Lafuma, F.; Audebert, R. *Progress in Colloid & Polymer Science* **1988**, *76*, 278-282.
(123) Shklovskii, B. I. *Physical Review Letters* **1999**, *82*, 3268-3271.
(124) Shklovskii, B. I. *Physical Review E: Statistical Physics* **1999**, *60*, 5802-5811.
(125) Dobrynin, A. V.; Deshkovski, A.; Rubinstein, M. *Physical Review Letters* **2000**, *84*, 3101-3104.
(126) Dobrynin, A. V.; Deshkovski, A.; Rubinstein, M. *Macromolecules* **2001**, *34*, 3421-3436.
(127) Dobrynin, A. V.; Rubinstein, M. *Journal of Physical Chemistry B* **2003**, *107*, 8260-8269.
(128) Dobrynin., A. V. *Journal of Chemical Physics* **2001**, *114*, 8145-8153.
(129) Joanny, J.-F.; Castelnovo, M.; Netz, R. *Journal of Physics: Condensed Matter* **2000**, *12*, A1-A7.
(130) Petty, M. C. *Langmuir-Blodgett Films*; Cambridge University Press: Cambridge, UK, 1996.
(131) Blodgett, K. B. *Journal of the American Chemical Society* **1935**, *57*, 1007-1022.

(132) Blodgett, K. B.; Langmuir, I. *Physical Review* **1937**, *51*, 964-982.
(133) Kaganer, V. M.; Mohwald, H.; PulakDutta *Reviews of Modern Physics* **1999**, *71*, 779-819.
(134) Butt, H.-J.; Graf, K.; Kappl, M. *Physics and Chemistry of Interfaces*; Wiley-VCH GmbH & Co. KGaA: Darmstadt, Germany, 2003.
(135) Dynarowicz-Latka, P.; A Dhanabalan; Oliveira, O. N. *Advances in Colloid and Interface Science* **2001**, *91*, 221-293.
(136) Schaub, M.; Wenz, G.; Wegner, G.; Stein, A.; Klemm, D. *Advanced Materials* **1993**, *5*, 919-922.
(137) Holmberg, M.; Berg, J.; Stemme, S.; Odberg, L.; Rasmusson, J.; Claesson, P. *Journal of Colloid and Interface Science* **1997**, *186*, 369-381.
(138) Buchholz, V.; Adler, P.; Baecker, M.; Hoelle, W.; Simon, A.; Wegner, G. *Langmuir* **1997**, *13*, 3206-3209.
(139) Rehfeldt, F.; Tanaka, M. *Langmuir* **2003**, *19*, 1467-1473.
(140) Buchholz, V.; Wegner, G.; Stemme, S.; Oedberg, L. *Advanced Materials* **1996**, *8*, 399-402.
(141) Geffroy, C.; Labeau, M. P.; Wong, K.; Cabane, B.; Stuart, M. A. C. *Colloids and Surfaces, A: Physicochemical and Engineering Aspects* **2000**, *172*, 47-56.
(142) Kontturi, E.; Thune, P. C.; Niemantsverdriert, J. W. H. *Langmuir* **2003**, *19*, 5735-5741.
(143) Kontturi, E.; Thune, P. C.; Niemantsverdriet, J. W. *Polymer* **2003**, *44*, 3621-3625.
(144) Ulman, A. *Chemical Reviews* **1996**, *96*, 1533-1554.
(145) Schreiber, F. *Progress in Surface Science* **2000**, *65*, 151-256.
(146) Schlotter, N. E.; Porter, M. D.; Bright, T. B.; Allara, D. L. *Chemical Physics Letters* **1986**, *132*, 93-98.
(147) Ogawa, H.; Chihara, T.; Taya, K. *Journal of the American Chemical Society* **1985**, *107*, 1365-1369.
(148) Allara, D. L.; Nuzzo, R. G. *Langmuir* **1985**, *1*, 45-52.
(149) Allara, D. L.; Nuzzo, R. G. *Langmuir* **1985**, *1*, 52-66.
(150) Sagiv, J. *Journal of the American Chemical Society* **1980**, *102*, 92-98.
(151) Maoz, R.; Sagiv, J. *Journal of Colloid and Interface Science* **1984**, *100*, 465-496.
(152) Gun, J.; Sagiv, J. *Journal of Colloid and Interface Science* **1986**, *112*, 457-472.
(153) Wasserman, S. R.; Tao, Y. T.; Whitesides, G. M. *Langmuir* **1989**, *5*, 1074-1087.
(154) Silberzan, P.; Leger, L.; Ausserre, D.; Benattar, J. J. *Langmuir* **1991**, *7*, 1647-1651.
(155) Grange, J. D. L.; Markham, J. L.; Kurkjian, C. R. *Langmuir* **1993**, *9*, 1749-1753.
(156) Nuzzo, R. G.; Allara, D. L. *Journal of the American Chemical Society* **1983**, *105*, 4481-4483.
(157) Porter, M. D.; Bright, T. B.; Allara, D. L.; Chidsey, C. E. D. *Journal of the American Chemical Society* **1987**, *109*, 3559-3568.
(158) Bain, C. D.; Troughton, E. B.; Tao, Y.-T.; Evall, J.; Whitesides, G. M.; Nuzzo, R. G. *Journal of the American Chemical Society* **1989**, *111*, 321-335.
(159) Nuzzo, R. G.; Dubois, L. H.; Allara, D. L. *Journal of the American Chemical Society* **1990**, *112*, 558-569.
(160) Dubois, L. H.; Zegarski, B. R.; Nuzzo, R. G. *Journal of the American Chemical Society* **1990**, *112*, 570-579.
(161) Thomas, R. C.; Sun, L.; Crooks, R. M.; Ricco, A. J. *Langmuir* **1991**, *7*, 620-622.

(162) Chailapakul, O.; Sun, L.; Xu, C.; Crooks, R. M. *Journal of the American Chemical Society* **1993**, *115*, 12459-12467.
(163) Bain, C. D.; Biebuyck, H. A.; Whitesides, G. M. *Langmuir* **1989**, *5*, 723-727.
(164) Nuzzo, R. G.; Fusco, F. A.; Allara, D. L. *Journal of the American Chemical Society* **1987**, *109*, 2358-2368.
(165) Nuzzo, R. G.; Zegarski, B. R.; Dubois, L. H. *Journal of the American Chemical Society* **1987**, *109*, 733-740.
(166) Li, Y.; Huang, J.; Jr, R. T. M.; Hemminger, J. C. *Journal of the American Chemical Society* **1992**, *114*, 2428-2432.
(167) Widrig, C. A.; Chung, C.; Porter, M. D. *Journal of Electroanalytical Chemistry and Interfacial Electrochemistry* **1991**, *310*, 335-359.
(168) Bryant, M. A.; Pemberton, J. E. *Journal of the American Chemical Society* **1991**, *113*, 8284-8293
(169) Dubois, L. H.; Nuzzo, R. G. *Annual Review of Physical Chemistry* **1992**, *43*, 437-463.
(170) Love, J. C.; Estroff, L. A.; Kriebel, J. K.; Nuzzo, R. G.; Whitesides, G. M. *Chemical reviews* **2005**, *105*, 1103-1169.
(171) Laibinis, P. E.; Whitesides, G. M.; Allara, D. L.; Tao, Y. T.; Parikh, A. N.; Nuzzo, R. G. *Journal of the American Chemical Society* **1991**, *113*, 7152-7167.
(172) Ulman, A.; Eilers, J. E.; Tillman, N. *Langmuir* **1989**, *5*, 1147-1152.
(173) Strong, L.; Whitesides, G. M. *Langmuir* **1988**, *4*, 546-558.
(174) Chidsey, C. E. D.; Loiacono, D. N. *Langmuir* **1990**, *6*, 682-691.
(175) Widrig, C. A.; Alves, C. A.; Porter, M. D. *Journal of the American Chemical Society* **1991**, *113*, 2805-2810.
(176) Brockman, J. M.; Nelson, B. P.; Corn, R. M. *Annual Review of Physical Chemistry* **2000**, *51*, 41-63.
(177) Karlsson, R.; Michaelsson, A.; Mattsson, L. *Journal of Immunological Methods* **1991**, *145*, 229-240.
(178) Green, R. J.; Frazier, R. A.; Shakesheff, K. M.; Davies, M. C.; Roberts, C. J.; Tendler, S. J. *Biomaterials* **2000**, *21*, 1823-1835.
(179) Jordan, C. E.; Frutos, A. G.; Thiel, A. J.; Corn, R. M. *Analytical Chemistry* **1997**, *69*, 4939-4947.
(180) Thiel, A. J.; Frutos, A. G.; Jordan, C. E.; Corn, R. M.; Smith, L. M. *Analytical Chemistry* **1997**, *69*, 4948-4956.
(181) Frutos, A. G.; Corn, R. M. *Analytical Chemistry* **1998**, *70*, 449A-455A.
(182) Fischer, B.; Heyn, S. P.; Egger, M.; Gaub, H. E. *Langmuir* **1993**, *9*, 136-140.
(183) Berger, C. E. H.; Beumer, T. A. M.; Kooyman, R. P. H.; Greve, J. *Analytical Chemistry* **1998**, *70*, 703-706.
(184) Frutos, A. G.; Weibel, S. C.; Corn, R. M. *Analytical Chemistry* **1999**, *71*, 3935-3940.
(185) Brockman, J. M.; Frutos, A. G.; Corn, R. M. *Journal of the American Chemical Society* **1999**, *121*, 8044-8051.
(186) Earp, R. L.; Dessy, R. E. In *Commercial Biosensors: Applications to Clinical, Bioprocess, and Environmental Samples*; Ramsay, G., Ed.; John Wiley & Sons, Inc.: New York, 1998; Vol. 148, p 99-164
(187) Kretschmann, E. *Zeitschrift fuer Physik* **1971**, *241*, 313-324.
(188) Liedberg, B.; Johansen, K. *Methods in Biotechnology* **1998**, *7*, 31-53.
(189) Earp, R. L. Ph. D. Dissertation, Virginia Tech, Blacksburg, VA, 1999.

(190) Sambles, J. R.; Bradbery, G. W.; Yang, F. *Contemporary Physics* **1991**, *32*, 173-183.
(191) Salamon, Z.; Macleod, H. A.; Tollin, G. *Biochimica et Biophysica Acta* **1997**, *1331*, 117-129.
(192) van Krevelen, D. V. *Properties of Polymers: Their Correlation with Chemical Structure; Their Numerical Estimation and Prediction from Additive Group Contributions*; Elsevier: Amsterdam, 1997.
(193) de Feijter, J. A.; Benjamins, J.; Veer, F. A. *Biopolymers* **1978**, *17*, 1759-1772.
(194) Sigal, G. B.; Mrksich, M.; Whitesides, G. M. *Langmuir* **1997**, *13*, 2749-2755.
(195) Tulpar, A.; Ducker, W. A. *Journal of Physical Chemistry B* **2004**, *108*, 1667-1676.
(196) Norman, L. L.; Badia, A. *Langmuir* **2007**, *23*, 10198-10208.
(197) Sigal, G. B.; Mrksich, M.; Whitesides, G. M. *Journal of the American Chemical Society* **1998**, *120*, 3464-3473.
(198) Donabedian, D. H.; McCarthy, S. P. *Macromolecules* **1998**, *31*, 1032-1039.
(199) McIntyre, D. D.; Vogel, H. J. *Starch/Staerke* **1993**, *45*, 406-410.
(200) Pattanaargson, S.; Munhapol, T.; Hirunsupachot, P.; Luangthongaram, P. *Journal of Photochemistry and Photobiology, A: Chemistry* **2004**, *161*, 269-274.
(201) Horton, H. R.; Moran, L. A.; Scrimgeour, K. G.; Perry, M. D.; Rawn, J. D. *Principles of Biochemistry*; 4th ed.; Pearson Prentice Hall: Upper Saddle River, NJ, 2006.
(202) Patnaik, P. *Dean's Analytical Chemistry Handbook* 2nd ed.; McGraw-Hill: New York, 2004.
(203) Schwikal, K.; Heinze, T.; Ebringerova, A.; Petzold, K. *Macromolecular Symposia* **2006**, *232*, 49-56.
(204) Jain, R. K.; Sjöstedt, M.; Glasser, W. G. *Cellulose* **2001**, *7*, 319-336.
(205) Carson, J. F.; Maclay, W. D. *Journal of the American Chemical Society* **1946**, *68*, 1015-1017.
(206) Ni, S.; Yin, W.; Ferguson-McPherson, M. K.; Satija, S. K.; Morris, J. R.; Esker, A. R. *Langmuir* **2006**, *22*, 5969-5973.
(207) Ahola, S.; Salmi, J.; Johansson, L.-S.; Laine, J.; Oesterberg, m. *Biomacromolecules* **2008**, *9*, 1273-1282.
(208) Nichifor, M.; Lopes, S.; Bastos, M.; Lopes, A. *Journal of Physical Chemistry B* **2004**, *108*, 16463-16472.
(209) Hunkeler, D.; Wu, X. Y.; Hamielec, A. E. *ACS Symposium Series* **1992**, *480*, 53-79.
(210) Wagner, P.; Hegner, M.; Guentherodt, H.-J.; Semenza, G. *Langmuir* **1995**, *11*, 867-3875.
(211) Toyama, S.; Aoki, K.; Kato, S. *Sensors and Actuators B* **2005**, *108*, 903-909.
(212) Harvey, A. H.; Gallagher, J. S.; Sengers, J. M. H. L. *Journal of Physical and Chemical Reference Data* **1998**, *27*, 761-774.
(213) Malitson, I. H. *Journal of the Optical Society of America* **1962**, *52*, 1377-1379.
(214) Palik, E. D. *Handbook of Optical Constants of Solids*; Academic Press: Orlando, 1985.
(215) Peterlinz, K. A.; Georgiadis, R. *Langmuir* **1996**, *12*, 4731-4740.
(216) *CRC Handbook of Chemistry and Physics, 88th Edition*; CRC Press/Taylor and Francis: Boca Raton, FL, 2008.
(217) Bond, G. M.; Richman, R. H.; McNaughton, W. P. *Journal of Materials Engineering and Performance* **1995**, *4*, 334-345.
(218) Fratzl, P. *Journal of the Royal Society, Interface* **2007**, *4*, 637-642.
(219) Toriz, G.; Arvidsson, R.; Westin, M.; Gatenholm, P. *Journal of Applied Polymer Science* **2003**, *88*, 337-345.

(220) Teeri, T. T.; Brumer, H.; Daniel, G.; Gatenholm, P. *Trends in Biotechnology* **2007**, *25*, 299-306.
(221) Fratzl, P.; Weinkamer, R. *Progress in Materials Science* **2007**, *52*, 1263-1334.
(222) Mohanty, A. K.; Misra, M.; Drzal, L. T. *Composite Interfaces* **2001**, *8*, 313-343.
(223) Samir, M. A. S. A.; Alloin, F.; Dufresne, A. *Biomacromolecules* **2005**, *6*, 612-626.
(224) Gustavsson, M. T.; Persson, P. V.; Iversen, T.; Martinelle, M.; Hult, K.; Teeri, T. T.; Brumer III, H. *Biomacromolecules* **2005**, *6*, 196-203.
(225) Akiyoshi, K.; Yamaguchi, S.; Sunamoto, J. *Chemistry Letters* **1991**, *7*, 1263-1266.
(226) Akiyoshi, K.; Nagai, K.; Nishikawa, T.; Sunamoto, J. *Chemistry Letters* **1992**, *9*, 1727-1730.
(227) Akiyoshi, K.; Sunamoto, J. *Surfactant Science Series* **1992**, *44*, 289-304.
(228) Sunamoto, J.; Sato, T.; Taguchi, T.; Hamazaki, H. *Macromolecules* **1992**, *25*, 5665-5670.
(229) Akiyoshi, K.; Deguchi, S.; Moriguchi, N.; Yamaguchi, S.; Sunamoto, J. *Macromolecules* **1993**, *26*, 3062-3068.
(230) Akiyoshi, K.; Sunamoto, J. *Supramolecular Science* **1996**, *3*, 157-163.
(231) Duval-Terrie, C.; Huguet, J.; Muller, G. *Colloids and Surfaces, A: Physicochemical and Engineering Aspects* **2003**, *220*, 105-115.
(232) Sallustio, S.; Galantini, L.; Gente, G.; Masci, G.; Mesa, C. L. *Journal of Physical Chemistry B* **2004**, *108*, 18876-18883.
(233) Henni, W.; Deyme, M.; Stchakovsky, M.; LeCerf, D.; Picton, L.; Rosilio, V. *Journal of Colloid and Interface Science* **2005**, *281*, 316-324.
(234) Baszkin, A.; Rosilio, V.; Albrecht, G.; Sunamoto, J. *Journal of Colloid and Interface Science* **1991**, *145*, 502-511.
(235) Deme, B.; Rosilio, V.; Baszkin, A. *Colloids and Surfaces, B: Biointerfaces* **1995**, *4*, 357-365.
(236) Paris, E.; Stuart, M. A. C. *Macromolecules* **1999**, *32*, 462-470.
(237) Simon, S.; Picton, L.; Cerf, D. L.; Muller, G. *Polymer* **2005**, *46*, 3700-3707.
(238) Deme, B.; Lee, L.-T. *Journal of Physical Chemistry B* **1997**, *101*, 8250-8258.
(239) Gradwell, S. E.; Renneckar, S.; Esker, A. R.; Heinze, T.; Glasser, W. G. *Comptes Rendus Biologies* **2004**, *327*, 945-953.
(240) Torn, L. H.; Koopal, L. K.; Keizer, A. d.; Lyklema, J. *Langmuir* **2005**, *21*, 7768-7775.
(241) Penfold, J.; Tucker, I.; Petkov, J.; Thomas, R. K. *Langmuir* **2007**, *23*, 8357-8364.
(242) Kawaguchi, T.; Nakahara, H.; Fukuda, K. *Thin Solid Films* **1985**, *133*, 29-38.
(243) Kontturi, K. S.; Tammelin, T.; Johansson, L.-S.; Stenius, P. *Langmuir* **2008**, *24*, 4743-4749.
(244) Mohanty, A. K.; Misra, M.; Drzal, L. T. *Journal of Polymers and the Environment* **2002**, *10*, 19-26.
(245) Mohanty, A. K.; Misra, M.; Hinrichsen, G. *Macromolecular Materials and Engineering* **2000**, *276/277*, 1-24.
(246) Rojas, O. J.; Ernstsson, M.; Neuman, R. D.; Claesson, P. M. *Journal of Physical Chemistry B* **2000**, *104*, 10032-10042.
(247) Tammelin, T.; Saarinen, T.; Oesterberg, M.; Laine, J. *Cellulose* **2006**, *13*, 519-535.
(248) Ahola, S.; Osterberg, M.; Laine, J. *Cellulose* **2008**, *15*, 303-314.
(249) Jacobs, A.; Larsson, P. T.; Dahlman, O. *Biomacromolecules* **2001**, *2*, 979-990.
(250) Teleman, A.; Larsson, P. T.; Iversen, T. *Cellulose* **2001**, *8*, 209-215.

(251) Windham, W. R.; Amos, H. E.; Evans, J. J. *Journal of Agricultural and Food Chemistry* **1987**, *35*, 698-704.
(252) Österberg, M. *Journal of Colloid and Interface Science* **2000**, *229*, 620-627.
(253) Schwikal, K. Ph. D. Dissertation, Friedrich-Schiller-University, Jena, Germany, 2007.
(254) Dunlop-Jones, N. In *Paper Chemistry*; Roberts, J. C., Ed.; Chapman and Hall: New York, NY, 1991, p 76-96
(255) Bowen, J.; Manickam, M.; Evans, S. D.; Critchley, K.; Kendall, K.; Preece, J. A. *Thin Solid Films* **2008**, *516*, 2987-2999.
(256) Smith, D. A.; Wallwork, M. L.; Zhang, J.; Kirkham, J.; Robinson, C.; Marsh, A.; Wong, M. *Journal of Physical Chemistry B* **2000**, *104*, 8862-8870.
(257) Rinaudo, M. *ACS Symposium Series* **1992**, *489*, 24-37.
(258) Lerouxel, O.; Cavalier, D. M.; Liepman, A. H.; Keegstra, K. *Current Opinion in Plant Biology* **2006**, *9*, 621-630.
(259) Glasser, W. G.; Ravindran, G.; Jain, R. K.; Samaranayake, G.; Todd, J. *Biotechnology Progress* **1995**, *11*, 552-557.
(260) Ebringerová, A.; Hromádková, Z. *Biotechnology and Genetic Engineering Reviews* **1999**, *16*, 325-346.
(261) Gröndahl, M.; Teleman, A.; Gatenholm, P. *Carbohydrate Polymers* **2003**, *52*, 359-366.
(262) Gröndahl, M.; Eriksson, L.; Gatenholm, P. *Biomacromolecules* **2004**, *5*, 1528-1535.
(263) Gabrielii, I.; Gatenholm, P.; Glasser, W. G.; Jain, R. K.; Kenne, L. *Carbohydrate Polymers* **2000**, *43*, 367-374.
(264) Ebringerová, A.; Hromadkova, Z.; Burchard, W.; Dolega, R.; Vorwerg, W. *Carbohydrate Polymers* **1994**, *24*, 161-169.
(265) Timell, T. E.; Glaudemans, C. P. J.; Gillham, J. K. *Tappi* **1959**, *42*, 623-634.
(266) Carson, J. F.; Maclay, W. D. *Journal of the American Chemical Society* **1948**, *70*, 293-295.
(267) Vincendon, M. *Die Makromolekulare Chemie* **1993**, *194*, 321-328.
(268) Antal, M.; Ebringerová, A.; Hromádková, Z.; Pikulik, I. I.; Laleg, M.; Micko, M. M. *Das Papier* **1997**, *51*, 223-226.
(269) Ebringerová, A.; Hromádková, Z.; Kacuráková, M.; Antal, M. *Carbohydrate Polymers* **1994**, *24*, 301-307.
(270) Paananen, A.; Österberg, M.; Rutland, M.; Tammelin, T.; Saarinen, T.; Tappura, K.; Stenius, P. *ACS Symposium Series* **2004**, *864*, 269-290.
(271) McNally, E.; Zografi, G. *Journal of Colloid and Interface Science* **1990**, *138*, 61-68.
(272) Alexandridis, P.; Hatton, T. A. *Colloids and Surfaces, A: Physicochemical and Engineering Aspects* **1995**, *96*, 1-46.
(273) Paterson, I. F.; Chowdhry, B. Z.; Leharne, S. A. *Langmuir* **1999**, *15*, 6187-6194.
(274) Dong, J.; Chowdhry, B. Z.; Leharne, S. A. *Colloids and Surfaces A: Physicochemical and Engineering Aspects* **2006**, *277*, 249-254.
(275) Yuen, S. *Process Biochemistry* **1974**, *9*, 7-22.
(276) Lazaridou, A.; Biliaderis, C. G.; Kontogiorgos, V. *Carbohydrate Polymers* **2003**, *52*, 151-166.
(277) Edgar, C. D.; Gray, D. G. *Cellulose* **2003**, *10*, 299-306.
(278) Martin, S. J.; Victoria Edwards Granstaff; Frye, G. C. *Analytical Chemistry* **1991**, *63*, 2272-2281.
(279) Marx, K. A. *Biomacromolecules* **2003**, *4*, 1099-1120.

(280) Sauerbrey, G. *Zeitschrift fuer Physik* **1959**, *155*, 206-222.
(281) Turon, X.; Rojas, O. J.; Deinhammer, R. S. *Langmuir* **2008**, *24*, 3880-3887.
(282) Decher, G. *Science* **1997**, *277*, 1232-1237.
(283) Garg, A.; Heflin, J. R.; Gibson, H. W.; Davis, R. M. *Langmuir* **2008**, *24*, 10887-10894.
(284) Revol, J. F.; Bradford, H.; Giasson, J.; Marchessault, R. H.; Gray, D. G. *International Journal of Biological Macromolecules* **1992**, *14*, 170-172.
(285) Dong, X. M.; Kimura, T.; Revol, J.-F.; Gray, D. G. *Langmuir* **1996**, *12*, 2076-2082.
(286) Liu, Z.; Choi, H.; Gatenholm, P.; Esker, A. R. In *Proceedings of the Annual Meeting of the Adhesion Society*; Anderson, G., Ed.; The Adhesion Society: Savannah, GA, 2009, p 152-154.